Master's thesis

NTNU
Norwegian University of Science and Technology
Faculty of Natural Sciences
Department of Materials Science and Engineering

Pål Emil England Karstensen

Simulation of Anion-Exchange Membrane Water Electrolyser with degradation of IrO_2 as electrocatalyst for oxygen evolution

Master's thesis in MTKJ
Supervisor: Svein Sunde
Co-supervisor: Michael Gerhardt
June 2023

NTNU
Norwegian University of Science and Technology

Pål Emil England Karstensen

Simulation of Anion-Exchange Membrane Water Electrolyser with degradation of IrO_2 as electrocatalyst for oxygen evolution

Master's thesis in MTKJ
Supervisor: Svein Sunde
Co-supervisor: Michael Gerhardt
June 2023

Norwegian University of Science and Technology
Faculty of Natural Sciences
Department of Materials Science and Engineering

NTNU
Norwegian University of
Science and Technology

Preface

The work presented in this thesis is a part of the course *TMT4900 - Materials Chemistry and Energy Technology, Master's Thesis* at NTNU spring 2023. It is the finishing course for the specialisation of Material science and Energy Technology within the five-year master programme Chemical Engineering and Biotechnology.

First of all, I would like to give my sincere gratitude to my supervisor Svein Sunde for lending me his expertise. He has provided excellent guidance, ideas, and discussions which have been crucial for the progression of the microkinetic modelling.

I would like to extend my utmost gratitude to my Co-supervisor Michael Gerhardt. Michael has been an essential piece in my overall progression regarding programming, electrochemistry, and personal growth. He has indeed given me invaluable assistance and provided me with his availability in my time of need. Especially when I did not understand things in the continuum model, which was about 90% of the time, Michael aided me time and time again. In short, this project would not be possible without Michael.

Lastly, I am very grateful for the support and motivation I have received from the "Mattek gang" during our trying times writing our theses. It has truly been a journey and I am glad I had such good friends with me to brighten the days at our reading hall.

Abstract

The growing effects of global warming attributed to the increase of CO_2 and other greenhouse gases in the atmosphere originating from human industry, enhances the motivation to find suitable replacements. Hydrogen has long been an attractive energy replacement for fossil fuels, and catalytic splitting of water through water electrolysis provides a way of producing hydrogen without CO_2 emissions. However, commercial water electrolysers either in lack efficiency or use platinum group metal materials as catalysts, which are quite scarce. Anion-exchange membrane water electrolysers (AEM-WEs), aim to combine the advantages of both the established low-temperature water electrolysers by combining alkaline operation with anionic-specific membranes. Still, the AEM-WE is relatively new, but has the potential to produce energy- and cost-efficient hydrogen by the use of more abundant catalyst materials. One of the problems with AEM-WE is catalyst stability. Microkinetic modelling has been applied to describe the degradation of IrO_2 under oxygen evolution conditions in both acidic and alkaline environments based on experimental degradation measurements [1, 2]. The alkaline model was then implemented into a continuum model developed by SINTEF [3] simulating the operation of an AEM-WE, trying to qualitatively capture the effects of anode catalyst degradation during polarisation. The simulations showed that catalyst degradation led to an offset in polarisation curves indicating a worsening in performance, though a smaller offset than expected. Furthermore, degradation did not occur uniformly across the catalyst layer; the rate of degradation was indeed faster closest to the anion-exchange membrane. However, the alkaline microkinetic model implemented in the continuum model by SINTEF [3] predicted too rapid degradation under normal AEM-WE operating conditions, suggesting a discrepancy between the continuum model and the microkinetic model. Nevertheless, the qualitative effects of degradation of IrO_2 as an oxygen evolution catalyst in an AEM-WE, could be described by microkinetic modelling.

Sammendrag

Økende effekter av global oppvarming som skyldes voksende mengder CO_2 og andre drivhusgasser forbundet med menneskelig industri øker motivasjonen for å finne erstatninger for fossile brensler. Hydrogen har lenge vært en attraktiv erstatning for fossile brensler, og katalytisk deling av vann gjennom vannelektrolyse er en teknologi som lar deg dele vann til hydrogen og oksygen uten produksjon av CO_2. Likevel sliter de kommersielle vannelektrolysørene enten med dårlig effektivitet eller bruk av dyre, edle, og skjeldne metaller. Vannelektrolysører med anionutveklsingsmembran har som mål å kombinere fordelene med de allerede kommersielle vannelektrolysørene ved å kombinere basisk drift med anionspesifikke membraner. Selv om vannelektrolysører med anionutveklsingsmembraner er relativt nye, så har de potensiale til å produsere billigere hydrogen ved å bruke metaller som ikke er like sjeldne. En av problemene med denne teknologien er stabiliteten til katalysatorene under utvikling av oksygen ved anoden. Mikrokinetisk modellering har blitt brukt til å beskrive nedbryting av IrO_2 under oksygen utvikling i sure og basiske forhold basert på eksperimentelle målinger [1, 2]. Den basiske modellen ble så implementert i en continuumsmodell utviklet av SINTEF[3] som simulerer en vannelektrolysør med anionisk utvekslingsmembran, og på den måten kvalitativt beskrive påvirkningen av nedbryting av katalysatorlaget hos anoden under polarisering. Simuleringene viste at nedbrytning av katalysatorlaget førte til dårligere drift sammenlignet med uten nedbryting, likevel var denne effekten mye mindre enn antatt. Simuleringene avslørte også at nedbrytingen ikke foregikk homogent over hele katalysatoren; nedbrytingshastigheten var størst nærmest anionutveklsingsmembranen. Likevel, implementeringen av den basiske mikrokinetiske modellen av nedbryting inn i continuumsmodellen forutså en for rask nedbryting av katalysatorlaget under normale driftsbetingelser, noe som kan tyde på avvik mellom continuumsmodellen og den mikrokinetiske modellen. De kvalitative effektene av nedbrytingen av IrO_2 som katalysator for oksygen utvikling i en vannelektrolysør med anionutveklsingsmembran kunne likevel bli beskrevet ved bruk av mikrokinetisk modellering.

Contents

List of Figures

List of Tables

Nomenclature

List of abbreviations, symbols, subscripts, and superscripts used in the thesis

Abbreviations

GHG	Green House gase
AEM	Anion-Exchange Membrane
PEM	Proton-Exchange Membrane
A-WE	Alkaline Water Electrolyser
AEM-WE	Anion-Exchange Membrane Water Electrolyser
PEM-WE	Proton-Exchange Membrane Water Electrolyser
HER	Hydrogen Evolution Reaction
OER	Oxygen Evolution Reaction
CV	Cyclic voltammetry
LSV	Linear sweep voltammetry
SHE	Standard Hydrogen Electrode
RHE	Regular Hydrogen Electrode
PGM	Platinum Group Metals
PTL	Porous Transport Layer
CL	Catalyst Layer
BP	Bipolar plates
MEA	Membrane Electrode Assembly
LOER	Lattice Oxygen Evolution Reaction
LOM	Lattice Oxide Oxidation Mechanism/ Lattice Oxygen Participated Mechanism

Inmr	Ionomer	
rds	Rate determining step	
calc	Calculated	
meas	Measured	
DFT	Density Functional Theory	

Symbols

E	Potential.	V
E°	Standard reduction potential.	V vs SHE
$E^{\circ}_{\mathrm{a}}/E^{\circ}_{\mathrm{c}}$	Standard reduction potential for anode/cathode reaction.	V vs SHE
E°_{j}	Standard reduction potential for reaction/step j.	V vs SHE
E_{j}	Reduction potential for reaction/step j.	V vs SHE
E_{n}	Null potential.	V vs SHE
E_{i}	Initial potential.	V
$E^{\circ}_{\mathrm{Cell}}$	Standard cell potential.	V vs SHE
η^{surf}_{j}	Surface overpotential related to reaction j.	V
ν	Sweep rate.	$\mathrm{V\,s^{-1}}$
$\tilde{\mu}_{\mathrm{k}}$	Electrochemical potential of species k.	$\mathrm{J\,mol^{-1}}$
μ_{k}	Chemical potential of species k.	$\mathrm{J\,mol^{-1}}$
μ°_{k}	Standard chemical potential of species k.	$\mathrm{J\,mol^{-1}}$
a_{k}	Activity of species k.	-
γ_{k}	Activity coefficient of species k.	-
z_{k}	Charge number of species k.	-

Φ_β	Potential in phase β.	V
$\vec{N}_{\mathrm{k},\beta}$	Total molar flux density of species k in phase β.	$\mathrm{mol\,m^{-2}\,s^{-1}}$
$\vec{N}_{\mathrm{k}}^{Trans}$	Molar flux density of species k by *Trans* mode of transport.	$\mathrm{mol\,m^{-2}\,s^{-1}}$
$\vec{J}_{\mathrm{k},\beta}$	Mass flux density of species k in phase β.	$\mathrm{g\,m^{-2}\,s^{-1}}$
c_{t}	Total concentration.	$\mathrm{mol\,m^{-3}}$
$c_{\mathrm{k},\beta}$	Concentration of species k in phase β.	$\mathrm{mol\,m^{-3}}$
$c_{\mathrm{k}}/c_{\mathrm{l}}$	Concentration of species k/l.	$\mathrm{mol\,m^{-3}}$
$\vec{v}_{\mathrm{k}}/\vec{v}_{\mathrm{l}}$	Velocity of species k/l.	$\mathrm{m\,s^{-1}}$
$\vec{v}_\beta$	Velocity of phase β.	$\mathrm{m\,s^{-1}}$
D_{k}	Diffusion coefficient for species k.	$\mathrm{m^2\,s^{-1}}$
D_{k}^{Eff}	Effective diffusion coefficient for species k.	$\mathrm{m^2\,s^{-1}}$
$\mathfrak{D}_{\mathrm{kl}}$	Diffusion coefficient between species k and l.	$\mathrm{m^2\,s^{-1}}$
u_{k}	Mobility of species k.	$\mathrm{m^2\,V^{-1}\,s^{-1}}$
$\rho_{\mathrm{k},\beta}$	Mass density of species k in phase β.	$\mathrm{g\,m^{-3}}$
B_β	Permeability of the solid phase to phase β.	$\mathrm{m^2}$
B_{Sat}	Saturated permability.	$\mathrm{m^2}$
ϵ_β	Volume fraction related to phase β.	-
η_β	Viscosity of phase β.	Pa s
p_β	Pressure of phase β.	Pa
τ	Tourtosity.	-
R_{k}	Production term for species k.	$\mathrm{mol\,m^{-3}\,s^{-1}}$
t_{k}	Transport number of species k.	-

i	Current density.	$\mathrm{A\,m^{-2}}$
i_β	Total current density in phase β.	$\mathrm{A\,m^{-2}}$
i_j	Current density related to reaction j.	$\mathrm{A\,m^{-2}}$
i_t^{an}	Total anodic current density.	$\mathrm{A\,m^{-2}}$
$i_{\mathrm{j},\beta}^{rx}$	Reaction rate related to reaction j in phase β.	$\mathrm{A\,m^{-3}}$
$i_{\mathrm{n,\,j}}$	Exchange current density for reaction j.	$\mathrm{A\,m^{-2}}$
I	Current.	A
A	Surface area.	$\mathrm{m^2}$
α_j	Charge transfer coefficient for reaction j.	-
$\alpha_{j,a}/\alpha_{j,c}$	Anodic/cathodic charge transfer coefficient for reaction j.	-
n	Number of electrons transferred for a reaction.	-
$\bar{V}_{\mathrm{IrO_2}}$	Molar volume of iridium oxide.	$\mathrm{m^3\,mol^{-1}}$
V_P	Volume per particle.	$\mathrm{m^3}$
N_P	Number of particles per volume.	$\mathrm{m^{-3}}$
r	Radius of particle.	m
a	Specific interfacial area.	$\mathrm{m^2\,m^{-3}}$
a_β	Specific interfacial area of phase β.	$\mathrm{m^2\,m^{-3}}$
M_k	Molar mass of species k.	$\mathrm{g\,mol^{-1}}$
X_β	Fraction covered by phase β.	-
$S_{\mathrm{k},\beta}$	Source term for species k in phase β.	$\mathrm{g\,m^{-3}\,s^{-1}}$ or $\mathrm{mol\,m^{-3}\,s^{-1}}$ or $\mathrm{s^{-1}}$
ν_k	Stoichiometric coefficient for species k.	-
Ω_k	Reaction order for species k.	-

t	Time.	s
t_i	Initial time.	s
t_Max	Time at maximum potential.	s
r_j	Total reaction rate of reaction j.	$\mathrm{mol\,m^{-2}\,s^{-1}}$
$r_\mathrm{j+}$	Forward reaction rate of reaction j.	$\mathrm{mol\,m^{-2}\,s^{-1}}$
$r_\mathrm{j-}$	Backward reaction rate of reaction j.	$\mathrm{mol\,m^{-2}\,s^{-1}}$
$\hat{r}_\mathrm{j}$	Rate determining step j.	$\mathrm{mol\,m^{-2}\,s^{-1}}$
$k_\mathrm{j,+}$	Potential dependent rate constant for forward reaction j.	$\mathrm{s^{-1}}$
$k_\mathrm{j,}$	Potential dependent rate constant for backward reaction j.	$\mathrm{s^{-1}}$
K_j	Potential dependent equilibrium constant for reaction j.	-
$k^0_\mathrm{j+}$	Chemical rate constant for forward reaction j.	$\mathrm{s^{-1}}$
$k^0_\mathrm{j-}$	Chemical rate constant for backward reaction j.	$\mathrm{s^{-1}}$
K^0_j	Chemical equilbrium constant for reaction j.	-
θ_k	Fractional coverage of species k.	-
Γ	Concentration of active sites on surface.	$\mathrm{mol\,m^{-2}}$
$\Gamma\theta_\mathrm{k}$	Surface coverage of species k.	$\mathrm{mol\,m^{-2}}$
$\frac{d\mathrm{Ir}}{dt}$	Dissolution rate of iridium.	$\mathrm{mol\,m^{-2}\,s^{-1}}$
χ^2	Squared difference of calculated and measured values.	-
R^2	Coefficient of determination.	-
$\Delta_r G^\circ_\mathrm{j}$	Standard Gibbs free energy from reaction j.	$\mathrm{J\,mol^{-1}}$
$\Delta_r G_\mathrm{j}$	Gibbs free energy from reaction j.	$\mathrm{J\,mol^{-1}}$
T	Temperature.	K

Physical constants

R	Molar gas constant.	$8.314\,\mathrm{J\,K^{-1}\,mol^{-1}}$
F	Faradays constant.	$96\,485\,\mathrm{C\,mol^{-1}}$
K_W	Equilibrium constant for autoprotolysis of water.	10^{-14}
c^0	Reference concentration.	$1\,\mathrm{mol\,L^{-1}}$

Subscripts

a	Anode.
c	Cathode.
Cell	Cell.
k	Denotes species k.
l	Denotes additional species l.
j	Denotes reaction/step j.
i	Initial.
β	Denotes phase β.
G	Gas phase.
L	Liquid/Electrolyte phase.
Inmr	Ionomer phase.
IrO_2	Iridium oxide phase.
t	Total.
Sat	Saturated.
Diss	Dissolution.
OER	Oxygen evolution reaction.
Eff	Denotes effective quantity.
Max	Maximum.

$+$	Forward.
-	Backward.
P	Particle quantity.

Superscripts

$^{\ominus}$	Standard state.
$^{\rightarrow}$	Vector quantity.
$^{\wedge}$	Rate determining step.
$Diff$	Transport mod: Diffusion.
Mig	Transport mode: Migration
$Conv$	Transport mode: Convection.
$surf$	Surface.
rx	Reaction rate.
an	Anodic.
0	Purely chemical quantity.

1 Introduction

In recent years, the world has experienced the adverse effects of climate change, of which the greenhouse gas (GHG) CO_2 has played a key role [4]. Climate change has led to more rapid occurrences of extreme weather, more drought, more acidic environment in the seas, etc. These effects have been linked to higher concentrations of CO_2 in the atmosphere originating from human industry from the use of fossil fuels [4, 5]. Different measures have been taken worldwide in order to reduce the emissions from GHGs and especially CO_2, such as the Paris Agreement [6], the Kyoto Protocol [7], and the recent meeting in Glasgow in 2021 [8]. Such agreements have led to more innovation and investments in renewable and alternative energy sources. One of the promising alternative energy carriers to fossil fuels is hydrogen[9].

Hydrogen is attractive in many ways: it has a high energy density compared to fossil fuels[9] when used as an energy source through a combustion reaction; it does not produce any CO_2, but water (see reaction 1.3 and 1.6); and it can be produced from water, which is one of the more abundant compounds on earth, through water electrolysis. The most common ways of producing hydrogen are either through chemical synthesis from natural gas, usually referred to as gray hydrogen [10], or through water electrolysis, which is commonly referred to as green hydrogen [10]. Green hydrogen can be produced through the electrocatalytic splitting of water into hydrogen, H_2, and oxygen, O_2[9, 11, 12]. Electrocatalytic splitting of water is, however, not a spontaneous process, and therefore it requires some form of energy. This energy should indeed come from renewable energy sources, and not from fossil fuels in order to make the hydrogen production without CO_2 emissions.

Water electrolysis is an already established technology and recently, it has gained a lot of interest. Efforts have been made to improve the technology even further, especially in the field of a quite young electrolysis technology, namely the anion-exchange membrane water electrolyser (AEM-WE). The AEM-WE is similar to the alkaline water electrolyser (A-WE) in the manner of an alkaline environment, it is also comparable to the proton-exchange membrane water electrolyser (PEM-WE) when it comes to membrane technology; both of them use solid polymer membrane [13, 14, 15]. The AEM-WE is the least established technology of the three, but it shows great potential when it comes to producing cost- and energy-

efficient hydrogen by combining the advantages from both the PEM-WE and the A-WE[9, 16, 17, 18]. The limiting factor for water electrolysis technology, in general, is the sluggish kinetics of the oxygen evolution reaction (OER) occurring on the anode and the stability of the catalyst material [19, 20, 21, 22, 23, 24, 25]. It is therefore essential to understand the OER in order to improve AEM-WE performance.

The OER is infamously known for lowering the cost- and energy efficiency of hydrogen production. The large overpotential related to the evolution of oxygen at the anode is perhaps one of the dominating factors causing a loss in energy efficiency [26, 27, 28, 20]. This has then motivated the search for viable electrocatalysts that can lower this energy loss and improve efficiency[15, 19, 29, 30]. Usually, noble metals, such as iridium, ruthenium, platinum, and their oxides have been used as such catalysts due to their outstanding catalytic activity towards both the hydrogen evolution reaction (HER) and OER [2]. Ir and iridium oxide are often regarded as the benchmark for OER catalytic activity due to their high stability and high activity, especially in acidic environments. However, the low abundance and high cost of noble metals make them less attractive for industrial applications. The activity towards OER is one problem, but the electrocatalysts must also be stable enough to sustain the harsh conditions surrounding oxygen evolution. Non-noble metals such as Ni, Fe, Co, and their oxides have been employed in alkaline conditions due to their stability. Because of these harsh oxidising conditions, the degradation of OER catalysts is often suggested to be coupled with the OER itself [1, 2, 25, 30, 31, 32]. This also begs the question of whether it is even sustainable to use expensive noble catalysts in the first place. Describing the relationship between the degradation of OER catalyst and the OER itself accurately is an important step towards realising efficient and sustainable hydrogen production through AEM water electrolysis. And here is where modelling can play a key role in gaining insights which are difficult to extract solely by experimental measures.

The dissolution of iridium, and similar noble metals, as OER catalysts is found experimentally to be dependent on the increase in anodic potentials/currents, change in anodic potentials and sweep directions, pH, nature of oxide layer, preparation history, and change in oxidation states[1, 2, 25, 30]. Kasian *et al.*[25] studied the dissolution of iridium and iridium oxide in acidic solutions with different prepa-

ration histories and proposed a two-way mechanism encapsulating how OER and dissolution are coupled. Mayrhofer *et al.* [1, 30] also studied the dissolution of iridium[30] and hydrous iridium oxide [1] with cyclic voltammetry (CV) in acidic solutions and found that the degradation was incited by a change in sweep rate and oxidation states. A similar experiment was conducted by Schalenbach *et al.*[2] under alkaline conditions, and saw the same general trends. Using microkinetic modelling to describe such dissolution trends for iridium oxide during OER conditions, could perhaps be applicable in the modelling of AEM-WE to study qualitatively how degradation of the catalyst layer affects performance.

Through the years there have been similar studies of water electrolysis and fuel cell technology by modelling [16, 33, 34], and there have also been studies where microkinetic modelling has been applied to study the OER both with[29, 35, 36] and without [28, 37] degradation. The microkinetic approach by Marshall *et al.* [28] showed the importance of how quasi-steady-state assumptions can hide important kinetic properties of the OER across potential ranges. Liu *et al.* [33] focused on the role of KOH electrolyte and its effect on AEM-WE performance, and An *et al.* [16] made a mathematical model of an AEM-WE, much like the continuum model from SINTEF [3] used in this thesis. However, both Liu *et al.* and An *et al.* did not incorporate any dissolution into their models. Geppert *et al.* applied microkinetics to study different mechanisms for OER and displayed how different mechanisms can explain the same observations, however, they too neglected dissolution in both cases as well. Lastly, Dam *et al.* [29] aimed to study the coupling of the OER and degradation on rutile iridium oxide, and found how structural differences of the oxide layer affect the dissolution rate and the importance of the nature of the dissolution step.

It is therefore not unreasonable to believe that implementing the dissolution of OER catalyst materials described by microkinetic modelling in a modelling framework, which simulates the operation of an AEM-WE, would yield results closer to real-life observations. Thus, describing the operation of an AEM-WE more accurately, and unifying theory with experiments by means of modelling and simulations. In this work, microkinetic modelling was used to simulate the degradation of IrO_2 in both acidic and alkaline environments based on the dynamic CV measurements from Mayrhofer *et al.* [1] and Schalenach*et al.*[2]. The alkaline model

would then be implemented into a continuum model developed by SINTEF[3] to simulate an AEM-WE with degradation described by microkinetic modelling. Thus, unveiling the effects of degradation during operation of an AEM-WE.

1.1 Electrolyser technologies

Electrolyser technologies, such as the proton-exchange membrane water electrolyser (PEM-WE) [38] and the alkaline water electrolyser (A-WE) [39], are already established technologies [12, 40]. Still, water electrolysis technologies have gained far more interest in recent years following the worlds global goal in lowering the amounts of carbon dioxide in the atmosphere as a response to the adverse effects of climate change [4, 6, 7, 8]. This has led to more research and innovation within renewable forms of energy in order to reach those commitments. One of such areas of interest is hydrogen production. Hydrogen has been a potential substitute for fossil fuels for a long time, there has even been mention of an idea called "Hydrogen society" [41], where hydrogen is the primary source of energy. Still, hydrogen is difficult to utilize, store efficiently, and lastly produce efficiently among other aspects [41]. One of the more promising, but not yet commercially available, water electrolyser technology is the up-and-coming anion-exchange membrane water electrolyser (AEM-WE) [9, 12, 15, 17, 33, 42]. Water electrolysis is a viable option for sustainable, energy-, and cost-effective production of hydrogen, though it has some limitations [11].

Water electrolysers split water electrocatalytically into hydrogen and oxygen through the hydrogen evolution reaction (HER), and the oxygen evolution reaction (OER) [38, 42]. These reactions happen at separate electrodes, but they are connected through an outer circuit. The current water electrolysis technologies will be introduced within the next sections

1.1.1 PEM water electrolysers

PEM-WE is one of the most commercial and well studied water electrolyser technologies on the market because of its high voltage efficiency and high operational current density [38, 42]. The name *proton-exchange membrane* water electrolyser insinuates an interplay between protons (H^+) and a membrane. PEM-WE relies on an acidic membrane which separates the anode and cathode compartments from each other. This acidic membrane also conducts protons, making it a solid

electrolyte, and at the same time, keeps the oxygen and hydrogen produced at the different compartments separated [9, 12, 38], see reaction 1.1 and 1.2. Since the proton is the only ion that travels between two compartments, due to the membrane, it is also the charge carrier for the PEM-WE [38]. This means that the proton carries the current with its movements from one side to the other, and this way closing the circuit.

The overall reaction for the splitting of water in a PEM-WE can be seen in reaction 1.3. Reaction 1.3 is the sum of the two half-reactions mentioned earlier, the HER and the OER. Water is split according to the OER at the anode, reaction 1.2, and produces protons. These protons then travel through the membrane to the cathode and create hydrogen through the HER at the cathode, reaction 1.1. [38]

$$\textit{Cathode}: \quad 4\,H^+(aq) + 4\,e^- \rightleftharpoons 2\,H_2(g) \qquad E_c^\circ = 0 \text{ Vvs SHE[43]} \tag{1.1}$$

$$\textit{Anode}: \quad 2\,H_2O(l) \rightleftharpoons 4\,e^- + 4\,H^+(aq) + O_2(g) \qquad E_a^\circ = 1.23 \text{ Vvs SHE[43]} \tag{1.2}$$

$$\textit{Overall}: \quad 2\,H_2O(l) \rightleftharpoons 2\,H_2(g) + O_2(g) \qquad E_{cell}^\circ = -1.23 \text{ Vvs SHE} \tag{1.3}$$

The electrocatalytic water splitting requires electrocatalysts, meaning catalysts that can increase the rates of electrochemical reactions occurring on surfaces [44]. Such catalysts need to be both stable and have increased activity towards the desired reaction. The presence of protons in the membrane as well as at the surface of the electrodes makes the environment acidic and puts a high demand on catalysts [9, 12, 38]. In addition, the catalyst materials must also withstand high applied voltages [12, 38]. These harsh conditions make the list of viable catalyst materials thin [12, 18, 38]. The most common catalyst materials used in PEM-WE are noble catalysts such as Pt, Ir, Ru, and their oxides, these are often called platinum group metals, or PGM for short [38]. Iridium or iridium oxide is often chosen as a catalyst material for the OER in PEM-WE because of its high stability and relatively high activity towards the OER [1, 30]. The sluggish kinetics of the OER and the use of scarce catalyst materials are some of the major drawbacks for the PEM-WE [12].

1.1.2 Alkaline water electrolysers

Alkaline water electrolysers are perhaps the most mature water electrolysis technology of the three because of their long history [38] and the use of inexpensive catalyst materials [9, 12, 18]. As the name suggests, this water electrolyser is using an alkaline electrolyte, usually concentrated aqueous KOH solutions [9, 12, 14, 18]. The anode and cathode compartments are separated by a porous diaphragm which separates the product gasses H_2 and O_2. This diaphragm, however, does not in itself have any intrinsic ionic conductivity; the conductivity is supplied by the circulation of the KOH-filled electrolyte which passes through the diaphragm along with OH^- [9, 17]. Subsequently, the diaphragm leads to large ohmic losses, resulting in lower operational currents and make it hard to operate with differential pressure [12, 13].

The half-reactions for the A-WE are still HER and OER, but because of the alkaline environment caused by the electrolyte, the half-reactions are a bit different than the ones presented in the previous section. Reaction 1.4 and 1.5 represents the HER on the cathode and the OER on the anode in an alkaline environment respectively [12]. A-WE is still a water electrolyser technology, so the overall reaction is identical to that of the PEM-WE, compare reaction 1.6 to reaction 1.3. Analogous to the role of the proton for the PEM-WE, the hydroxide ion is transported between the compartments in the A-WE, but because of the opposite charge of the OH^--ion compared to the proton, it moves in the opposite direction, meaning from the cathode compartment to the anode compartment [38].

$$\begin{aligned} \textit{Cathode}: \quad & 4\,H_2O(l) + 4\,e^- \rightleftharpoons 4\,OH^-(aq) + 2\,H_2(g) \\ & E_c^\circ = -0.83 \text{ Vvs SHE[43]} \end{aligned} \tag{1.4}$$

$$\begin{aligned} \textit{Anode}: \quad & 4\,OH^-(aq) \rightleftharpoons 4\,e^- + 2\,H_2O(l) + O_2(g) \\ & E_a^\circ = 0.41 \text{ Vvs SHE[43]} \end{aligned} \tag{1.5}$$

$$\begin{aligned} \textit{Overall}: \quad & 2\,H_2O(l) \rightleftharpoons 2\,H_2(g) + O_2(g) \\ & E_{cell}^\circ = -1.23 \text{ Vvs SHE} \end{aligned} \tag{1.6}$$

Contrary to the PEM-WE, the environment in the electrode compartments is alkaline, and not acidic. This enables the use of less scarce materials such as

Co, Ni, and Fe and their oxides to be used as catalyst materials due to their increased activity towards HER and OER[9, 17]. The stability and abundancy of these metals make it more desirable to upscale the production, but the A-WE still suffers from lower efficiency and limited current density due to some cross-diffusion of the product gasses between the chambers [12, 15, 38], high ohmic losses across the electrolyte due to the presence of the porous diaphragm [12], and low operating pressures [12]. The general kinetics for the A-WE is also slower compared to that of the PEM-WE because of the lower conductivity of OH^- in the A-WE, and the larger ohmic losses [12].

1.1.3 AEM water electrolysers

Lastly, the anion-exchange membrane water electrolyser aims to combine the advantages of both the PEM-WE and the A-WE [9, 12, 14, 16, 17, 33]. It is still in its early stages, and yet it has the potential to produce hydrogen in large scales, cost- and energy efficiently. Like the alkaline water electrolyser, the AEM water electrolyser can potentially utilise more abundant catalyst materials because it too operates under alkaline conditions [9, 14, 15, 17, 18]. Replacement of the PGM catalyst materials lowers the cost drastically compared to PEM-WE. Though the electrolyte itself is alkaline, it shows more resemblance to the operation of the PEM-WE, in the regard that it has a nonporous polymer membrane which also acts as a separator between the electrode compartments [12, 40], meaning no diaphragm. The Anion-exchange membrane (AEM) permits the AEM-WE to operate without circulating a caustic liquid electrolyte between the two compartments. Analogous to the proton exchange membrane (PEM) in the PEM-WE, the AEM also provide the anionic conductivity for the hydroxide ion with its intrinsic ionic conductivity [12, 14, 15, 33]. The AEM-WE can still be run with circulating caustic electrolytes like $1\,\mathrm{mol\,L^{-1}}$ or $5\,\mathrm{mol\,L^{-1}}$ KOH[17, 45]. However, using a concentrated corrosive alkaline electrolyte is a disadvantage to membrane-based AEM-WEs, though using pure water instead has shown much lower performance [18]. Some operational parameter for AEM-WE are given in Table 1.1.

Table 1.1: Some operating parameters for anion-exchange membrane water electrolysis

Parameter [unit]	Value	Ref
T [°C]	$60 - 85$	[17]
c_{OH^-} [mol L^{-1}]	$0.1 - 5$	[17, 45]
i [A cm^{-2}]	$1.8 - 5.3$	[17, 46]
E_{Cell} [V]	1.8 - 2	[17, 46]
p [Pa]	$1.013 \cdot 10^5$	[16]
Life time [h]	<3000	[46]

A simplified figure of an AEM-WE is shown in Figure 1.1 and is meant to represent the AEM-WE which is being modelled by the framework provided by SINTEF [3]. The figure shows that both the anode and cathode consist of a porous transport layer (PTL) and a catalyst layer (CL) as well as bipolar plates (BP). In addition, the AEM is placed between the two electrode compartments, and the anode and cathode CL along with the AEM is often referred to as the membrane electrode assembly (MEA) [3, 15]. Inside the AEM in Figure 1.1, it is emphasised that the hydroxide ions are travelling from the cathode compartment, where they are created through the HER, see reaction 1.4, to the anode compartment where they react to form oxygen through the OER, see reaction 1.5 [9]. The HER and OER are also displayed in Figure 1.1 in their respective electrode compartments. From the schematic, one can see that there is also the presence of other ions, like K^+, but they are prevented from crossing over by the AEM, and is a part of the electrolyte KOH solution providing hydroxide ions. The oxygen and hydrogen being produced are transported out of the cell by the anode and cathode PTL respectively. Though it is not represented in Figure 1.1, there is also an ionomer present, see Figure 1.2, ensuring ionic transport between both the cathode and anode CL, and the AEM. Moreover, the ionomer is also responsible for making the active sites for the electrochemical reactions more accessible for reactants, increasing the reaction rate [15]. Introduction of the AEM and the presence of an ionomner within the CLs can, in theory, remove the need for a caustic electrolyte solution like KOH or K_2CO_3 [13, 16, 17, 18, 40], but this may also lead to lower activity [15]. The modelling framework developed by SINTEF [3] does in fact simulate an operating AME-WE with a KOH solution and an ionomer.

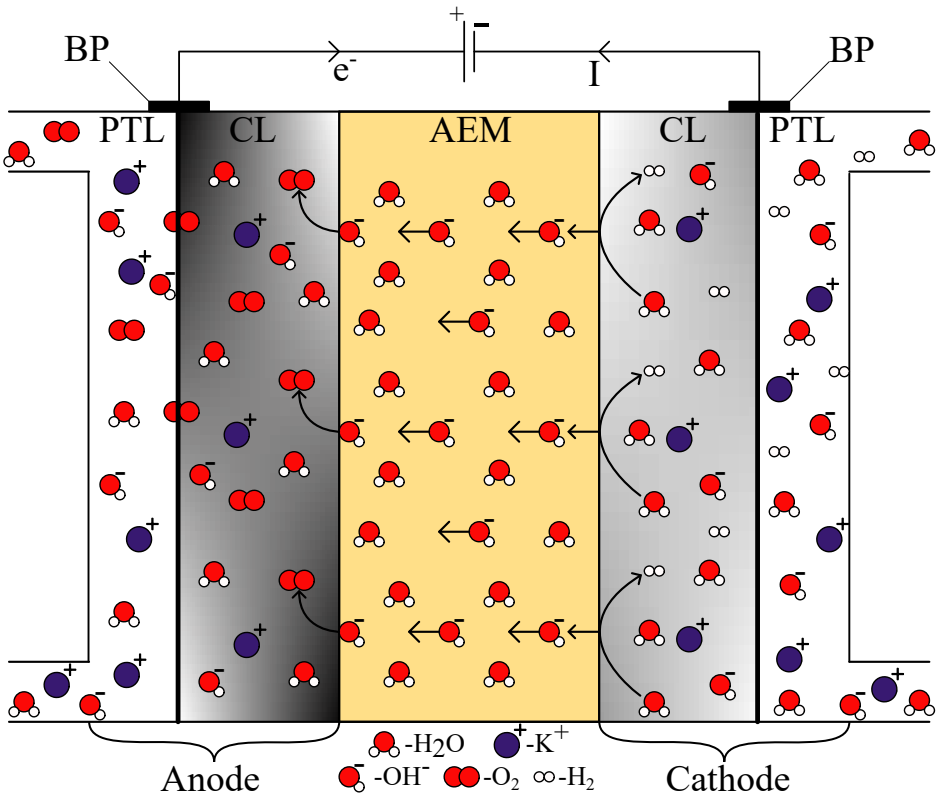

Figure 1.1: An anion-exchange membrane water electrolyser (AEM-WE). The figure shows that both the anode and the cathode is comprised of a porous transport layer (PTL) and a catalyst layer (CL), which is also porous. Additionally, the bipolar plates (BP), which collect the current, are also displayed, along with the voltage source and the direction of both electrons, e^-, and current, I. The anion exchange membrane (AEM) is sandwiched between the two CLs, and as the figure shows, it only lets hydroxide ions, OH^-, through. It can also be seen that oxygen gas, O_2, is produced at the anode and hydrogen, H_2 at the cathode.

The CLs are porous with an ionomer providing more surface area per volume catalyst, increasing the surface area available for reactions [3, 16, 47]. Usually, the electrode compartments are flushed with KOH electrolyte [18, 40], and this too is the case for the modelling framework by SINTEF [3]. The KOH, ionomer, and the AEM ensure ionic conductivity throughout the MEA, see Figure 1.2. HER is occurring within the cathode CL through reaction 1.4 where water is reduced into hydrogen and hydroxide ions upon reacting with electrons coming from the outer circuit. Then, the hydroxide ions travel from the cathode CL, through the AEM, to the anode CL where the hydroxide ions get oxidised into oxygen and water according to reaction 1.5. In the creation of oxygen, the hydroxide ions also generate electrons which are then transported via the external circuit. The direction of the electrons is given in Figure 1.1.

The electrochemical reactions for the AEM-WE, see reaction 1.4, 1.5, and 1.6 are limited to occur at catalyst sites where there is access to electrons, water, and hydroxide ions [3, 15]. These catalytic sites are referred to as *electrochemically active sites*. Such active sites are illustrated in Figure 1.2 as catalyst particles, black, partially covered in ionomer, yellow, making what is not covered in ionomer exposed to the electrolyte. This is also called a three-phase boundary [15] where the catalyst particle provides a pathway for the electron, the ionomer ensures a pathway for hydroxide ions with its ionic conductivity, and the pore electrolyte provides water [48]. Figure 1.2 is meant to visualise how the ionomer is present in the anode CL since the scope of the project is limited to the study of the anode catalyst layer, though the ionomer is present across the AEM and in the cathode CL too.

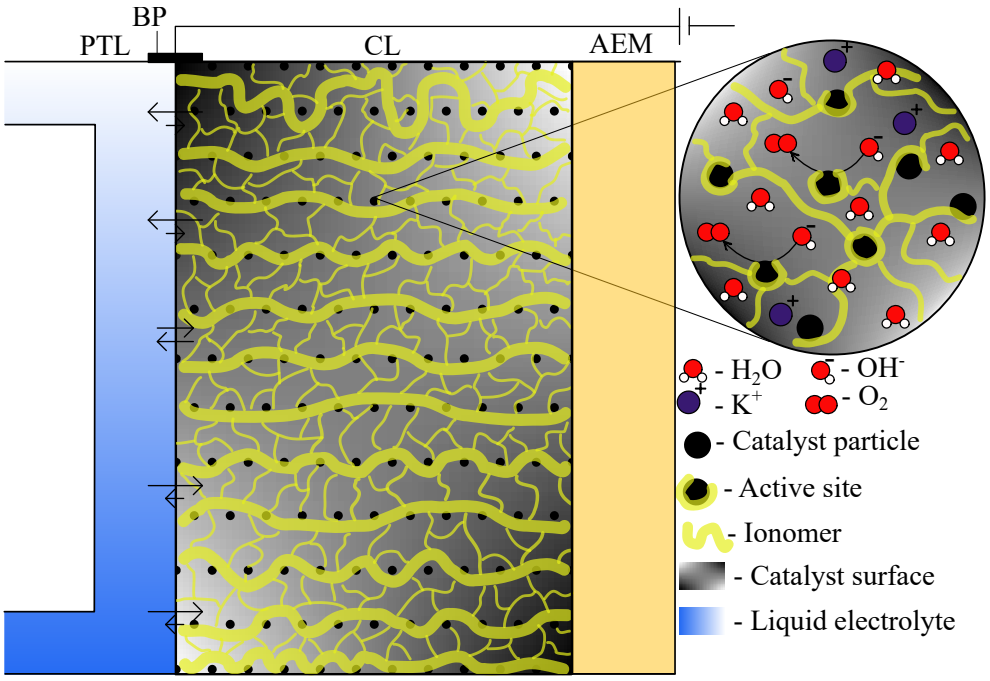

Figure 1.2: The anode side of the anion-exchange membrane water electrolyser (AEM-WE) with porous transport layer (PTL), bipolar plates (BP), anode catalyst layer (CL), and lastly the anion-exchange membrane (AEM) with emphasis on a specific part of the CL. The zoomed-in circle represents a local microscopic area where active sites are visible as catalyst particles in contact with an ionomer, two reactions on active sites are also illustrated to emphasise the importance of the active sites in the CL

As stated earlier, the goal of a commercial AEM-WE is to take the advantages from both the PEM-WE and A-WE. However, it still needs innovation when it

comes to power efficiency, handling, reduction in cell cost, and lastly membrane and catalyst stability [9, 42]. This project focuses on the latter, catalyst stability for the anode catalyst material under OER conditions. The common limitation for all three of the water electrolysis technologies and water electrolysis, in general, is the sluggish kinetics of the OER [15, 32, 42], though the OER activity can be somewhat higher in alkaline environment [15]. Compared to the HER, the OER is also quite complicated including a four-electron transfer [15]. Finding a stable, active, and cheap electrocatalyst is no easy feat, and there is an extensive effort in catalyst research [9, 15, 42, 49]. Ir and Ru and their respective oxides are popular choices due to their activity towards the OER [12, 42], but both lack long-term stability in alkaline conditions [42]. Even though the AEM can utilise non-PGM catalysts, IrO_2 is chosen as the model catalyst material for this project since it is used as a benchmark for electrocatalysts towards OER. There is also a lot of data on iridium oxide regarding OER and degradation [1, 25, 27, 29, 30, 31, 37, 50, 51] and because of the available data and proposed mechanisms, the mechanism for degradation of iridium oxide is studied.

2 Theory

2.1 Electrocatalysis

The electrochemical reactions occurring in the AEM-WE, and electrochemical reactions in general, usually occur at the interface between the electrolyte and the electrode on the surface of the electrode [44, 52, 53]. If the surface acts as a catalyst for the electrochemical reaction, then the electrode is an electrocatalyst. The catalysis can also be referred to as *heterogeneous catalysis* since the electrode surface is a different phase than the electrolyte [53, 44][54, p. 15]. Figure 2.1 is an example of the OER on the surface of a catalyst. Electrochemical reactions are associated with the transfer of electric charge between the electrolyte/electrode interface where the charge carriers in such reactions can be either ions or electrons [44, p. 339-341]. The dissolution of electrode material, as will be discussed later in section 2.3, is an example of an electrocatalyst not catalysing the wanted reaction. In this case, the wanted reaction is not catalysed and the catalyst is instead participating in another reaction leading to the surface of the electrocatalyst being altered in the end, see Figure 2.3. The surface orientation also plays a role in the catalysis of reactions, for instance, the (110) crystal plane for rutile IrO_2 was found to be more stable, but less active than the (100) plane towards the OER [19, 55]. Moreover, whether the layer is monocrystalline, amorphous, hydrous, anhydrous, reactively sputtered or thermally prepared has a lot to say for the stability and the activity towards the desired reaction [1, 25, 29, 30, 42]. The difference in activity and stability can indicate different mechanisms altogether due to the surface chemistry [1][44, p. 339-341]. The driving forces for regular heterogeneous catalysis are parameters like surface concentration, temperature, and pressure, but electrocatalysis is also affected by the potential drop at the electrode surface [44, p. 339-341]. This means that the potential across the electrocatalyst can affect the rate of a reaction occurring on the surface, and this is utilised in the electrocatalytic splitting of water to increase the rate of the desired reactions, namely the OER and HER.

The activity of the electrocatalysts is largely decided through the binding energy of the reactants adsorbed onto the surface [56]. Plotting an activity descriptor against binding energy, or descriptors easier to measure since binding energies

seldom are accessible, will give rise to a volcano plot[26], which is often used to compare activities for different electrocatalysts. Iridium oxide is often found around the top of the volcano plot[57] for electroactivity towards OER, and hence often regarded as an excellent OER catalyst. The Sabatier principle is usually used as a qualitative description of how an ideal catalyst should be, and it says that *the catalysts should not bind themselves to the adsorbates too strongly nor too weakly* [58]. The principle states that if the reactant is bound too weakly then the reactant won't interact with other adsorbates on the surface, or if it is bound too strongly, then it will have a hard time desorbing from the surface, and thus inhibit further reaction[56].

Electrochemical reactions occur on electrode surfaces, and experimentally it is often observed that electrochemical reactions either do not occur, or they do occur, but at very low rates for certain electrode materials [44, p. 339]. The role of the catalyst is to increase the rate at which the surface reactions happen by altering the reaction mechanism to be more favourable compared to the situation without a catalyst[54, p. 39]. Usually, the catalyst lowers the activation energy needed for the specific reaction, because the reaction mechanism changes accordingly, and that way, increasing the rate of reaction[54, p. 41]. For water electrolysis, it is specifically the OER that limits the efficiency of hydrogen production with its sluggish kinetics. It is therefore desirable to have a catalyst that increases the reaction rate for the OER under the relevant conditions. Another criteria for the electrocatalyst, or catalysts in general, is to not be consumed during reaction [44, p. 339][54, p. 10], and this is a problem regarding the OER electrocatalysts. The electrocatalysts used for OER in water electrolysis technology show some degree of dissolution, be it either noble or non-noble catalyst material, alkaline or acidic environment[1, 2, 29, 30, 32, 27]. This is especially unfortunate when metals such as Ir and Ru and their oxides are regarded as the most active catalysts for the OER, and yet they still suffer degradation [1, 30, 49, 27]. Usually, the oxides of such metals show smaller degradation, and higher stability, than their metallic counterparts, but the metallic catalysts also show more activity[50]. Cherevko *et al.*[50] found that the activity for OER increased as $IrO_2 < RuO_2 \approx Ir < Ru$ in acidic media. An opposite trend for the same compounds was also observed for the stability of the same compounds as $IrO_2 \gg RuO_2 > Ir \gg Ru$ during OER conditions [50]. A similar study by Cherveko *et al.* [27], studied several

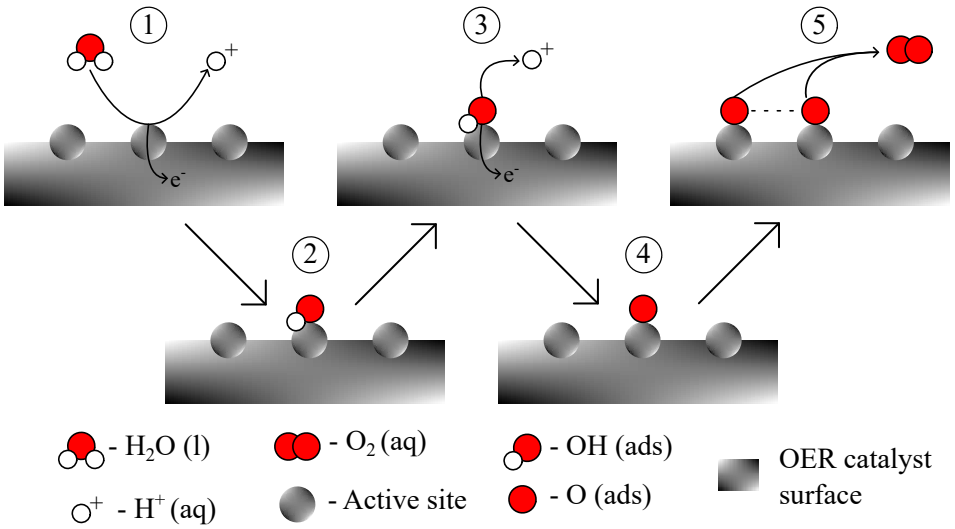

Figure 2.1: An example of the OER mechanism on the surface of an electrocatalyst where the catalyst is not consumed, nor is the surface changed at the end of the reaction. The figure can also, in a way, describe the reaction mechanism for OER on thermally prepared IrO_2 proposed by Kasian *et al.* [25] and written in section 2.6 as step 3.1 - 3.2 - 3.4. In addition it is also a representation of the electrochemical oxide path formulated by Bockris *et al.* [59] described in section 2.2

noble metals and observed that the activity towards OER was increasing like Au < Pt < Pd < Rh < Ir < Ru. In alkaline conditions, Schalenbach *et al.* [2] conducted similar measurements of noble metals as Cherevko *et al.* [27], and found that the activity towards OER at $i = 4\,\mathrm{mA\,cm^{-2}}$ increased as Au < Pt < Pd < Ag < Rh < Ir < Ru, which follows the same pattern.

Figure 2.1 displays a mechanism for a half-cell reaction occurring on the surface of an electrode, where the electrode has active sites where species can adsorb onto so that reactions can occur [44, p. 207-208][53]. An active site on a surface is usually a microscopic area on the surface that differs from the rest of the surface, such as atomic clusters, flat planes, edges, defects, and more [44, p. 207-208]. Such active sites play a huge role in the kinetics of electrochemical reactions where adsoprtion is a prerequisite for reactions to occur, such as illustrated in figue 2.1. The mechanism is an example of the OER in acidic environment as described by Kasian *et al.*[25].

2.2 Oxygen evolution reaction

The oxygen evolution reaction, see reaction 1.2 for acidic and 1.5 for alkaline, is the electrochemical reaction in water electrolysis taking place at the anode. While the HER has relatively fast kinetics on platinum based cathodes [36], the OER, on

the other hand, suffers from sluggish and poor kinetics with high overpotentials required to promote the OER at the anode[27, 28, 31]. Lowering the overpotentials for the OER and improving the kinetics is therefore of high interest for increasing the energy efficiency for hydrogen production through water electrolysis. Consequently, the preparation of adequate catalysts is important for improving the kinetics and driving the overpotential related to OER to a minimum. Because of the harsh reaction conditions related to the OER in low-temperature WE, like high overpotentials in very alkaline or acidic environment, there is a lot of constraints on viable catalyst materials regarding both high activity towards OER, but also high long-term stability, making the list of catalyst materials thin. Even though model catalyst materials based on PGMs like Ir and Ru and their oxides are regarded as excellent catalysts, they still suffer from degradation under OER conditions, and lack long-term stability in both alkaline and acidic environment [2, 27, 42, 50].

The mechanism for the OER has been under heavy discussion and is poorly understood. Understanding the mechanism of the OER on different materials is paramount for creating good electrocatalysts [26]. It is a rather complex reaction involving four electrons and four hydroxide ions/protons depending on the environment, see reaction 1.5 and 1.2. Geppert *et al.* [36] lists four mechanisms for OER on iridium surfaces, where they also involve dissolution steps. Usually, the OER mechanism does not include dissolution, for example, Bockris *et al.* [59] have proposed two different paths for OER on a general catalyst surface. These two paths are the electrochemical oxide path

$$\mathrm{S} + \mathrm{H_2O(l)} \rightleftharpoons \mathrm{S{-}OH} + \mathrm{H^+(aq)} + \mathrm{e^-} \tag{2.1}$$

$$\mathrm{S{-}OH} \rightleftharpoons \mathrm{S{-}O} + \mathrm{H^+(aq)} + \mathrm{e^-} \tag{2.2}$$

$$\mathrm{S{-}O} \rightleftharpoons \mathrm{S} + \frac{1}{2}\mathrm{O_2(g)} \tag{2.3}$$

and the oxide path

$$\mathrm{S} + \mathrm{H_2O(l)} \rightleftharpoons \mathrm{S{-}OH} + \mathrm{H^+(aq)} + \mathrm{e^-} \tag{2.4}$$

$$2\,\mathrm{S{-}OH} \rightleftharpoons \mathrm{S{-}O} + \mathrm{H_2O(l)} \tag{2.5}$$

$$2\,\mathrm{S{-}O} \rightleftharpoons 2\,\mathrm{S} + \mathrm{O_2(g)} \tag{2.6}$$

where S alone denotes an active site on the catalyst surface, and S−OH and S−O represent OH and O adsorbed onto a site respectively. The mechanism in Figure 2.1 is an example of the electrochemical oxide path which occurs on active sites on the surface of a catalyst layer. A different type of mechanism altogether has even been found experimentally and researched by computational methods, where the lattice oxygen in the crystal lattice on the surface participates directly in the OER [29, 31, 32, 60, 61, 62]. It is often called *lattice oxygen evolution reaction*, LOER, by Binninger *et al.* [32] and Dam *et al.* [29], while it is dubbed *lattice oxide oxidation mechanism*, LOM, by Wang *et al.* [60] and *lattice oxygen participated mechanism*, also LOM, by Rong *et al.* [61]. This mechanism will be called LOER from here on out. Wang *et al.* [60] even hypothesize that this mechanism can bypass the traditional rate-determining step for the OER mechanism via adsorption and therefore increase the effectiveness of the OER by promoting this type of mechanism. The study of this type of mechanism is outside of the scope of this project, but it should be kept in mind.

Oxygen evolution on iridium and iridium oxide surfaces depends on the preparation history, the pH, the available surface, and the potential to name a few. Kasian *et al.* [25] studied the degradation of metallic Ir and its oxides in acidic solutions and found two paths for the OER. The most favourable pathway depended on whether the iridium oxide was formed by thermal treatment, was reactively sputtered, or produced during short polarisation of the metallic Ir surface, and also on the anodic potential. The different oxides experienced different degradation and hence two separate OER pathways were hypothesised and described in the Supporting material [63] and also given in Appendix B. Both the activity and stability of iridium oxide depend heavily on the surface chemistry[1, 19, 26, 55, 30]. As mentioned earlier, crystal orientation has an effect on electrocatalytic activity, and Lee *et al.* [19] compared the (100) plane for both rutile IrO_2 and columbite IrO_2 and found that they displayed different activities towards OER. In addition, Stoerzinger *et al.* [55] found that the electrocatalytic activity towards OER for the (100) plane on iridium oxide showed greater activity than the more stable plane (110) in alkaline environments. However, monocrystalline electrocatalysts are seldom used as catalysts towards OER, and usually, the electrodes have more porous structures to promote intimate contact with the electrolyte [52]. To follow up on this, Du *et al.* [42] state that the electrolytic activity towards OER is

greater for amorphous iridium oxide, IrO_x, and hypothesise that may be related to the more porous structures of hydrous and amorphous iridium oxides, especially in acidic environments[36]. On the contrary, consistent baseline data for OER activity on iridium and iridium oxide in alkaline environments are rare and often quite different than that of acidic environments[30, 42].

2.3 Catalyst degradation

Electrocatalysts, and catalysts in general, will deteriorate over time. The rate of this degradation is of high importance when it comes to electrocatalysts, especially when it comes to the use of noble and expensive PGM materials, such as iridium. Over time, the efficiency of the catalyst layer will decrease, mainly because of the catalytic surface changes either in the form of dissolution or by changing the structure. Hence, the frequency of replacing the catalyst layer is crucial when it comes to the economic perspective of hydrogen production. As mentioned earlier, because of the harsh conditions related to the OER, the catalyst is put under a lot of stress, and the list of viable catalysts is thin. There are few catalysts which show long-term stability, but even noble catalysts such as iridium display degradation under OER conditions.

Most of the investigated oxides for anodic catalysts for the OER undergo substantial corrosion [32]. Binninger *et al.* [32] have explained a universality in the correlation between oxygen evolution activity and corrosion of oxides through fundamental thermodynamic concepts independent of the pH by assuming that the autoprotolysis of water holds[i]. Wohlfahrt-Mehrens & Heitbum [62] among others[31, 51, 64] have also reported lattice oxygen from the crystal lattice of the metal oxide in the evolved oxygen amongst the corrosion phenomena by the use of isotope labelling. This was mentioned in the last section as a different form for OER mechanism, and one of which dominates in hydrous oxide [29]. In addition, degradation by the dissolution of metal cations from the catalyst surface is also observed [25, 27], and this degradation does not participate in the production of oxygen in the OER. These are two examples of altering and degradation of the catalyst surface, which affects the activity towards OER for the anodic catalyst layer.

By the use of thermodynamic principles, Binninger *et al.* [32] have explained why

metal oxides, often used as catalyst materials, experience corrosion during OER conditions. The reason is the thermodynamic instability of the oxygen anion in the metal oxide [32]. They have derived the concept based on alkaline conditions, but by assuming that the chemical equilibrium of the water autoprotolysis[i] holds, the result is independent of the pH and is equally valid for acidic environments. Their results include the diffusion of cations from the surface, but does not exclude dissolved ions, see Figure 2.3. Furthermore, it also includes the LOER mechanism of OER as well. Their work concludes with an impossibility of a thermodynamically stable metal oxide under OER conditions, regardless of the pH because of the instability of the oxygen anion in the metal oxide lattice. This implies that the degradation and OER might be coupled and that degradation might even be triggered in some cases by the onset of OER [25, 31, 63]. Their findings imply that since the degradation of catalyst might be unavoidable, the study of the rate of degradation is paramount. In addition, their findings do not contradict the predictions of the Pourbaix diagram, Figure 2.2, which tells which phase of the metal is *most stable* under defined pH - potential regimes. From the Pourbaix diagram in Figure 2.2, one can see that in alkaline conditions and high potentials, as there are in AEM-WEs, the most stable phase of iridium in contact with water is indeed the dissolution product IrO_4^{2-}. In acidic conditions, however, Ir is stable up until around 0.9 V vs SHE, where it forms a protective oxide layer and becomes IrO_2. IrO_2 is resistant to corrosion up until around 1.3 V vs SHE where it then forms IrO_3. Still, Mayrhofer *et al.* [1, 25, 30, 31] still report dissolution of iridium oxide, in line with the correlations described by Binninger *et al.* [32] for higher potentials and acidic conditions.

[i] The waters autoprotolysis is the chemical equilibrium described by

$$H_2O(l) \rightleftharpoons H^+(aq) + OH^-(aq)$$

which describes water's ability to self-dissociate into protons and hydroxides [65]. In addition, the ionic product for water gives the relationship between the protons and the hydroxides and is described as

$$K_W = a_{H^+} a_{OH^-}$$

where K_W is the ionic product for water and is a function of the temperature, but at room temperature, the ionic product is $K_W = 10^{-14}$. This relation can be used to transform reactions from acidic conditions to alkaline conditions

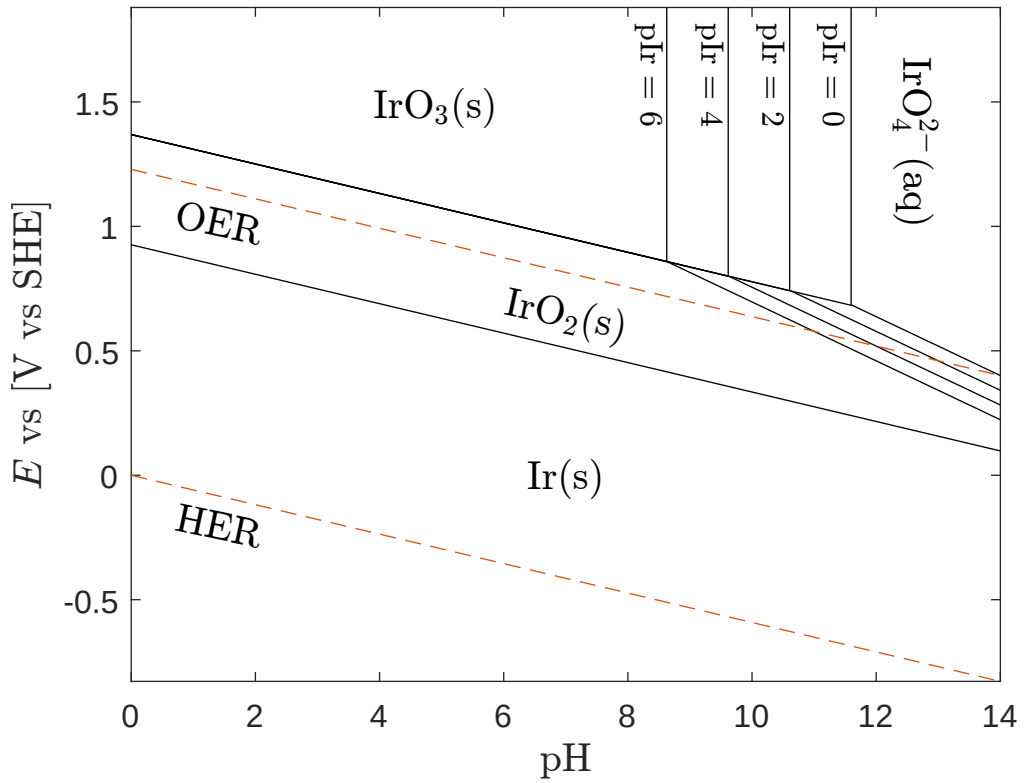

Figure 2.2: A simplified Pourbaix diagram of Ir in contact with water based on the values from Pourbaix [66] and *Material Explorer* app [67, 68, 69, 70, 71, 72, 73, 74, 75, 76, 77, 78, 79, 80]. It is based on data measured by Pourbaix, and also from the DFT calculations from the *Material explorer* from *Materials Project*[81]. Activities, assumed to be equal to concentrations, for IrO_4^{2-} creates the extra lines marked with $p\mathrm{Ir} = \{0, 2, 4, 6\}$ separating IrO_4^2 from IrO_3(s) and IrO_2(s). $p\mathrm{Ir} = 0$ is the same as setting the concentration equal to $1\,\mathrm{mol\,L^{-1}}$, and hence setting the activity to unity. The derivation of the Pourbaix diagram is given in Appendix A.

Figure 2.3 shows an electrocatalyst which degrades. It shows the same procedure as Figure 2.1 up until point four, the adsorbed oxygen on the active site. Contrary to the mechanism which is displayed in Figure 2.1, where the catalyst surface is left unchanged and oxygen is produced, this mechanism displays degradation of the catalyst layer by the dissolution of an active site away from the catalyst surface, leaving the catalyst surface changed and with one less active site available for OER. Figure 2.3 can in a way display the reaction pathway of dissolution of IrO_2 as described in reaction 3.5/3.18 and is different from that of the LOER where oxygen is produced as well.

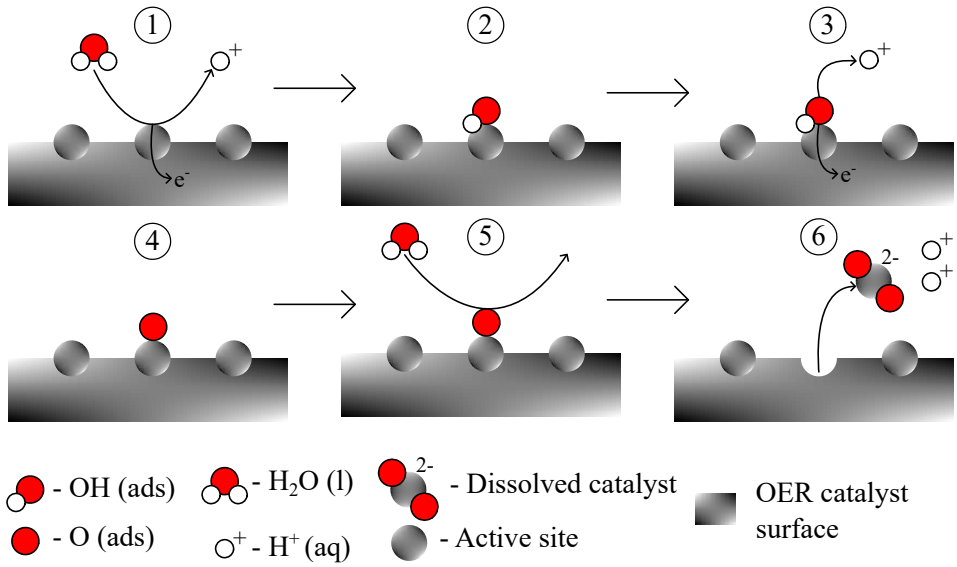

Figure 2.3: An electrocatalyst which participates in a reaction mechanism, and is spent/altered such that one of the active sites leaves the OER catalyst surface via dissolution route. The end result is a changed catalytic surface with fewer active sites and thus lower activity towards OER since there now are fewer sites where reactions can occur. This figure can also, in a way, represent the dissolution pathway described by Kasian *et al.* [25] which is written in section 2.6 as step 3.1 - 3.2 - 3.3

The mechanism mentioned in Section 2.2, where the oxygen in the metal oxide lattice participates directly in the OER[29, 32, 60, 61], dubbed LOER here, is an example of catalyst degradation that promotes the OER, but sacrifices long-term stability. Even though this mechanism can supposedly bypass common rate-determining steps and increase the efficiency of the OER [60], it is not certain if this type of mechanism is sustainable due to the reconstruction of the catalyst surface. It is shown that this type of mechanism does occur in an acidic environment for IrO_2 [51, 60]. It was mentioned that Dam *et al.* stated that the activity towards OER is greater for hydrous oxides compared to dry oxides in Section 2.2, but this may also be related to the presence of hydroxides within the hydrous catalytic layer, promoting the LOER mechanism. There is usually a trade-off between high electrolytic activity towards OER and stability during OER [55]. The conclusions from Danilovic *et al.* [82] suggest that an electrocatalyst for the OER should balance activity and stability as a consequence of their reverse proportionality and states the catalyst should not dissolve too fast nor too slow.

Generally, electrocatalyst degradation is a transient process[30]. It is usually initiated by a change in oxidation state, both by reduction and oxidation on the surface. The oxidation states of metals change continuously during non-

equilibrium processes, like polarisation, under OER conditions. This implies that the metal cations on the surface are prone to dissolution due to their constant change in oxidation states, which makes dissolution rate a function of kinetics and mechanisms[2]. Because of the kinetic effects from the OER, the real onset potential for dissolution and also the potential dependency on the rate of dissolution cannot be captured by a Pourbaix diagram which is described purely by thermodynamical principles in the absence of other factors [53, p. 116][2]. In addition to the potential dependency, the dissolution kinetics are also affected by the physiochemical properties of the catalyst and the operating conditions [83]. For instance, the Pourbaix diagram does not differ between hydrous and anhydrous oxide layers, which makes the stability of the different oxide layers under different OER conditions not represented in a Pourbaix diagram. However, the Pourbaix diagram is still a useful tool to predict if corrosion is possible under certain conditions.

2.3.1 Degradation of IrO_2

The studied dissolution is based on the mechanism proposed by Kasian *et al.* [25] for thermally prepared iridium oxide described in section 3.1 and also rewritten in Appendix B. The same mechanism is assumed to apply in alkaline conditions and explained in Section 3.2. The dissolution reaction in question is given in reaction 3.5 and 3.18 and describes a pathway of the OER mechanism which does not lead to oxygen production, but rather a change in catalytic surface. Figure 3.1 illustrates how the degradation mechanism for dissolution does not lead to oxygen production, and Figure 2.3 shows a simplified degradation mechanism which resembles that of Figure 3.1, where the catalyst surface is left altered.

Usually, there is a trade-off between OER activity and stability against corrosion arising from different types of iridium and iridium oxides such as hydrous oxides, anhydrous oxides, reactively sputtered oxides, single crystal surfaces, polycrystalline surfaces, etc. [1, 30, 31, 35, 55]. In the research done by Mayrhofer *et al.* [1, 30], they compare the degradation of metallic iridium and hydrous iridium oxides. Hydrous iridium oxide is known for its superior OER activity, but at the same time suffers from poor stability [1], though metallic iridium displays a larger dissolution rate than oxidised iridium [27, 1]. At the same time, Du *et al.* [42] reports that the activity for amorphous and hydrous iridium oxides, IrO_x, shows greater activity towards OER than rutile and crystalline iridium ox-

ide, but also worse stability. Stoerzinger *et al.* [55] studied how the orientation of crystalline IrO_2 and RuO_2 and found that the (100) plane for both was more electrocatalytically active towards OER than the more thermodynamically stable plane (110) for both in alkaline conditions (pH = 13). They too also argue that the formation of a hydrous layer contributes to the increased activity [55]. Another article by Kasian *et al.* [31] explores the participation of the surface oxide in both the OER and the degradation of the catalyst layer. They also found that, unlike rutile, hydrous iridium oxide containing IrOOH- species directly affected the oxygen evolution from the lattice at the surface. These species is also included in the reaction mechanism displayed earlier. In addition, this oxygen evolution led to faster dissolution and degradation of the iridium. In turn, this mechanism for the OER also displayed more involvement for oxygen catalysis in the near-surface bulk region for the hydrous oxide, compared to the rutile IrO_2 which only involves the active sites on the outermost layer for both reaction mechanisms.

Now, for the Iridium oxide, there is still a lot of debate about how the OER mechanism, and subsequently the degradation process in fact do occur. As mentioned earlier, the degradation mechanism is dependent on the type of oxide, alkaline or acidic conditions, as well as the applied potential. For this study, the proposed mechanism by Kasian *et al.* [25] which was most favourable for thermally formed oxides was chosen and assumed to be the most dominant mechanism. Such thermal oxides are usually called "dry" based on the temperature, while electrochemically grown oxides usually are hydrous, which affects both stability and activity [1]. The mechanism is described in section 3.1 and the other half of the mechanism, most favourable towards reactively sputtered, electrochemically grown, and metallic iridium is given in Appendix B where the dissolution product is Ir^{3+}. Their study focuses on common intermediates for OER and degradation, which for this study is IrO_2OH and IrO_3 [25]. By taking a look at the Pourbaix diagram in Figure 2.2, it can be seen that the most stable form of iridium in contact with water is ${IrO_4}^{2-}$ in alkaline conditions and high potentials, which implies that the degradation of iridium oxide would be higher in alkaline compared to acidic conditions. It should be noted that Naito *et al.* [23] has also reported other degradation products different from Ir^{3+} and ${IrO_4}^{2-}$. Depending on the nature of the oxide, there can be several mechanisms of OER and dissolution present at the same time, especially in porous electrodes since there might be a large variation in reaction

rates and local conditions promoting different mechanism [52].

The OER and dissolution reaction is thought to be coupled or intertwined and go through a common intermediate[1, 25, 29, 83]. As a consequence of the duality regarding stability and activity towards OER, Danilovic *et al.* [82] stated that an OER catalyst should balance the two in such a way that the catalyst does not dissolve too fast, nor too slow. However, the findings by Mayrhofer *et al.*[1] suggests that there is no link between the dissolution and activity, but that dissolution and OER are two parallel pathways joined by a common intermediate. They even hypothesise that you might be able to suppress one of them without changing the other considerably. This idea of the two reactions being in parallel is illustrated in Figure 3.1, illustrating that IrO_3 is the common intermediate for this OER path on iridium oxide [25]. Depending on the mechanism of OER and the dissolution of iridium oxide, the common intermediate might be different, and hence affect the dissolution rate. As mentioned, IrO_3 is the common intermediate for the assumed reaction mechanism of OER on thermally treated oxide, while for the electrochemically formed oxide, $HIrO_2$ is the common intermediate and is formed in the same step as oxygen gas[25]. The nature of the intermediate and also whether or not the dissolution step itself is chemical or electrochemical has a great effect on the stability of the OER/dissolution relationship[29]

2.4 Concentrated solution theory

Mass transport in a concentrated electrolytic solution is described by the movement of charged species in the solvent, the interaction between the charged species, mass continuity, current flow, and fluid mechanics [52, p. 271]. The molar flux equation in infinite dilute solution theory[ii] breaks down in concentrated solutions due to the interactions between ionic species being neglected and because the migration and diffusion, and flux relations from this, must be defined with respect to an average velocity of the fluid. There is not only the solvent velocity which contributes to the fluid velocity in a concentrated solution [52, p.274]. Furthermore, the driving force for diffusion is approximated to be concentration gradients instead of gradients in activity, and defining potential gradients in a solution which can change composition should be done with care. This leads to the conclusion that the coupled driving force for both diffusion and migration is expressed with

a gradient in the electrochemical potential, $\tilde{\mu}$, defined as

$$\tilde{\mu_{\mathrm{k}}} = \mu_{\mathrm{k}} + z_{\mathrm{k}}\mathrm{F}\Phi_\beta = \overset{\circ}{\mu_{\mathrm{k}}} + \mathrm{R}T\ln\{a_{\mathrm{k}}\} + z_{\mathrm{k}}\mathrm{F}\Phi_\beta$$

where μ_{k}, $\overset{\circ}{\mu_{\mathrm{k}}}$, a_{k}, and z_{k} are the chemical potential, standard chemical potential, activity, and the charge number for species k respectively. R is the Molar gas constant, F is Faraday's constant[43, p. 4],and T is the temperature. Lastly Φ_β is the potential in phase β. From Newman and Thomas-Alyea [p. 297][52] a multicomponent diffusion equation can be expressed for the total flux density of species k, $\vec{N}_{\mathrm{k}}$, as

$$\vec{N}_{\mathrm{k}} = \frac{c_{\mathrm{t}}c_{\mathrm{k}}\vec{\nabla}\tilde{\mu_k}}{\mathrm{R}T\sum_{l=0}^{k}\frac{c_{\mathrm{l}}(\vec{v}_{\mathrm{l}}-\vec{v}_{\mathrm{k}})}{\mathfrak{D}_{\mathrm{kl}}\vec{v_{\mathrm{k}}}}} = c_{\mathrm{k}}\vec{v}_{\mathrm{k}}$$

where c_{k}, $\vec{\nabla}\tilde{\mu_{\mathrm{k}}}$, and $\vec{v}_{\mathrm{k}}$ is the concentration, gradient in electrochemical potential, and velocity of species k. l is denoting all species which can also contain k. For the system described by SINTEF in their model [3], a KOH electrolyte is used making the only species worth taking into account is $\mathrm{k} = \{\mathrm{H_2O}(l), \mathrm{K^+(aq)}, \mathrm{OH^-(aq)}\}$. $\mathrm{l} = 0$ is reserved for the solute which is $\mathrm{H_2O(l)}$. Finally, $\mathfrak{D}_{\mathrm{kl}}$, is a diffusion coefficient describing the interactions between species k and l, $\mathfrak{D}_{\mathrm{k0}}$ resembles the diffusion coefficient for species k in dilute solution theory. c_{t} is the total concentration including the solute and can be described as [52, p. 298]

$$c_{\mathrm{t}} = \sum_{l=0}^{k} c_{\mathrm{l}}$$

A current in the electrolyte is established due to the movement of the electrically charged species in the electrolyte[52, p. 272]. This current is related to the total molar flux of each charged species in the electrolyte as

[ii] From infinite dilute solution theory, the molar flux density of an ionic species $\vec{N}_{\mathrm{k}}$ is given by

$$\vec{N}_{\mathrm{k}} = \vec{N}_{\mathrm{k}}^{diff} + \vec{N}_{\mathrm{k}}^{Mig} + \vec{N}_{\mathrm{k}}^{Conv} = -D_{\mathrm{k}}\vec{\nabla}c_{\mathrm{k}} - u_{\mathrm{k}}c_{\mathrm{k}}\vec{\nabla}\Phi + c_{\mathrm{k}}\vec{v}$$

where $\vec{N}_{\mathrm{k}}^{diff}$, $\vec{N}_{\mathrm{k}}^{Mig}$, and $\vec{N}_{\mathrm{k}}^{Conv}$ is the diffusion, migration, and the convective molar flux densities of species k respectively [52, p. 271]. The diffusion flux is described by Fick's first law[53, p. 154] where D_{k} is the diffusion coefficient for species k in the solvent and $\vec{\nabla}c_{\mathrm{k}}$ is the concentration gradient and the driving force for diffusion. The migratory flux is the product of the mobility, u_{k}, and concentration, c_{k}, of species k, and the driving force which is the gradient in potential, $\vec{\nabla}\Phi$. Lastly, the convective flux is the product of the fluid velocity, $\vec{v}$, and the concentration of species k.

$$\vec{i}_{\mathrm{L}} = \mathrm{F} \sum_{l=0}^{k} z_{\mathrm{l}} \vec{N}_{\mathrm{l,\ L}}$$

where $\vec{i}_{\mathrm{L}}$ is the current density in the electrolyte phase, denoted L, formed as a response to the molar flux density of electrically charged species movement [52, p. 272][53, p. 165]. Next, a material balance for a component in the electrolyte is needed. For a species k, a mass continuity can be described by

$$\frac{\partial c_{\mathrm{k}}}{\partial t} = -\vec{\nabla} \cdot \vec{N}_{\mathrm{k}} + R_{\mathrm{k}}$$

where $\frac{\partial c_{\mathrm{k}}}{\partial t}$, $\vec{\nabla} \cdot \vec{N}_{\mathrm{k}}$, and R_{k} is the rate of change in concentration for species k, the divergence of the molar flux density of species k, and the production term for species k respectively [p. 272][52]. Lastly, it is reasonable to assume that the liquid electrolyte is macroscopically neutral and that electroneutrality applies [52, p. 273]. Electroneutrality is described as

$$\sum_{j} z_{\mathrm{k}} c_{\mathrm{k}} = 0$$

The fluid velocity, $\vec{v}_{\mathrm{k}}$ has not been described yet, and that is because it is dependent on the nature of the medium the fluid is travelling through. For the case of the AEM-WE, the catalytic layer is porous, and therefore Darcy's law [84] is used to describe the fluid velocity. This is also the case for the model framework by SINTEF [3] and will be elaborated in Section 2.5 where the essential parts of the continuum model will be described shortly.

2.5 Modelling framework

The continuum model developed by SINTEF [3] is a modelling framework meant to simulate the operation of an AEM-WE. The model simulates the entirety of an AEM-WE while the scope of this project is confined to the anode CL, hence only the most essential parts of the model which affect the scope are described here. Figure 1.1 is a representative visualisation of the different domains in the model. From the figure, it can be seen that the anode compartment contains anode catalyst, bipolar plates, porous transport layer, H_2O, O_2, K^+, and OH^-. What is

not present in Figure 1.1 is the ionomer phase, which is added in Figure 1.2. These different phases have different properties, and these properties affect the different mechanisms such as transport, reaction rates, current, etc. A short description of the relevant phases and their properties will be described before elaborating on how they affect the modelling. The notation in this section is inspired by the description of the model by Michael *et al.*[3].

There are primarily three phases in the anode compartment that are of concern, the anode catalytic layer, the ionomer, denoted as "Inmr", and the electrolyte, denoted as "L". As mentioned in Section 1.1, the electrodes are porous, which brings with it complications regarding the ohmic potential drops and the mass transport which now occurs in both series and parallel with electrode processes because of the intimate contact with the electrolyte [52, p. 518]. At any given time, there might be a range of reaction rates as a result of local conditions within the pores. This makes it necessary to describe the porous electrodes with average quantities that are experimentally accessible and expresses the most essential features of the electrode, such as void fraction for porous structures, average surface area per volume, and volume averages of currents and resistivity [52, p. 518]. The addition of the ionomer phase complicates things even further. Now, the ionomer adds an additional way of transport for reactants to the electrode surface on top of the one provided by the pore-filling electrolyte. Furthermore, there will also be an exchange of hydroxide ions and water between the electrolyte and ionomer as well. It is also important to remember that the current must be a part of a continuous circuit, and one of the aspects that characterize an AEM-WE is that the AEM only permits the hydroxide ions to travel between the cathode and anode compartments, which affects both how and the magnitude of the current carried by hydroxide ions. At the boundaries of the anode CL is the AEM and the PTL, which affect the boundary conditions for current and flux.

2.5.1 Governing equations

The Continuum model solves seven governing equations concurrently, with the *ode15i* solver in MATLAB under isothermal conditions and in one dimension. The seven governing equations describe the conservation of gaseous species, conservation of liquid water, conservation of dissolved ionic species, charge conservation, conservation of water in the ionomer phase, conservation of iridium oxide catalyst

volume fraction, and a liquid equation of state which deals with the change in molar volume for water with different ions and concentrations [3]. It is primarily the conservation of iridium catalyst volume fraction that is of most interest, however, the electrochemical reactions are also dependent on the transport of reactants and products and the interplay between the ionomer, electrolyte, CL, AEM, and the PTL, thus this will also be elaborated.

The conservation of gaseous species, k is described by

$$\frac{d\rho_{\mathrm{k}}\epsilon_{\mathrm{G}}}{dt} = -\vec{\nabla} \cdot \vec{J}_{\mathrm{k,\ G}} + S_{\mathrm{k,\ G}} \tag{2.7}$$

where the subscript G denotes gas phase. ρ_{k} is the density of species k and ϵ_{G} is the volume fraction related to the gas phase. The divergence of the mass flux of gas is $\vec{\nabla} \cdot J_{\mathrm{k,\ G}}$ and lastly the source term for the gaseous species is $S_{\mathrm{k,\ G}}$. The mass flux is affected by the porosity of the electrode and will be described later, and the source term for the gaseous species consists of electrochemical reactions, which for the anode is the OER.

Conservation of dissolved species in the liquid phase is expressed with

$$\frac{d(c_{\mathrm{k,L}}\epsilon_{\mathrm{L}})}{dt} = -\vec{\nabla} \cdot \vec{N}_{\mathrm{k,L}} + S_{\mathrm{k,\ L}} \tag{2.8}$$

where $c_{\mathrm{k,\ L}}$ is the concentration of species k in the liquid phase L. Like for Equation 2.7, ϵ_{L} is the volume fraction related to the liquid phase. Lastly, $\vec{\nabla} \cdot \vec{N}_{\mathrm{k,L}}$ and $S_{\mathrm{k,\ L}}$ is the divergence of the molar flux and the source term of species k in the electrolyte phase. This source term is also affected by the electrochemical reactions, but also the exchange of hydroxide and water between the electrolyte and the ionomer, illustrated in Figure 3.2, and will also be elaborated later.

Lastly, the conservation of anode catalyst volume fraction, $\epsilon_{\mathrm{IrO_2}}$, is described by

$$\frac{d\epsilon_{\mathrm{IrO_2}}}{dt} = S_{\mathrm{IrO_2}} \tag{2.9}$$

where $S_{\mathrm{IrO_2}}$ is an expression for the source term for iridium oxide. The source term, $S_{\mathrm{IrO_2}}$ is expressing the dissolution of the catalyst over time, normalised

to the molar volume of iridium oxide, $\bar{V}_{\mathrm{IrO_2}}$, and is described by Butler-Volmer kinetics in the model framework.

How the governing equations are expressed in detail and how they are affected by the porous structure of the electrode and the electrochemical reactions will be elaborated. First a short description of the molar and mass fluxes, then the electrochemical reactions and the dissolution of the electrode catalyst.

2.5.2 Transport equations

Both Equation 2.7 and 2.8 are dependent on mass and molar flux, both of which is affected by the porous structure of the electrode, and thus assumed to follow Darcian flow [84] through the porous membrane. The mass flux of the gaseous species is described solely by convection through porous media and calculated independently as

$$\vec{J}_{\mathrm{k,\ G}} = \rho_{\mathrm{k,\ G}}\vec{v}_{\mathrm{G}} = -\rho_{\mathrm{k,\ G}}\frac{B_{\mathrm{G}}}{\eta_{\mathrm{G}}}\vec{\nabla}p_{\mathrm{G}} \tag{2.10}$$

where $\vec{v}_{\mathrm{G}}$ is the velocity of the gas phase, B_{G} is the permeability of the solid to the gas phase, η_{G} is the viscosity of the gas phase, and lastly $\vec{\nabla}p_{\mathrm{G}}$ is the pressure gradient in the gas phase, which acts as the driving force for convection of the gas. The permeability of the solid to the gas phase is calculated from the saturated permeability, B_{Sat} as

$$B_{\mathrm{G}} = B_{\mathrm{Sat}}\epsilon_{\mathrm{G}}^{1.5} \tag{2.11}$$

The molar flux of ionic species in the electrolyte is described by the concentrated solution theory, but approximating it to moderately dilute solutions [52, p. 289], to the extent that the driving force for diffusion and migration is still coupled and described by a gradient in electrochemical potential, see Section 2.4. This gives

$$\vec{N}_{\mathrm{k,\ L}} = -D_{\mathrm{Eff,\ k}}\vec{\nabla}c_{\mathrm{k}} + \frac{t_{\mathrm{k}}}{z_{\mathrm{k}}\mathrm{F}}\vec{i}_{\mathrm{L}} + c_{\mathrm{k}}\vec{v}_{\mathrm{L}} \tag{2.12}$$

where t_{k} is the transport number of species k, j_{L} is the ionic current in the liquid phase as a result of the movement of ions, $\vec{\nabla}c_{\mathrm{k}}$ is the gradient in the concentra-

tion of species k. Because of the porosity of the electrode, the effective diffusion coefficient, $D_{\text{Eff, k}}$ has replaced the regular diffusion coefficient in Fick's first law [53, p. 154]. Similar to the permeability in Equation 2.11, the effective diffusion coefficient is described by

$$D_{\text{Eff, k}} = D_{\text{k}} \epsilon_{\text{L}}^{\tau} \tag{2.13}$$

where τ is the tortuosity, which is a correction factor for transport through porous media [85]. Tortuosity can be interpreted as a ratio between the actual path through porous media compared to the path in the absence of porosity and is often in the range of $\tau = 1.5$.

2.5.3 Source terms

All three governing equations given earlier is dependent on a source term S of some kind. The source term is a collection of different contributions to increase/decrease the number of species k either through electrochemical reactions or through transfer between phases.

The OER and the dissolution of catalytic particles is the only electrochemical reaction occurring on the anode electrode surface. From reaction 1.5 one can see that the products are oxygen gas and liquid water, and the reactants are four hydroxide ions. This implies that the OER on the surface of the anode affects both the conservation of O_2 and OH^-. It is assumed that the water produced by the OER is in liquid, which leads to oxygen being the only gas produced through the OER. Likewise, hydroxide ions are used in the OER to produce oxygen, but because of the addition of the ionomer, we also have an exchange between the ionomer and the electrolyte phase as well. In the modelling framework[3], the OER is modelled by Butler-Volmer kinetics as

$$\begin{aligned} i_{\text{OER, L}}^{rx} =& (1 - X_{\text{Inmr}}) a i_{\text{n, OER}} \times \\ & \left[\exp\left\{ \frac{\alpha_{\text{OER,a}} n\text{F}}{\text{R}T} \eta_{\text{L}}^{surf} \right\} - \exp\left\{ -\frac{(1 - \alpha_{\text{OER,c}}) n\text{F}}{\text{R}T} \eta_{\text{L}}^{surf} \right\} \right] \end{aligned} \tag{2.14}$$

$$i^{rx}_{\text{OER, Inmr}} = (X_{\text{Inmr}}) a i_{\text{n, OER}} \times \left[\exp\left\{ \frac{\alpha_{\text{OER,a}} n\text{F}}{\text{R}T} \eta^{surf}_{\text{Inmr}} \right\} - \exp\left\{ -\frac{(1-\alpha_{\text{OER,c}}) n\text{F}}{\text{R}T} \eta^{surf}_{\text{Inmr}} \right\} \right] \tag{2.15}$$

where the i^{rx} is a measure of the reaction rate in the form of a volume averaged current density. a is the specific interfacial area describing the surface area in the porous electrode per volume, i_{n} is the exchange current density for the OER on iridium oxide, α_a and α_c is the charge transfer coefficients for the anode and cathode reactions of the OER respectively, η^{surf} is the surface overpotential, and lastly X_{Inmr} is the fraction of the surface area covered by the ionomer, making the rest, $(1 - X_{\text{Inmr}})$ covered by electrolyte.

The source terms for oxygen in the gas phase then becomes the sum of the contributions of the OER in ionomer and electrolyte as

$$S_{\text{O}_2\text{, G}} = \frac{i^{rx}_{\text{OER, L}} + i^{rx}_{\text{OER, Inmr}}}{n\text{F}} \text{M}_{\text{O}_2} \tag{2.16}$$

where M_{O_2} is the molar mass of oxygen gas. For the hydroxide ions which are consumed in the OER, the source term for the hydroxide in both the electrolyte and the ionomer phase becomes a sum of the contributions from the OER and the exchange between the ionomer and the electrolyte as

$$S_{\text{OH}^-\text{L}} = \frac{i^{rx}_{\text{OER, L}}}{n\text{F}} \text{M}_{\text{OH}^-} - R_{\text{Exch}} \tag{2.17}$$

$$S_{\text{OH}^-\text{Inmr}} = \frac{i^{rx}_{\text{OER, Inmr}}}{n\text{F}} \text{M}_{\text{OH}^-} - R_{\text{Exch}} \tag{2.18}$$

where M_{OH^-} is the molar ass of the hydroxide ion, and R_{Exch} is the exchange term expressing the exchange of hydroxide between the ionomer and the electrolyte phase. The exchange of hydroxide and water between the ionomer and the electrolyte is illustrated in Figure 3.2.

Finally, source term for the conservation of the catalyst layer expressed in Equation 2.9 is assumed to only be a function electrochemical kinetics and assumed to follow Butler-Volmer kinetics as well. The dissolution of the IrO_2 is given by

$$i^{rx}_{\text{Diss}} = a i_{\text{n, Diss}} \left[\exp\left\{ \frac{\alpha_{\text{Diss, aF}}}{\text{R}T} \eta_{\text{Diss}} \right\} - \exp\left\{ -\frac{\alpha_{\text{Diss, cF}}}{\text{R}T} \eta_{\text{Diss}} \right\} \right] \tag{2.19}$$

and like the source terms for oxygen and hydroxide, the source term for IrO_2 then becomes linear function of the dissolution current by

$$S_{\text{IrO}_2} = -\frac{i^{rx}_{\text{Diss}} \bar{V}_{\text{IrO}_2}}{n\text{F}} \tag{2.20}$$

where $\bar{V}_{\text{IrO}_2}$ is the molar volume of IrO_2.

The specific interfacial area of the catalyst layer available for reaction, a, is assumed to consist of a number of particles, or clusters, N_{p}, per volume. These clusters are also assumed to be spheres, with a radius, r, which has its original value from geometrical considerations expressed as

$$r(t) = \frac{3\epsilon_{\text{IrO}_2}}{a} \tag{2.21}$$

By setting the initial value of $a = 2{\cdot}10^6$ m^2 m^{-3} and the initial value of the volume fraction of iridium oxide to be $\epsilon_{\text{IrO}_2} = 0.14$, an initial radius to the clusters are defined. Since this radius can describe the surface area of every particle on the surface, that also means that the total interfacial area can be expressed as the total surface area for all the clusters on the surface as

$$a = 4\pi r(t)^2 N_{\text{p}} \tag{2.22}$$

This radius, r, can also describe the volume of the clusters, V_{p} through the volume of a sphere as

$$V_{\text{p}} = \frac{4\pi r(t)^3}{3} \tag{2.23}$$

During the dissolution, it is assumed that iridium atoms are removed from these particles/clusters that contain the catalyst material. This implies that the number of particles per volume, N_{p}, stays the same, but the radius of every cluster does not. For every time step, ϵ_{IrO_2} is calculated from Equation 2.9, which results in

a new volume of each particle. The new V_{p} can be described through geometrical considerations from the new volume fraction and the number of particles per volume as

$$V_{\mathrm{p}} = \frac{\epsilon_{\mathrm{IrO_2}}}{N_{\mathrm{p}}}$$

This will in turn provide a new radius by Equation 2.23 which can be used to calculate a new value for the interfacial area through Equation 2.22. However, this approach also implies that the dissolution occurs uniformly over every particle, but the particles might experience different dissolution rates between them selves.

2.6 Microkinetic modelling

Microkinetic modelling is a powerful tool for studying and describing the surface kinetics of heterogeneous catalysis, be it electrocatalysis or not [86]. Microkinetic modelling has been widely used to study the kinetics of different types of reactions on surfaces and compare model predictions with experimental data, and in that way extracting important parameters such as rate constants, the free energy of adsorptions for intermediates, and rate-determining steps for different catalysts [86, 87]. One of the most important aspects of microkinetic modelling and analysis is the use of physical and chemical parameters that can be either estimated and related by theory and/or measured experimentally [88, p. 3]. The main objective of the microkinetic analysis is to unify available experimental data, theoretical principles, and fitting correlations relevant to the catalyst reactions in a quantitative manner [88, p. 2].

The fundamental starting point for a microkinetic analysis is the description of a reaction by a feasible reaction mechanism consisting of several elementary steps encapsulating the essentials of the surface reactions [88, p. 2]. This includes reactants, products, intermediates and their surface coverages, and the interplay between them. A fundamental assumption for microkinetic modelling is therefore to assume that the reaction itself can indeed be described by a set of stepwise elementary reactions. An elementary step is regarded as the most simple, mechanistic process a reaction can undergo [52, p. 207]. A reaction scheme or mechanism dictates the output of the model and thus plays an essential role in the output

of the microkinetic model to be successful [29, 36]. Consequently, the mechanism should be inspired by either experimentally found intermediates or measured data.

The microkinetic analysis describes a reaction as a set of elementary reactions, and the rate of each elementary reaction has its own rate [88, p. 2]. Usually, the *power-law model* is used to describe the kinetics of elementary reactions[86]. This model is extensively used because of its ease of application, but it might be a limiting approximation to more complicated mechanisms[86]. The power law model, as described by Fogler [89, p. 82], describes the rate of reaction as a product of the activity for the reacting species raised to the power of their reaction order and a rate constant. Equation 2.24

$$r_{\mathrm{j}} = k_{\mathrm{j}} \prod_{k} a_{\mathrm{k}}^{\Omega_{\mathrm{k}}} \tag{2.24}$$

illustrates the power-law model for an elementary step j of a mechanism with rate constant, k_{j}, and the activity of species k, a_{k}, reacting in the step raised to its respective reaction order Ω_{k}[88, p. 24][89, p. 82][86]. Note that for a reversible reaction, equation 2.24 can express both the backward and the forward rate, and the total rate is the difference between the two. The rate constant, k_{j}, is not dependent on the reacting species but is a function of temperature[88, p. 23]. In this project, the rate constant, k_{j}, is denoted as a chemical rate constant as k_{j}^{0}, to separate it from the potential dependent rate constants $k_{\mathrm{j}}(E)$. The reaction orders for a species, Ω_{k} are often assumed to correlate with the stoichiometric coefficients, but must always be measured and verified experimentally if the power law is assumed [89]. In order to describe elementary steps which are also electrochemical, the elementary step is assumed to follow Butler-Volmer kinetics and in its most simple way should also only include the transfer of one single electron [p. 130][53]. The activity of the electron is dependent on the potential that the electrode experiences through [53, p. 135]

$$a_{\mathrm{e}^-} = \exp\left\{-\frac{\mathrm{F}}{\mathrm{R}T}(E - E_{\mathrm{n}})\right\} \tag{2.25}$$

3 Method

In order to study the degradation of IrO_2 used as the anode catalyst material in an AEM-WE under OER conditions studied in this thesis, microkinetic modelling was applied to the reaction mechanism describing the coupled mechanism of degradation of IrO_2 during OER and the OER on an IrO_2 surface proposed by Kasian *et al.* [25] with some modifications. The full reaction mechanism including dissolution by Kasian *et al.*[25, 63] is provided in Appendix B. By applying microkinetic analysis to the proposed mechanism, it is implicitly assumed that the reaction indeed can be described by a set of elementary steps [86]. Though Kasian *et al.* [25] proposed the mechanism in acidic conditions, the same mechanism is assumed to be applicable to alkaline conditions as well, by assuming water autoprotolysis to hold[i][32] such that acidic conditions can be transformed to alkaline conditions. Hence, the degradation of IrO_2 was studied during OER in both acidic and alkaline environments. In addition, using the modelling framework by SINTEF described in Section 2.5, the effect and the rate of catalyst degradation could be studied during the operation of an AEM-WE by the use of the continuum model.

The proposed reaction mechanism is a two-way mechanism, which includes both oxygen evolution, and dissolution through the formation of IrO_4^{2-} and is assumed to be the most dominant mechanism present on thermally formed iridium oxide [25]. If electrochemically grown iridium oxide was assumed, then the other half of the mechanism proposed by Kasian *et al.*.[25] would be most fitting. Figure 3.1 is a simplification of the reaction scheme presented later in this section which displays the different species containing iridium throughout the propagation of the reaction. The starting point is the iridium oxide IrO_2, which then reacts in step 1 in the figure and creates IrO_2OH. IrO_2OH reacts further into IrO_3 in step 2. Now IrO_3 acts as a common intermediate[25] for the two pathways, where the reaction can either go towards dissolution by IrO_4^{2-} in step 3, or towards the formation of oxygen and IrO_2 as displayed in step 4. If the reaction goes through the latter step, IrO_2 can again be used as a catalyst for the reaction by providing an active site on the surface, shown by the arrow pointing towards the top.

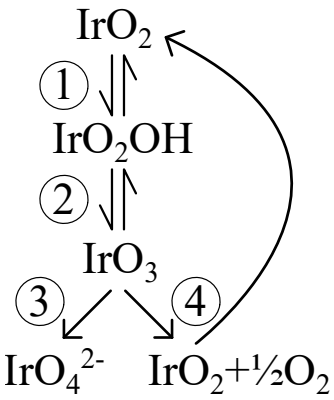

Figure 3.1: The reaction pathway for the OER (1-2-4) on IrO_2 and degradation of IrO_2 (1-2-3) during OER. If the reaction goes towards OER, then IrO_2 is not consumed during the reaction and can act as an electrocatalyst again. The numerical steps are also analogous to the reaction mechanisms described in the acidic model, and steps in the alkaline model.

The reaction mechanism provided in Figure 3.1 is applicable in both acidic and alkaline environments, and will be referenced later. First, the acidic model will be described, and then the alkaline model.

3.1 Acidic model

By assuming the starting point for the mechanism is already formed IrO_2, meaning omitting step B.1 (and hence B.3) and B.2 and combining B.4, and B.5 to step 3.1, the dissolution mechanism on the IrO_2 surface becomes

$$IrO_2(s) + H_2O(l) \underset{k_{1-}}{\overset{k_{1+}}{\rightleftharpoons}} IrO_2OH + H^+(aq) + e^- \tag{3.1}$$

$$IrO_2OH \underset{k_{2-}}{\overset{k_{2+}}{\rightleftharpoons}} IrO_3 + H^+(aq) + e^- \tag{3.2}$$

$$IrO_3 + H_2O(l) \underset{k_{3-}}{\overset{k_{3+}}{\rightleftharpoons}} IrO_4^{2-}(aq) + 2\,H^+(aq) \tag{3.3}$$

$$IrO_3 \underset{k_{4-}}{\overset{k_{4+}}{\rightleftharpoons}} IrO_2(s) + \frac{1}{2}O_2(aq) \tag{3.4}$$

where step 3.1 and 3.2 are electrochemical reaction steps indicated by the presence of electrons, e^-, and step 3.3 and 3.4 are purely chemical. The reaction steps provided in this mechanism in an acidic environment are analogous to the simplified mechanism provided in Figure 3.1. In this mechanism, IrO_2 represents an active site on the surface of the iridium oxide layer, and IrO_2OH and IrO_3 denote surface

intermediates by adsorbed OH and O respectively. Based on this mechanism, it is assumed that IrO_2OH and IrO_3 are the only surface species present, and hence, all occupied active sites are occupied by one of these two. If the dissolution step, step 3.3, is neglected, then the reaction mechanism becomes that of the Electrochemical oxide path proposed by Bockris *et al.* [59], see Section 2.2.

If the reaction proceeds through step 3.1 - 3.2 - 3.3, indicated by step 1 - 2 - 3, in Figure 3.1, then the reaction goes towards dissolving the catalytic surface via the soluble species IrO_4^{2-}. The total reaction for this process is the sum of these steps and yields,

$$\begin{gathered} IrO_2(s) + 2\,H_2O(l) \rightleftharpoons IrO_4^{2-}(aq) + 4\,H^+(aq) + 2\,e^- \\ E^{\circ}_{\text{diss}} = 2.057\,\text{V vs SHE} \end{gathered} \tag{3.5}$$

with its standard reduction potential $E^{\circ}_{diss} = 2.057\,\text{V vs SHE}$[90]. It shows that the degradation of the catalytic surface, IrO_2, is dependent on both the pH and the potential.

If the reaction mechanism were to proceed through oxygen formation by step 3.1 - 3.2 - 3.4, then IrO_2 would act as an electrocatalyst towards OER. The half-reaction for this process is

$$\begin{gathered} IrO_2(s) + H_2O(l) \rightleftharpoons IrO_2(s) + \frac{1}{2}O_2(aq) + 2\,H^+(aq) + 2\,e^- \\ E^{\circ}_{\text{OER}} = 1.23\,\text{V vs SHE} \end{gathered} \tag{3.6}$$

with its well known standard reduction potential of $E^{\circ}_{\text{OER}} = 1.23\,\text{V vs SHE}$[43]. This way is again analogous to Figure 3.1 by steps 1 - 2 - 4. Here IrO_2 is solely acting as an electrocatalyst towards the OER [44, p. 339-241]. The two standard potentials for the two half-reactions 3.5 and 3.6 is given in Table 3.1

Table 3.1: The standard electrode potentials for the dissolution reaction, $E^{\circ}_{\mathrm{Diss}}$, and for the oxygen evolution reaction (OER), E°_{OER} in acidic environment

Parameter	Unit	Value
$E^{\circ}_{\mathrm{Diss}}$	V vs SHE	2.057 [90]
E°_{OER}	V vs SHE	1.23 [43, p. 157]

In order to study this reaction mechanism by microkinetic modelling, the rate of each step must be described by a rate law, where the power law model is assumed to be applicable. By applying the power law model to each step in the degradation mechanism under acidic conditions described by the steps 3.1 to 3.4, the rate of each step can be expressed by

$$r_1 = r_{1+} - r_{1-} = k_{1+}\Gamma(1-\theta_1-\theta_2)a_{\mathrm{H_2O}} - k_{1-}\Gamma\theta_1 a_{\mathrm{H^+}} \tag{3.7}$$

$$r_2 = r_{2+} - r_{2-} = k_{2+}\Gamma\theta_1 - k_{2-}\Gamma\theta_2 a_{\mathrm{H^+}} \tag{3.8}$$

$$r_3 = r_{3+} - r_{3-} = k^0_{3+}\Gamma\theta_2 a_{\mathrm{H_2O}} - k^0_{3-} a_{\mathrm{IrO_4^{2-}}} a^2_{\mathrm{H^+}} \tag{3.9}$$

$$r_4 = r_{4+} - r_{4-} = k^0_{4+}\Gamma\theta_2 - k^0_{4-}\Gamma(1-\theta_1-\theta_2)\sqrt{a_{\mathrm{O_2}}} \tag{3.10}$$

where the total rate of each step, r_{j}, is given by the difference between the forward reaction, $r_{\mathrm{j}+}$, and backward reaction, $r_{\mathrm{j}-}$, for step $\mathrm{j} = \{1,2,3,4\}$. Γ represents the total concentration of active sites on the IrO_2-surface and is an intrinsic property of the nature of the oxide layer and is different whether the layer is hydrous, anhydrous, polycrystalline, monocrystalline etc... Each step is a product between the rate constant, $k_{\mathrm{j}\pm}$ or $k^0_{\mathrm{j}\pm}$, for step j and the activities of the reacting species, a_{k}, raised to their stoichiometric coefficient ν_{k}, where $\mathrm{k} = \{\mathrm{IrO_2}, \mathrm{IrO_2OH}, \mathrm{IrO_3}, \mathrm{H^+}, \mathrm{H_2O}, \mathrm{O_2}\}$. The activities of reacting species k is a function of the surface concentration[iii], c_{k} since electrochemical reactions occur on electrode surfaces. Subsequently, the activities of IrO_2OH and IrO_3 are described with their surface concentration expressed by their fractional surface coverage, θ, with respect to the total concentration of active sites, Γ. Therefore, their fractional coverage is denoted θ_1 and θ_2 respectively, and their activities then become $\Gamma\theta_1$ and $\Gamma\theta_2$ respectively[91]. The use of fractional coverages implies that the activity of the catalyst surface, $a_{\mathrm{IrO_2}}$, can be expressed as $\Gamma(1-\theta_1-\theta_2)$, practically represent

an unoccupied site. Lastly, the rate constants for step j is represented by either $k_{\mathrm{j}\pm}$ or $k^0_{\mathrm{j}\pm}$. $k^0_{\mathrm{j}\pm}$ denotes the chemical rate constants for step j, and $k_{\mathrm{j}\pm}$ denotes the potential dependant rate constants for the electrochemical steps. $k_{\mathrm{j}\pm}$ also encapsulates the activity of the electrons through Equation 2.25 and is expressed by

$$k_{\mathrm{j}+} = k^0_{\mathrm{j}+} \exp\left\{\frac{(1-\alpha_{\mathrm{j}})\mathrm{F}}{\mathrm{R}T}(E - E_{\mathrm{n}})\right\} \quad j = 1, 2 \tag{3.11}$$

$$k_{\mathrm{j}-} = k^0_{\mathrm{j}-} \exp\left\{\frac{-\alpha_{\mathrm{j}}\mathrm{F}}{\mathrm{R}T}(E - E_{\mathrm{n}})\right\} \quad j = 1, 2 \tag{3.12}$$

and is also a function of the chemical rate constants $k^0_{\mathrm{j}\pm}$. Both the chemical rate constant and the electrochemical rate constant are a function of temperature, T, but the potential dependent rate constant is also a function of the transfer coefficient α_{j}[53, p. 135], Faradays number, F, the molar gas constant, R, the electrode potential, E, and the null potential, E_{n} for the reaction. The null potential, E_{n}, for a reaction is expressed by Nernst equation as

$$E_{\mathrm{n}} = E^{\ominus}_{\mathrm{j}} - \frac{\mathrm{R}T}{\mathrm{nF}} \ln\left\{\prod_k a_{\mathrm{k}}^{\nu_{\mathrm{k}}}\right\} \tag{3.13}$$

where ν_{k} is the stoichiometric coefficient for species k = $\{\mathrm{IrO_2(s)}, \mathrm{H_2O(l)}, \mathrm{H^+(aq)}, \mathrm{IrO_4^{2-}(aq)}, \mathrm{O_2(aq)}\}$ which participates in reaction j. By using the convention that the half-reactions are written as reductions, then ν_{k} adopts a positive sign if species k is a product and a negative if it is a reactant. $E^{\ominus}_{\mathrm{j}}$ is the standard potential for the half-reaction [53], and if the activity for all species is set to unity, $a_{\mathrm{k}} = 1 \forall \mathrm{k}$, then the null potential becomes equal to the standard potential, $E_{\mathrm{n}} = E^{\ominus}$. Lastly, the n in the denominator represents the number of electrons being transferred every time the reaction proceeds, in this case, $n = 2$. Since the mechanism has two separate paths, as indicated by figure 3.1, this gives rise to two separate faradaic currents[92], which also means that there is a null potential related to both the pathway that leads to the dissolution reaction, given by reaction 3.5, and the OER,

[iii] The activity of species k is a function of concentration through

$$a_{\mathrm{k}} = \gamma_{\mathrm{k}} \frac{c_{\mathrm{k}}}{c^0}$$

where γ_{k} is the activity coefficient for species k, which expresses deviations from ideality, and c^0 is the reference concentration $c^0 = 1\,\mathrm{mol\,L^{-1}}$. γ_{k} is often difficult to predict but is assumed to be unity in infinitely dilute solutions.

given by reaction 3.6.

3.2 Alkaline model

The same reaction mechanism introduced in the previous section is assumed to also be applicable under alkaline conditions, by assuming the chemical equilibrium of the water autoprotolysis[i] to hold. By doing so, the acidic conditions can be trivially changed to alkaline conditions by the introduction of hydroxide ions [32]. Consequently, the degradation mechanism of IrO_2 in alkaline environment can be expressed by

$$IrO_2(s) + OH^-(aq) \underset{k_{1-}}{\overset{k_{1+}}{\rightleftharpoons}} IrO_2OH + e^- \tag{3.14}$$

$$IrO_2OH + OH^-(aq) \underset{k_{2-}}{\overset{k_{2+}}{\rightleftharpoons}} IrO_3 + H_2O(l) + e^- \tag{3.15}$$

$$IrO_3 + 2\,OH^-(aq) \underset{k^0_{3-}}{\overset{k^0_{3+}}{\rightleftharpoons}} IrO_4^{2-}(aq) + H_2O(l) \tag{3.16}$$

$$IrO_3 \underset{k^0_{4-}}{\overset{k^0_{4+}}{\rightleftharpoons}} IrO_2(s) + \frac{1}{2}O_2(aq) \tag{3.17}$$

where step 3.14 and 3.15 are electrochemical and 3.16 and 3.17 are purely chemical. Comparable to the mechanism described in the previous section, hydroxide ions have been added to all the steps which are dependent on the pH, and that way neutralised H^+ to H_2O. If the dissolution step, step 3.16, is neglected from the mechanism the resulting mechanism is the electrochemical oxide path on IrO_2 proposed by Bockris *et al.* [59], see section 2.2, in alkaline conditions. The same notation as introduced in the acidic model is used here.

If the reaction proceeds through step 1-2-3 as indicated by figure 3.1, represented by step 3.14 - 3.15 - 3.16 in the alkaline model, then the end product is dissolution of the catalytic layer via the soluble species IrO_4^{2-}, same as for the acidic model, though the reaction steps are different. The sum of these steps yields the half-reaction for dissolution given by

$$\begin{gathered}\mathrm{IrO_2(s) + 4\,OH^-(aq) \rightleftharpoons IrO_4^{2-}(aq) + 2\,H_2O(l) + 2\,e^-} \\ E^{\circ}_{\mathrm{Diss}} = 0.401\,\mathrm{V vs\ SHE}\end{gathered} \tag{3.18}$$

with its standard potential of $E^{\circ}_{\mathrm{Diss}} = 0.401\,\mathrm{V vs\ SHE}$ [iv]. In the reaction, the catalyst is consumed and therefore no longer acts as a catalyst towards the OER [44, p. 339-341].

On the other hand, if the reaction proceeds through steps 1-2-4 from figure 3.1, also represented by step 3.14 - 3.15 - 3.17, then the half-reaction becomes that of OER on iridium oxide in alkaline conditions

$$\begin{gathered}\mathrm{IrO_2(s) + 2\,OH^-(aq) \rightleftharpoons IrO_2(s) + \frac{1}{2}O_2(aq) + H_2O(l) + 2\,e^-} \\ E^{\circ}_{\mathrm{OER}} = 0.401\,\mathrm{V vs\ SHE}\end{gathered} \tag{3.19}$$

where IrO_2 is not consumed and can be used again as an active site in the catalytic layer. This is also depicted in figure 2.1. If the mechanism proceeds this way, then IrO_2 does in fact behave as a catalyst towards OER [44, p. 339-241]. The standard potentials for the half-reactions 3.18 and 3.19 is available in Table 3.2

Table 3.2: The standard electrode potentials for the dissolution reaction, $E^{\circ}_{\mathrm{Diss}}$, and for the oxygen evolution reaction (OER), E°_{OER}

Parameter	Unit	Value
$E^{\circ}_{\mathrm{Diss}}$	V vs SHE	0.401 [iv]
E°_{OER}	V vs SHE	0.401 [43, p. 43]

By following the same procedure as described in the acidic model, the power law model is applied to describe the rate of the reaction steps 3.14 to 3.17, and Butler-Volmer kinetics are applied to describe the activity of the electrons described by Equation 2.25 for electrochemical steps. The rate equations for each step in the

[iv] The standard reduction potential for reaction 3.18, $E^{\circ}_{\mathrm{Diss}}$, was found by using equation A.10 which is derived based on reaction 3.5 and reaction A.4. By using the acidic dissolution reaction and applying standard state, meaning setting $p\mathrm{Ir} = 0$ in equation A.10, and using the tabulated standard reduction potential for reaction A.4 provided by Milazzo and Caroli [90] to be $E^{\circ}_{\mathrm{Diss}} = 2.057\,\mathrm{V}$, the standard reduction potential for reaction 3.18 could be found by evaluating equation A.10 at $p\mathrm{H} = 14$.

mechanism under alkaline conditions becomes

$$r_1 = r_{1+} - r_{1-} = k_{1+}\Gamma(1-\theta_1-\theta_2)a_{OH^-} - k_{1-}\Gamma\theta_1 a_{H_2O} \tag{3.20}$$

$$r_2 = r_{2+} - r_{2-} = k_{2+}\Gamma\theta_1 a_{OH^-} - k_{2-}\Gamma\theta_2 a_{H_2O} \tag{3.21}$$

$$r_3 = r_{3+} - r_{3-} = k^0_{3+}\Gamma\theta_2 a^2_{OH^-} - k^0_{3-} a_{IrO_4^{2-}} a_{H_2O} \tag{3.22}$$

$$r_4 = r_{4+} - r_{4-} = k^0_{4+}\Gamma\theta_2 - k^0_{4-}\Gamma(1-\theta_1-\theta_2)\sqrt{a_{O_2}} \tag{3.23}$$

where r_j is the total rate of reaction j which is still the difference between the forward rate, r_{j+}, and the backward rate r_{j-} where $j = \{1,2,3,4\}$. Γ denotes the total concentration of active sites available on the surface of the catalyst. The intermediates IrO_2OH and IrO_3 from the described reaction mechanism are formed on the surface, and therefore occupy an active site each. It is still assumed that these two intermediates are the only two intermediates taking part in the reaction mechanism and consequently an available active site, IrO_2, is then denoted $\Gamma(1-\theta_1-\theta_2)$. The activities for each species taking part in each elementary step is a_k for each species $k = \{H_2O(l), OH^-(aq), IrO_4^{2-}(aq), O_2(aq)\}$. Lastly, the chemical rate constants for each step is denoted k^0_{j+} and k^0_{j-} follows the same notation as described in the acidic model and is expressed by equation 3.11 and 3.12 respectively. The null potential as expressed by the Nernst equation, equation 3.13, in the previous section, still applies, but the reactants and products have changed in response to the shift to alkaline conditions. This means that there is a null potential and anodic current related to reaction 3.18 and 3.19.

3.3 Numerical approach

The numerical approach for studying the degradation of iridium oxide under OER conditions was the same for both the acidic and alkaline models[v]. The end goal was to try and describe qualitatively how fast the degradation occurs in acidic and alkaline environments. For both models, the rate of dissolution is given by the rate of the third step in both mechanisms, meaning step 3.3 and 3.16 in the acidic and alkaline model respectively. This implies that the motivation behind this approach is to compare the rate of dissolution described by 3.3 and 3.16 with measured degradation data. Degradation data measured by Mayrhofer *et al.* [1] is used for the acidic model, and data from Schalenbach *et al.* [2] is used in

the alkaline model. The amount of data on iridium oxide is much more scarce for alkaline conditions than for acidic conditions, so the data provided by Schalenbach *et al.* [2] is for metallic iridium. The simulated current-potential curves can be found by expressing the conservation of adsorbed species and the sweep rate, ν, in the form of a set of differential equations as

$$\frac{d(\Gamma\theta_1)}{dt} = r_1 - r_2 \tag{3.24}$$

$$\frac{d(\Gamma\theta_2)}{dt} = r_2 - r_3 - r_4 \tag{3.25}$$

$$\frac{dE}{dt} = \nu \tag{3.26}$$

and then solving the set of equations where t is the time variable. Equation 3.24 and 3.25 describes the conservation of the site coverage of IrO_2OH and IrO_3 respectively and equation 3.26 describes the sweep rate. Here r_1, r_2, r_3, r_4 represents the reaction rates described in section 3.1 or 3.2 depending on the model used. Then by following the same procedure as Daydova *et al.* [93, 91], the total faradaic current of the system arising from electrochemical reactions on the surface of the electrode can be described as the sum of the electrochemical steps by

$$i = nF(r_1 + r_2) \tag{3.27}$$

in the case where transport limitations are absent[91]. Equation 3.27 relates the electrochemical steps from the reaction scheme to the faradaic current density, i. The current density is the total current, I, divided by the surface area, A, of the electrode available for reactions

$$i = \frac{I}{A}$$

As Figure 3.1 suggests, there are two possible reaction pathways, assuming the given reaction mechanism is the dominant one, which gives rise to one anodic current originating from two different reaction pathways. These reactions are a

[v]The code used to do the microkinetic modelling is available on the public Github repository: `https://github.com/pekarste/Degradation/tree/main`. Some segments are also provided in Appendix F

part of the same mechanism and occur on the same electrode and will experience the same potential. The total current density will therefore be the sum of the two. That is

$$i_{\text{tot}}^{an} = i_{\text{OER}} + i_{\text{Diss}} \tag{3.28}$$

where i_{t}^{an} is the total anodic current density, and i_{OER} and i_{Diss} is the current density from the OER and the dissolution reaction on the anode respectively. From the literature, and based on general catalyst properties, it is reasonable to assume that the OER pathway will dominate over the dissolution pathway, $i_{\text{OER}} \gg i_{\text{Diss}}$. Cherevko *et al.* [27] found that the faradaic current efficiency for the dissolution current on iridium oxide was somewhere between 0.05% and 1% in acidic conditions. Schalenbach *et al.* [2] found a similar current efficiency for the dissolution current in alkaline media to be around 0.01% at $i = 1\,\text{mA}\,\text{cm}^{-2}$. These findings are in line with the assumption that the majority of the anodic current is originating from the OER. This assumption lets Equation 3.28 be approximated to

$$i_{\text{tot}}^{an} \approx i_{\text{OER}} \tag{3.29}$$

which also implies that the reaction mechanism is dominated by the OER pathway following step 3.1/3.14 - 3.2/3.15 - 3.4/3.17. This can be illustrated in Figure 3.1 as the pathway 1-2-4 will dominate over 1-2-3.

The next step is then to find an expression for the total current density. In order to do that, a quasi-steady state is assumed for the mechanism where step 3.2 and 3.15 is assumed to be the rate-determining step (rds) for the acidic and alkaline model respectively. The rate-determining step is now denoted as $\hat{r}_2$, where the hat $\hat{}$ represents rds. The rds is assumed to be much slower than the other steps [53, p. 48], hence this step is the bottleneck for the rate of the reaction. This implies that the steps prior, meaning step 3.1/3.14, can be assumed equilibrated, and the steps after the rds, meaning step 3.4/3.17 can be assumed to be much faster than the forward rate of the rds [35, 36, 37]. Though, it is advisable to avoid such quasi-steady-state assumptions when modelling dynamic behaviour since it can

undermine the complexity of the kinetics and hide kinetic properties like several Tafel slopes across large potential regions [28, 35]. A full dynamic analysis inspired by the work of Reksten [94] and Marshall *et al.* [28] was attempted, but ultimately abandoned and described in Appendix D. Finally, by assuming a quasi-steady-state and following the procedure from the mechanistic study described by Reksten *et al.* [37] to derive an expression for the total rate of the OER based on the rds, the rate of the reaction becomes

$$\text{Acidic model}: \quad \hat{r}_2 = \frac{\Gamma k_{2+}^0 \exp\left\{\frac{(1-\alpha_2)\mathrm{F}}{\mathrm{R}T}(E-E_\mathrm{n})\right\}}{1+\frac{a_{\mathrm{H}^+}}{a_{\mathrm{H_2O}}}K_1^0\exp\left\{-\frac{\mathrm{F}}{\mathrm{R}T}(E-E_\mathrm{n})\right\}} \approx \frac{i_{\mathrm{tot}}^{an}}{n\mathrm{F}} \tag{3.30}$$

$$\text{Alkaline model}: \quad \hat{r}_2 = \frac{\Gamma k_{2+}^0 \exp\left\{\frac{(1-\alpha_2)\mathrm{F}}{\mathrm{R}T}(E-E_\mathrm{n})\right\} a_{\mathrm{OH}^-}}{1+\frac{K_1^0}{a_{\mathrm{OH}^-}}\exp\left\{-\frac{\mathrm{F}}{\mathrm{R}T}(E-E_\mathrm{n})\right\}} \approx \frac{i_{\mathrm{tot}}^{an}}{n\mathrm{F}} \tag{3.31}$$

where k_{2+}^0 is the chemical forward rate constant for step 3.2/3.15, which is also the rds. α_2 is the transfer coefficient [53, p. 135] which accompanies the electron transfer in the rds, though it is assumed that the transfer coefficient for both electrochemical steps is equal, meaning $\alpha_1 = \alpha_2 = \alpha$. Following the notation of Reksten *et al.* [37], K_1^0 is the ratio between the chemical backwards and forward rate constant, $\frac{k_{1-}^0}{k_{1+}^0}$. This expression is based on the assumption that OER dominates over the dissolution reaction, and therefore simulates the OER, consequently, the null potential, E_n, for this expression is that of the OER [vi]. Lastly, the n in this denominator is representing the total number of electrons being transferred in reaction 3.6/3.19, which can be seen as $n = 2$.

Equation 3.30 and 3.31 is supposed to simulate a polarization curve for the OER, and by using reported linear sweep voltammetry data (LSV) for OER on iridium and iridium oxide, the unknown parameters to equation 3.30/3.31 could be found through numerical fitting procedures in MATLAB ®. By using reported LSV

[vi] The OER is given in reaction 3.6 for the acidic model and 3.19 for the alkaline model. By using the Nernst equation given in 3.13, the null potential becomes

$$\text{Acidic model}: \quad E_\mathrm{n} = E_{\mathrm{OER}}^{\circ} - \frac{\mathrm{R}T}{n\mathrm{F}}\ln\left\{\frac{a_{\mathrm{H_2O}}}{a_{\mathrm{H}^+}^2\sqrt{a_{\mathrm{O_2}}}}\right\}$$

$$\text{Alkaline model}: \quad E_\mathrm{n} = E_{\mathrm{OER}}^{\circ} - \frac{\mathrm{R}T}{n\mathrm{F}}\ln\left\{\frac{a_{\mathrm{OH}^-}^2}{a_{\mathrm{H_2O}}\sqrt{a_{\mathrm{O_2}}}}\right\}$$

which depends on the pH/pOH.

data for OER on iridium and iridium oxide from Scohy *et al.* [24] and Mayrhofer *et al.* [1] in the acidic model, and Schalenbach *et al.* [2] for the alkaline model, and lastly, Cherevko *et al.* [50] and Damjanovic *et al.* [95] for both models, estimates for Γk_{2+}^0, $\alpha_2 = \alpha$, and K_1^0, could be found. Γ is treated as an unknown since it is difficult to estimate, and therefore the product Γk_{2+}^0 is found by fitting instead of Γ and k_{2+}^0 separately. The numerical fitting and the resulting fitting parameters are presented in Section 4 for Mayrhofer *et al.*[1] and Schalenbach *et al.*[2] since that is where the degradation comes from. The fitting results from the other LSV data are shown in Appendix C.

With estimate values for the fitting parameters Γk_{2+}^0, $\alpha_2 = \alpha$, and K_1^0, the rate of degradation could be found. In this assessment, the rds is assumed to be much slower than the rest of the steps. This means that one could assume that the rate of formation of IrO_2OH, denoted as $\Gamma\theta_1$, given in equation 3.24 to be at steady state. Now, one can solve the site balance for IrO_3, which is denoted $\Gamma\theta_2$, given as the differential equation 3.25 with respect to time with some assumptions being made. Firstly, the backwards reaction for both step 3.3/3.16 and 3.4/3.17 can be assumed to be much lower than the forward reaction. In this approximation, the redeposition of IrO_4^{2-} is assumed negligible compared to the dissolution of IrO_4^{2-}, making the forward rate of step 3.3/3.16 much larger than the backward rate, $r_{3+} \gg r_{3-}$. Though, it should be noted that Yu *et al.* [96] did a study on PEM-WE degradation and found that iridium was redeposited all across the membrane, and was even found on the cathode, still, the redeposition of iridium was outside of the scope. The same goes for the last step, 3.4/3.17, which creates oxygen in the OER mechanism. The back diffusion of O_2 back to the iridium oxide surface is highly unlikely, and can be deemed much slower than the formation of oxygen on the surface. Geppert *et al.* [36] performed a similar modelling study of a similar mechanism, and stated the oxygen formation step could be assumed irreversibly due to its high reaction energies, hence $r_{4+} \gg r_{4-}$. Lastly, we assume that the rate of oxygen formation out rules that of the dissolution, which is the fundamental assumption for this numerical approach. This can also be related to the dominating current efficiencies for the OER already mentioned earlier. Consequently, the site coverage of IrO_3 given in Equation 3.25 can be written and simplified to

$$\begin{aligned}\frac{d\Gamma\theta_2}{dt} &= r_2 - r_3 - r_4 = \hat{r}_2 - (r_{3+} - r_{3-}) - (r_{4+} - r_{4-}) \\ &\approx \hat{r}_2 - r_{3+} - r_{4+} \\ &\approx \hat{r}_2 - r_{4+}\end{aligned} \tag{3.32}$$

Applying Equation 3.32 to the acidic and the alkaline model gives

$$\text{Acidic model}: \quad \frac{d\Gamma\theta_2}{dt} \approx \frac{\Gamma k_{2+}^0 \exp\left\{\frac{(1-\alpha_2)\mathrm{F}}{\mathrm{R}T}(E - E_\mathrm{n})\right\}}{1 + \frac{a_{\mathrm{H}+}}{a_{\mathrm{H_2O}}} K_1^0 \exp\left\{-\frac{\mathrm{F}}{\mathrm{R}T}(E - E_\mathrm{n})\right\}} - k_{4+}^0 \Gamma\theta_2 \tag{3.33}$$

$$\text{Alkaline model}: \quad \frac{d\Gamma\theta_2}{dt} \approx \frac{\Gamma k_{2+}^0 \exp\left\{\frac{(1-\alpha_2)\mathrm{F}}{\mathrm{R}T}(E - E_\mathrm{n})\right\} a_{\mathrm{OH}^-}}{1 + \frac{K_1^0}{a_{\mathrm{OH}^-}} \exp\left\{-\frac{\mathrm{F}}{\mathrm{R}T}(E - E_\mathrm{n})\right\}} - k_{4+}^0 \Gamma\theta_2 \tag{3.34}$$

where the potential, E, is a function of time, t, given by integrating equation 3.26 from the initial time, t_i to a time t with a constant sweep rate, ν, yielding

$$E(t) = E_\mathrm{i} + \nu t \tag{3.35}$$

where, E_i, is the initial potential at $t = t_\mathrm{i}$. Though for the degradation data that the microkinetic models are meant to simulate, the degradation measurements were performed by cyclic voltammetry [1, 2], where the sweep rate changes direction after reaching a maximum potential after a time $t = t_\mathrm{max}$. Hence, the potential regime used is described by

$$E(t) = \begin{cases} E_\mathrm{i} + \nu t, & t \leq t_\mathrm{max} \\ E_\mathrm{i} + \nu(2t_\mathrm{max} - t), & t \geq t_\mathrm{max} \end{cases}$$

Solving the simplified differential equation 3.32 for $\Gamma\theta_2(t)$, yields an estimate for the formation of the site coverage of IrO_3, $\Gamma\theta_2(t)$, which participates in the degradation mechanism. The chosen potential regime used by Mayrhofer *et al.* [1] is that of a linear potential sweep, with a constant sweep rate, with two cycles, one cycle with $E_\mathrm{max} = 1.2\,\mathrm{V}$vs RHE and another with $E_\mathrm{max} = 1.6\,\mathrm{V}$vs RHE, both with a sweep rate of $\nu = 2\,\mathrm{mV\,s^{-1}}$. For this study, the latter cycle with dissolution data and the corresponding potential regime was used, capturing the whole

dissolution peak corresponding to this potential change. The potential regime from Schalenbach *et al.* [2] follows the same procedure with the same sweep rate, but only using two cycles with $E_{\max} = 1.5\,\mathrm{V}$vs RHE where the first cycle was chosen. Now, the only unknown parameter in equation 3.33/3.34 is the forward rate constant for step 3.4/3.17, k^0_{4+}, meaning that the solution to Equation 3.32, $\Gamma\theta_2(t)$, is dependent on a value for k^0_{4+}.

The differential equations 3.33 and 3.34 are examples of *stiff differential equations*. Stiff differential equations are mathematically difficult to define unambiguously but they show properties like a solution to a slow and smooth curve is substantially disturbed by nearby rapid solutions [97], such properties force the step size to be unreasonable small in regions where the curve is smooth [98]. Equation 3.33 and 3.34 are considered stiff because of the different sizes of the rate constants in the expression. This equation was solved using a built-in solver in MATLAB®called *ode15s*, which is briefly described in Appendix E.

Now, with a solution for equation 3.32 on the form, $\Gamma\theta_2(t)$, for different values of k^0_{4+} obtained by using *ode15s*, corresponding estimates for the forward rate constant for the dissolution step, k^0_{3+}, could be found by setting the rate of step 3.3/3.16, equal to the rate of dissolution, $\frac{d\mathrm{Ir}}{dt}$, measured by Mayrhofer *et al.*[1] and Schalenbach *et al.* [2] as

$$\begin{aligned} r_3 &= r_{3+} - r_{3-} \approx r_{3+} \\ &= r_{3+} = \frac{da_{\mathrm{Ir}}}{dt}(calc) \end{aligned} \tag{3.36}$$

where the first approximation is still the neglecting of back diffusion of $\mathrm{IrO_4^{2-}}$ for both models. Inserting the respective expressions for the acidic model and the alkaline model for r_{3+} gives

$$\text{Acidic model}: \quad r_{3+} = k^0_{3+} a_{\mathrm{H_2O}} \Gamma\theta_2 = \frac{d\mathrm{Ir}}{dt}(calc) \tag{3.37}$$

$$\text{Alkaline model}: \quad r_{3+} = k^0_{3+} a^2_{\mathrm{OH^-}} \Gamma\theta_2 = \frac{d\mathrm{Ir}}{dt}(calc) \tag{3.38}$$

The *calc* represents the calculated value based on the solution $\Gamma\theta_2(t)$ obtained by

solving 3.32. Then by comparing the calculated dissolution rate to the measured dissolution rate from Mayrhofer *et al.* [1] and Schalenbach *et al.* [2], an estimated value for k^0_{3+} could be found by minimising the difference between the measured dissolution and the calculated dissolution rate, on the basis of k^0_{3+}. This can be described as minimising the square of the differences given as χ^2 for both models.

$$\chi^2 = \left[\frac{d\mathrm{Ir}}{dt}(calc) - \frac{d\mathrm{Ir}}{dt}(meas)\right]^2 \tag{3.39}$$

where *meas* represents the measured dissolution rate reported by Mayrhofer *et al.* [1] and Schalenbach *et al.*[2]. The value of the rate constant, k^0_{3+}, can give an indicator of how fast the degradation reaction occurs.

Table 3.3 contains a summary of the important parameters from the microkinetic model, their description, units, and lastly how they are found.

Table 3.3: A summary of the different constants from the microkinetic model and how they are found

Variable	Description	Unit	Source
Γk^0_{2+}	Product of total concentration of active sites on IrO_2 surface and forward rate constant for rds	$\mathrm{mol\,m^{-2}\,s^{-1}}$	Fit from data
K^0_1	Chemical equilibrium constant for step 1	-	Fit from data
α	Charge transfer coefficient	-	Fit from data
k^0_{3+}	Chemical forward rate constant for dissolution step	$\mathrm{s^{-1}}$	Found by minimising χ^2
k^0_{4+}	Chemical forward rate constant for oxygen formation step	$\mathrm{s^{-1}}$	Predetermined

3.3.1 Continuum model for an AEM-WE

Since the continuum model by SINTEF [3] is made to simulate the operation of an AEM-WE, then it was most reasonable to implement the alkaline model into the continuum model where it was fitting[vii]. Implementing a microkinetic model describing the dissolution of the catalyst layer into a cell-level model may

capture the details of the degradation process more accurately, than just assuming they follow a Butler-Volmer type of reaction. This way, the mechanism of the degradation has an effect on the output, whereas, without the microkinetic model, it would seem as if the dissolution is described by a single step. This means that the way dissolution and current in the model were described in Section 2.5 had to change. The model descriptions for the membrane and the cathode side were left unaltered. As mentioned in Section 2.5, the model is solving seven governing equations concurrently, by the use of *ode15i* [3]. By implementing the microkinetic model to describe dissolution, the conservation of site coverage for IrO_3, Equation 3.34, was added to the system of equations in the continuum model.

With the assumption of an rds and quasi-equilibrium, Equation 3.31 describes the total rate of the OER, and hence the anodic current related to the oxygen evolution at the anode. Until now, the reactions and the prior numerical approach have not dealt with the presence of an ionomer, only IrO_2 covered in an electrolyte. In order to be consistent, the derived alkaline model described in Section 3.2 and 3.3 was then assumed to only apply for the electrolyte-covered catalyst. Consequently, this also meant that there was assumed no degradation for the catalyst which is covered by an ionomer, see Figure 3.2. Li *et al.* [18] found that ionomer detachment from the catalyst surface led to a higher degradation rate, meaning that the presence of ionomer could keep the catalyst particles stable under operation. The resulting change is then that Equation 2.15 remains unchanged, and is still described by Butler-Volmer, and that Equation 2.14 is replaced with

$$i_{\mathrm{L}}^{rx} = a_{\mathrm{L}} n \mathrm{F} \hat{r}_2(\eta_{\mathrm{L}}^{surf}) \tag{3.40}$$

where a_{L} has replaced $(1 - X_{\mathrm{Inmr}})a$, indicating the interfacial area covered by electrolyte. Subsequently, $X_{\mathrm{Inmr}}a$ is replaced with a_{Inmr}, and that way, omitting the use of X_{Inmr}. This implies that it is only a_{L} which is decreasing as a result of the degradation of electrolyte-covered catalyst, while a_{Inmr} stays the same. The initial value for the interfacial area exposed to electrolyte and the part covered by ionomer is set to be the same, and half the original value of a as $a_{\mathrm{L}} = a_{\mathrm{Inmr}} = 1{\cdot}10^6\ \mathrm{m^2\,m^{-3}}$.

[vii] The continuum model with my alterations is available on the open Github repository: `https://github.com/CHANNEL-H2020/AlkalineElectrolyzerContinuumModel/tree/Pally_AEM_WE_diss`

Equation 3.40 has also put emphasis on the substitution of $E - E_{\mathrm{n}}$ with the surface overpotential related to the electrolyte-covered catalyst, η_{L}^{surf}, in addition, the activity of hydroxide, a_{OH^-}, within $\hat{r}_2$ as showed in Equation 3.31 is now calculated by the means of the continuum model.

Figure 3.2 illustrates the effect of implementing the alkaline microkinetic model into the continuum model. Because of consistency, there is only catalyst dissolution where the catalyst is exposed to the electrolyte, and not ionomer, whereas there is still the formation of oxygen in both phases. Furthermore, it shows the exchange of OH^- and H_2O between the ionomer and electrolyte phase.

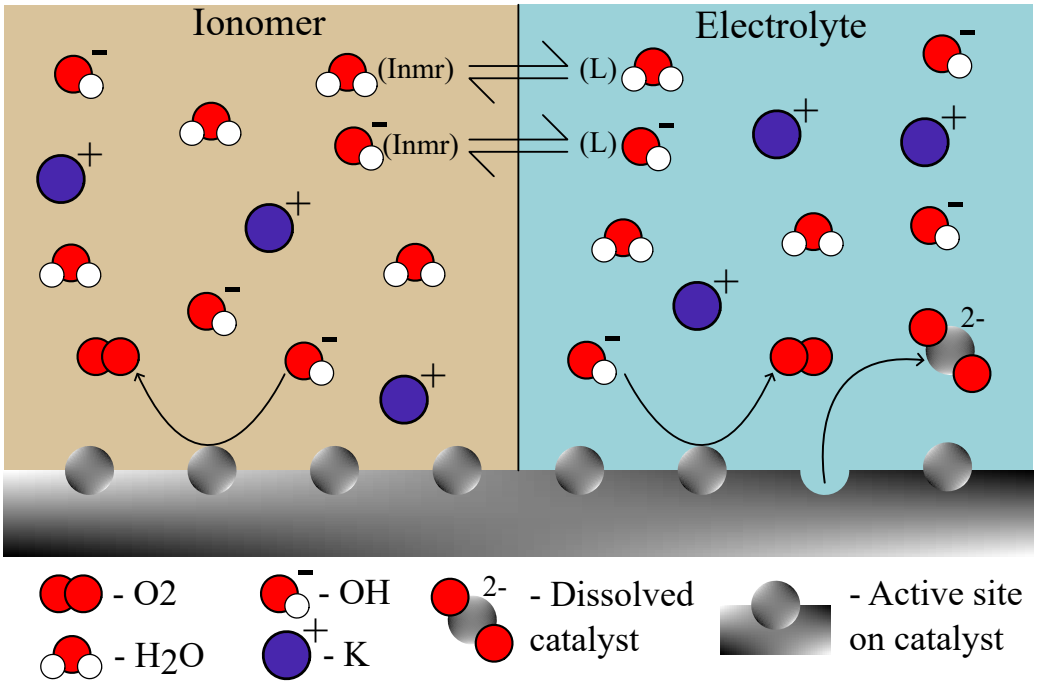

Figure 3.2: Anode catalyst surface of an anion-exchange membrane water electrolyser partially covered in ionomer and partially exposed to the electrolyte. It illustrates the effect of the implementation of the microkinetic model into the continuum model regarding the dissolution of the catalyst layer. The transfer of hydroxide and water between the two phases is also added, as well as oxygen formation.

The alteration of how the current is calculated will also affect the oxygen produced in the anode by Equation 2.16 and also the amount of hydroxide consumed by Equation 2.17. This will also indirectly affect the molar transport of ions expressed through Equation 2.12 and also the pressure gradient in Equation 2.10.

Finally, the dissolution will not be described by Butler-Volmer directly, but by the microkinetic expression in Equation 3.38. Equation 3.38 would then replace

Equation 2.19 as

$$i_{\text{Diss}}^{rx} = a_{\text{L}} n \text{F} r_{3+} \tag{3.41}$$

and the source term for the dissolution of IrO_2 described by Equation 2.20 was then changed to

$$S_{\text{IrO}_2} = -a_{\text{L}} r_{3+} \bar{V}_{\text{IrO}_2} \tag{3.42}$$

Regardless of the resulting rate constant from the alkaline model, the ratio $\frac{k_{4+}^0}{k_{3+}^0}$ was also changed when running simulations. This was done since the k_{3+}^0 values ended up being dependent on a given value of k_{4+}^0, making the results more qualitative. Hence, the ratio was also changed to study the effect of larger differences in k_{4+}^0 and k_{3+}^0 on the output of the model. This is because it is often assumed that the rate of dissolution is usually much lower than that of oxygen formation, and that could be studied as well, and this would be a qualitative measure for that.

Table 3.4 contains the standard operating conditions and the initial values for quantities related to the simulation of an AEM-WE. The predefined variables are above the midrule in the table, while initial values based on the predefined parameters are below the midrule.

Table 3.4: Model parameters used for the continuum model after the implementation of the alkaline model. The constants from the alkaline model are given in Section 4

Parameter	Value	[unit]
c_{OH^-}	1	$mol\,L^{-1}$
i_n	0.256	$A\,m^{-2}$
a_L	$1 \cdot 10^6$	$m^2\,m^{-3}$
a_{Inmr}	$1 \cdot 10^6$	$m^2\,m^{-3}$
ϵ_{IrO_2}	0.14	[-]
T	333.15	K
$\bar{V}_{IrO_2}$	$1.9230 \cdot 10^{-5}$	$m^3\,mol^{-1}$
I	30000	$A\,m^{-2}$
r	$4.2 \cdot 10^{-7}$ [a]	m
N_p	$4.51 \cdot 10^{17}$ [b]	m^{-3}

[a] Calculated from Equation 2.21 based on ϵ_{IrO_2} and a_L

[b] Calculated from Equation 2.22 based on r and N_p

4 Results

To study the dissolution of iridium oxide during OER, it was assumed that the current originating from dissolution was negligible compared to the current related to the OER. Moreover, a quasi-steady-state was assumed for the reaction where step 3.2 and 3.15 were assumed as the rds in the acidic and alkaline model respectively. This led to the derived expression for the rate of reaction given in equation 3.30 and 3.31, where Γk_{2+}^0, α_2, and K_1^0 was unknown. In order to find estimated values for these parameters, a numerical fitting procedure was undertaken using MATLAB for both the acidic model and the alkaline model based on linear sweep voltammetry (LSV) in acidic[1, 24, 95, 50] and alkaline[2, 50, 95] conditions respectively. Though, only the results from Mayrhofer *et al.* [1] and Schalenbach *et al.*[2] are reported here since those are directly related to the degradation data which the model is meant to reproduce. From there a solution to equation 3.32 for three different values of k_{4+}^0 could be obtained giving values for the site coverage of IrO_3 as a function of time, $\Gamma\theta_2(t)$. The site coverage was then used to estimate the rate of dissolution r_{3+}. This section contains the fitting parameters of Γk_{2+}^0, α_2, and K_1^0 from the LSV data from Mayrhofer *et al.*[1] and Schalenbach *et al.*[2], $\Gamma\theta_2$ as a function of time, t, and potential, E, and lastly the rate of dissolution for both the acidic and alkaline model as a function of time.

4.1 Acidic model

The acidic model was based on the assumption that reaction 3.2 is the rds, which leads to the rate of reaction expressed as equation 3.30. Equation 3.30 has three unknown parameters, the product between the concentration of active sites on the surface and the forward chemical rate constant for the rds, Γk_{2+}^0, α, and K_1^0. The values of these parameters were obtained by numerical fitting carried out in MATLAB of Equation 3.30 to the measured LSV curves in acidic media. The LSV curves were extracted from Scohy *et al.* [24], Damjanovic *et al.* [95], Cherevko *et al.* [50], and Mayrhofer *et al.*[1], though only the result from Mayrhofer is given in this section, and the rest in Appendix C.

The result of fitting Equation 3.30 to the sampled LSV curve from Mayrhofer *et al.*[1] which corresponds to the electrode of which the degradation was measured is shown in Figure 4.1. Sampled data are represented by red squares and the fitted

result is the black line. In addition, the coefficient of determination, R^2, is also provided.

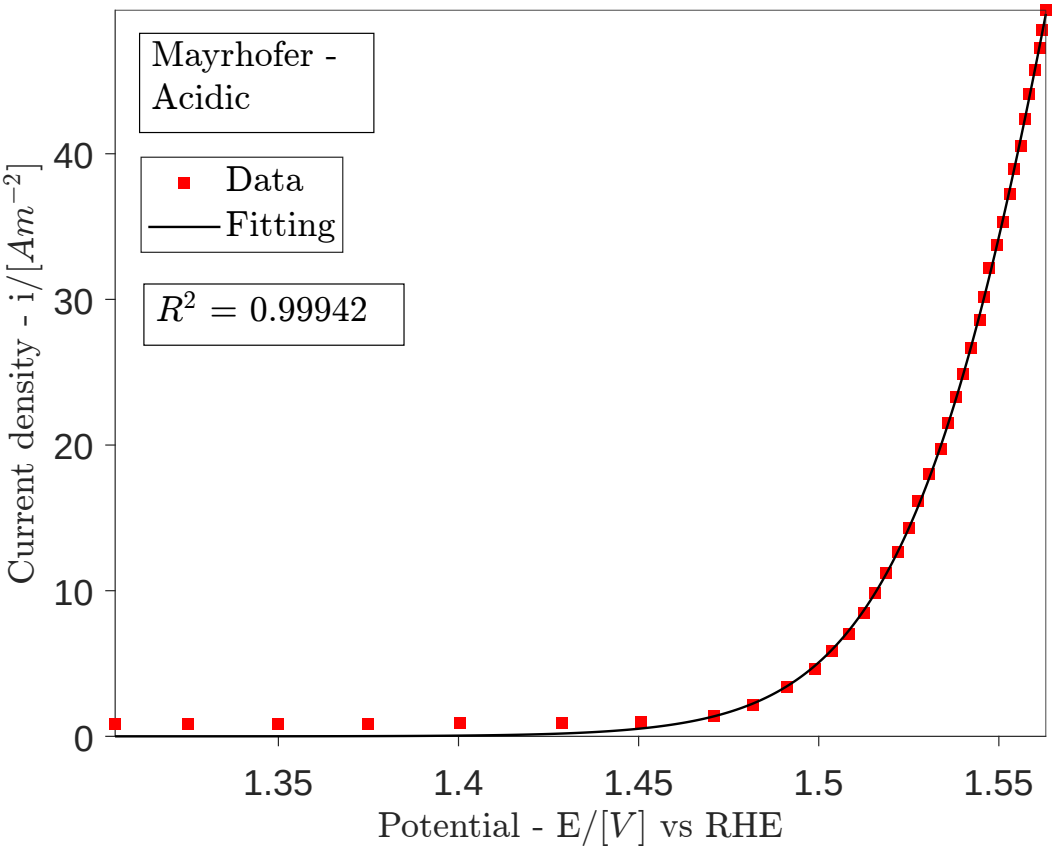

Figure 4.1: The sampled data from a linear sweep voltammetry on hydrous IrO_2 in $0.1\,\mathrm{mol\,L^{-1}}$ H_2SO_4 from Mayrhofer *et al.* [1] in red squares and the corresponding curve fitting black line. This electrode was cycled 20 times and shares the preparation history of the electrode in which the degradation is measured. The coefficient of determination is $R^2 = 0.99942$

The modelling parameters used for solving Equation 3.33 were the fitting parameters obtained by the fitting of Equation 3.30 to LSV data, and the temperature and activity of protons during the measuring of the degradation data done by Mayrhofer *et al.*[1]. The degradation was measured on a hydrous iridium oxide electrode, which was cycled 20 times and a sweep rate of $\nu = 2\,\mathrm{mV\,s^{-1}}$ and the activity of the protons was approximated to be equal to the concentration of protons in $0.1\,\mathrm{mol\,L^{-1}}$ H_2SO_4. Table 4.1 shows the parameters used for the acidic model.

Table 4.1: Model parameters used for the computation of the dissolution rates for the acidic model. Above the horizontal line are the results from the numerical fitting of equation 3.30 to sampled data extracted from measured LSV data by Mayrhofer *et al.*[1]. Γk_{2+}^0, α_2, and K_1^0 were fitting parameters and the 95% confidence interval is provided in parenthesis after the calculated value by MATLAB. The corresponding LSV curve with the sampled data and the coefficient of determination are shown in Figure 4.1

Parameter	Value		[Unit]
$\Gamma k_{2+}^0 \cdot 10^5$	1.954	$(1.9 - 5.8)$	$[\mathrm{mol\,m^{-2}}]$
$K_1^0 \cdot 10^{-7}$	1.532	$(0.65 - 2.06)$	$[-]$
α	0.7881	$(0.67 - 0.91)$	$[-]$
T		298[a]	[K]
$c_{\mathrm{H^+}}$		0.2[b]	$[\mathrm{mol\,L^{-1}}]$

[a] Temperature for electrochemical measurements from Mayrhofer *et al.*[1].

[b] The concentration of H^+ given by Mayrhofer *et al.*[1] to be $0.1\,\mathrm{mol\,L^{-1}}$ H_2SO_4, and full dissociation was assumed.

With the modelling parameters in Table 4.1, a solution to Equation 3.33 could be found for different values of k_{4+}^0. The differential equation, Equation 3.33, is solved over the time measured by Mayrhofer *et al.* [1] for the dissolution peak with $E_{\max} = 1.6\,\mathrm{V vs\ RHE}$ and the potential regime as described in Section 3 with a sweep rate of $\nu = 2\,\mathrm{mV\,s^{-1}}$. The solution to equation 3.33 for $k_{4+}^0 = \{0.1\,\mathrm{s^{-1}}, 0.01\,\mathrm{s^{-1}}, 0.001\,\mathrm{s^{-1}}\}$ as a function of time is given in Figure 4.2 along with the potential regime, $E(t)$, in grey dashed lines.

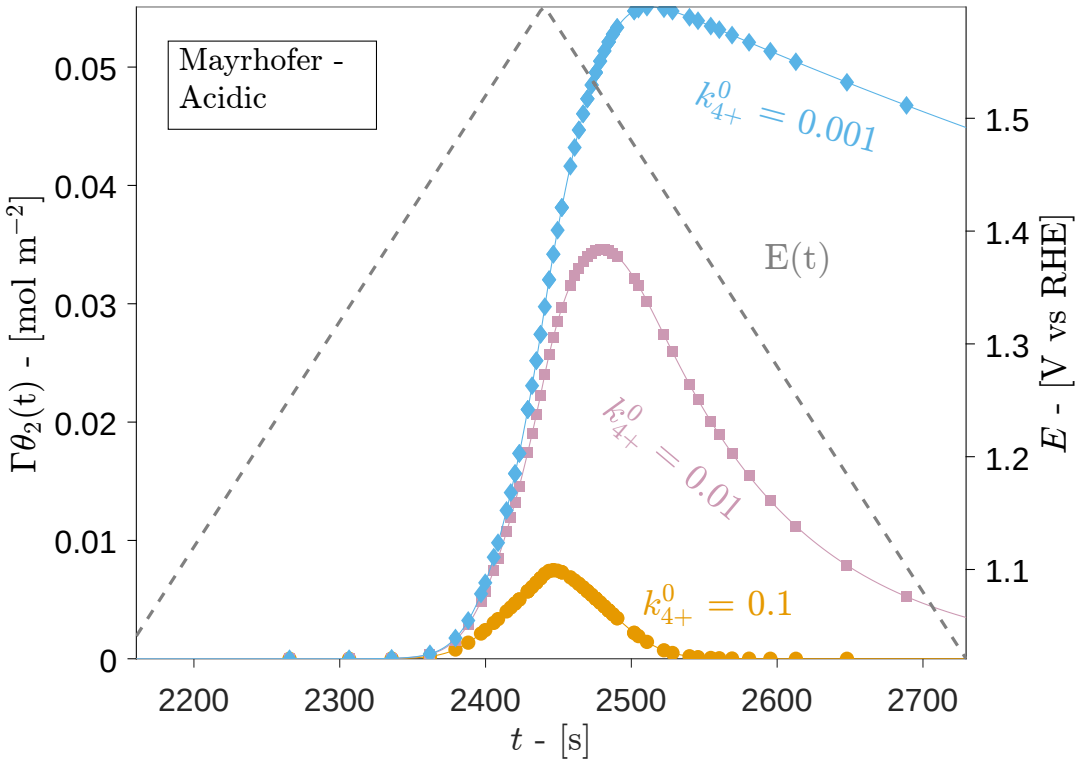

Figure 4.2: The solution of equation 3.33 describing the site coverage of IrO_3, denoted $\Gamma\theta_2$, as a function of time, t, for three different values of k^0_{4+} based on the data obtained from Mayrhofer *et al.* [1] and the model parameters from Table 4.1. The potential regime during the degradation study by Mayrhofer *et al.* [1] is also provided on the right y-axis. The markers represent the sampled data points for time from the degradation data

The solution to equation 3.33 based on the parameters in table 4.1 was also plotted as a function of the potential during the potential sweep in Figure 4.3. The measured degradation data by Mayrhofer *et al.* [1] is plotted against the second y-axis, denoted $\frac{dIr}{dt}$, in grey dashed lines. The direction of the linear potential sweep is also given in the figure as black and grey arrows.

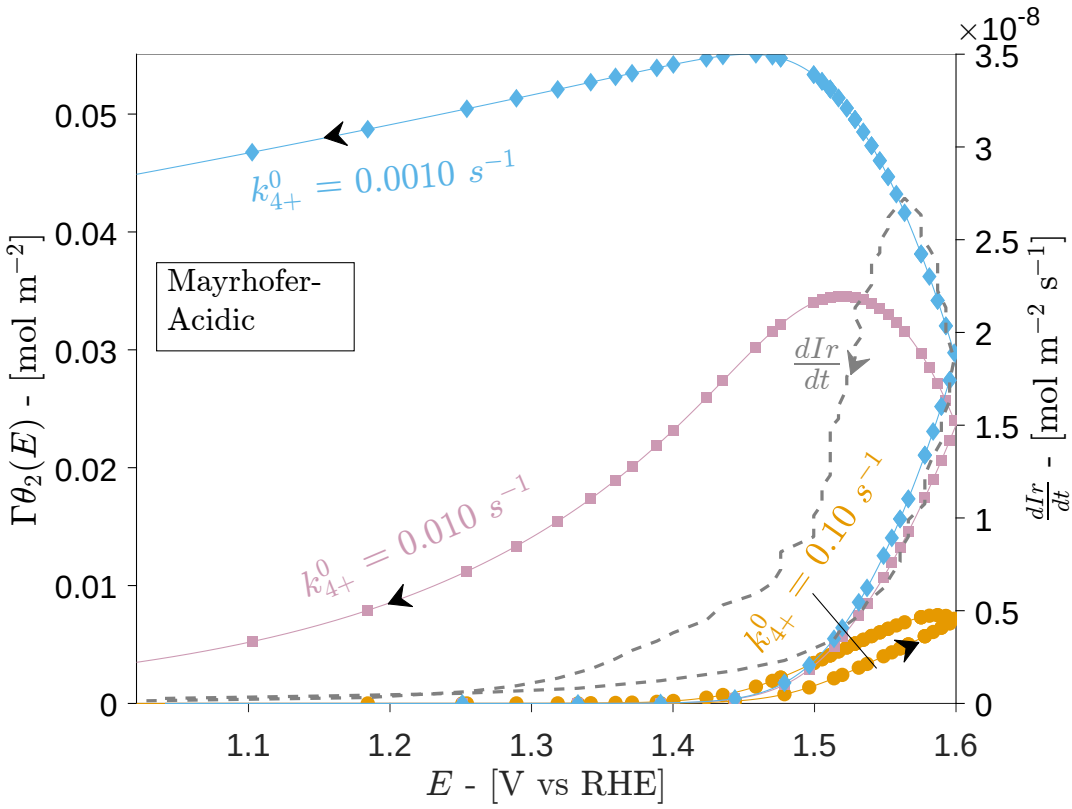

Figure 4.3: The solution of equation 3.33 describing the site coverage of IrO_3, denoted $\Gamma\theta_2$, as a function of potential, E, for three different values of k^0_{4+} based on the data obtained from Mayrhofer *et al.* [1]. The degradation data from Mayrhofer *et al.* [1] is also provided for reference on the right y-axis. The markers represent the sampled points from the degradation data

Lastly, the rate of degradation was obtained by minimising χ^2 as described by equation 3.39 with respect to k^0_{3+} for the acidic model. The resulting degradation rates along with the minimised values for k^0_{3+} are given in Figure 4.4 as a function of time. The degradation data, which the calculated dissolution rates are meant to reproduce, are also given in black dashed lines marked with $\frac{d\mathrm{Ir}}{dt}$, along with the potential regime, $E(t)$ in grey dashed lines.

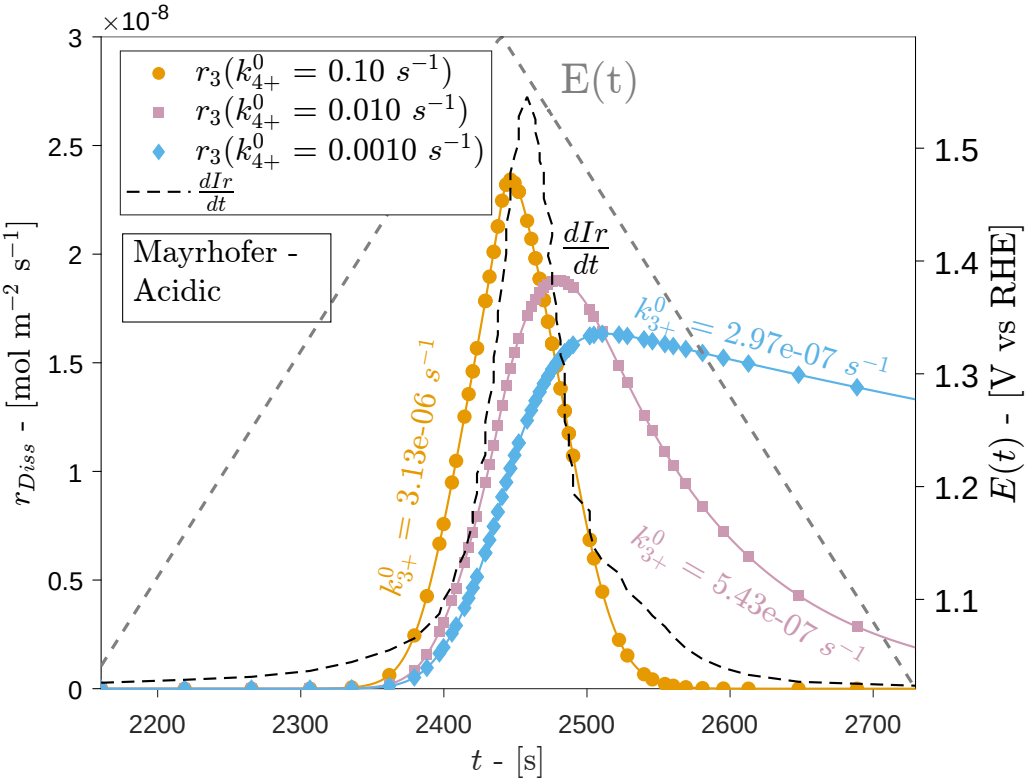

Figure 4.4: The rate of degradation, r_{3+}, as a function of time, t, for three different values of k^0_{4+}, based on the data from Mayrhofer *et al.* [1]. The resulting rate constant for the degradation, k^0_{3+}, is also provided with their respective solutions. The measured rate of dissolution from Mayrhofer *et al.* [1] in black dashed lines and the potential regime used under the measuring of degradation is also provided as grey dashed lines. The markers represent the sampled data from the degradation data

The chemical forward rate constants for the dissolution rates in Figure 4.4 can be seen in Table 4.2.

Table 4.2: The chemical rate constants for dissolution, k^0_{3+}, as a result from the minimisation of Equation 3.39 for the acidic model for $k^0_{4+} = \{0.1\,\mathrm{s}^{-1}, 0.01\,\mathrm{s}^{-1}, 0.001\,\mathrm{s}^{-1}\}$. The values are also showed in Figure 4.4.

Rate constant	Value		
k^0_{4+} [s^{-1}]	0.1	0.01	0.001
k^0_{3+} [s^{-1}]	$3.13 \cdot 10^{-6}$	$5.43 \cdot 10^{-7}$	$2.97 \cdot 10^{-7}$

4.2 Alkaline model

Much like the acidic model, the alkaline model was based on the assumption that reaction 3.15 is the rds, and this assumption gives the expression for the whole

reaction rate as Equation 3.31. The three unknowns in this expression are Γk_{2+}^{0}, α, and K_{1}^{0}. These unknowns were fitted by a numerical fitting procedure in MATLAB based on the measured LSV data in alkaline conditions from Cherevko *et al.* [50], Damjanovic *et al.* [95], and Schalenbach *et al.* [2], though only the results from Schalenbach is reported in this section since the degradation data in alkaline media was from Schalenbach *et al.* [2]. The result obtained based on Cherevko *et al.* [50] and Damjanovic *et al.*[95] are given in Appendix C.

The numerical fitting of Equation 3.31 to the LSV data from Schalenbach *et al.* [2] is shown in Figure 4.5, where the sampled data are represented in magenta diamonds and the resulting fit is the black line. The coefficient of determination, R^2, is also displayed.

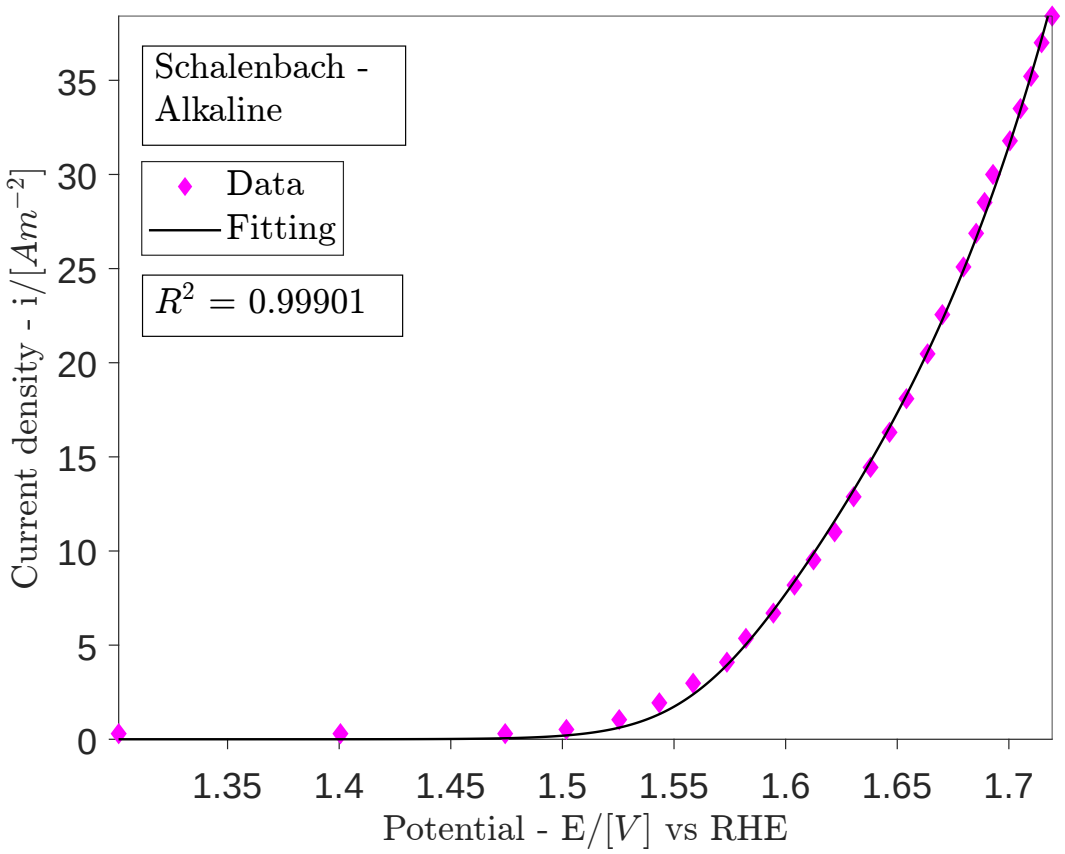

Figure 4.5: The sampled data from the LSV measurement on Ir in $0.05\,\mathrm{mol\,L^{-1}}$ NaOH from Schalenbach *et al.* [2] in magenta diamonds and the corresponding curve fitting black line. The coefficient of determination is $R^2 = 0.99901$

The modelling parameters for solving Equation 3.34 were the fitting parameters obtained by the fitting of Equation 3.31 to LSV data, and the temperature and

activity of hydroxide ions during the measuring of the degradation data done by Schalenbach *et al.*[2]. The activity of the hydroxide ions was approximated to be equal to the concentration. Table 4.3 shows the parameters used for the alkaline model.

Table 4.3: Model parameters used for the computation of the dissolution rates for the acidic model. Above the horizontal line are the results from the numerical fitting of equation 3.31 to sampled data extracted from measured LSV data by Schalenbach *et al.*[2]. Γk_{2+}^0, α_2, and K_1^0 were fitting parameters and the 95% confidence interval is provided in parenthesis after the calculated value by MATLAB. The corresponding LSV curve with the sampled data and the coefficient of determination are shown in Figure 4.5

Parameter	Value	[Unit]
$\Gamma k_{2+}^0 \cdot 10^5$	$3.684 \quad (2.9 - 4.4)$	$[\mathrm{mol\,m^{-2}}]$
$K_1^0 \cdot$	$2436 \quad (1757 - 3115$	$[-]$
α	$0.7146 \quad (0.70 - 0.73x)$	$[-]$
T	298^{a}	[K]
$c_{\mathrm{OH^-}}$	0.05^{b}	$[\mathrm{mol\,L^{-1}}]$

[a] Temperature for electrochemical measurements from Schalenbach *et al.*[2].

[b] The concentration of $\mathrm{OH^-}$ given by Schalenbach *et al.*[2] to be $0.05\,\mathrm{mol\,L^{-1}}$ NaOH, and full dissociation was assumed.

By using the model parameters in Table 4.3, a solution, $\Gamma\theta_2(t)$, to equation 3.34 could be obtained. The solution to equation 3.34 is given as a function of time in Figure 4.6 for $k_{4+}^0 = \{0.1\,\mathrm{s^{-1}}, 0.01\,\mathrm{s^{-1}}, 0.001\,\mathrm{s^{-1}}\}$. The used potential regime, $E(t)$, by Schalenbach *et al.*[2] for the dissolution peak chosen is plotted against the right y-axis for $E_{\max} = 1.5\,\mathrm{V vs\ RHE}$ and a sweep rate $\nu = 2\,\mathrm{mV\,s^{-1}}$.

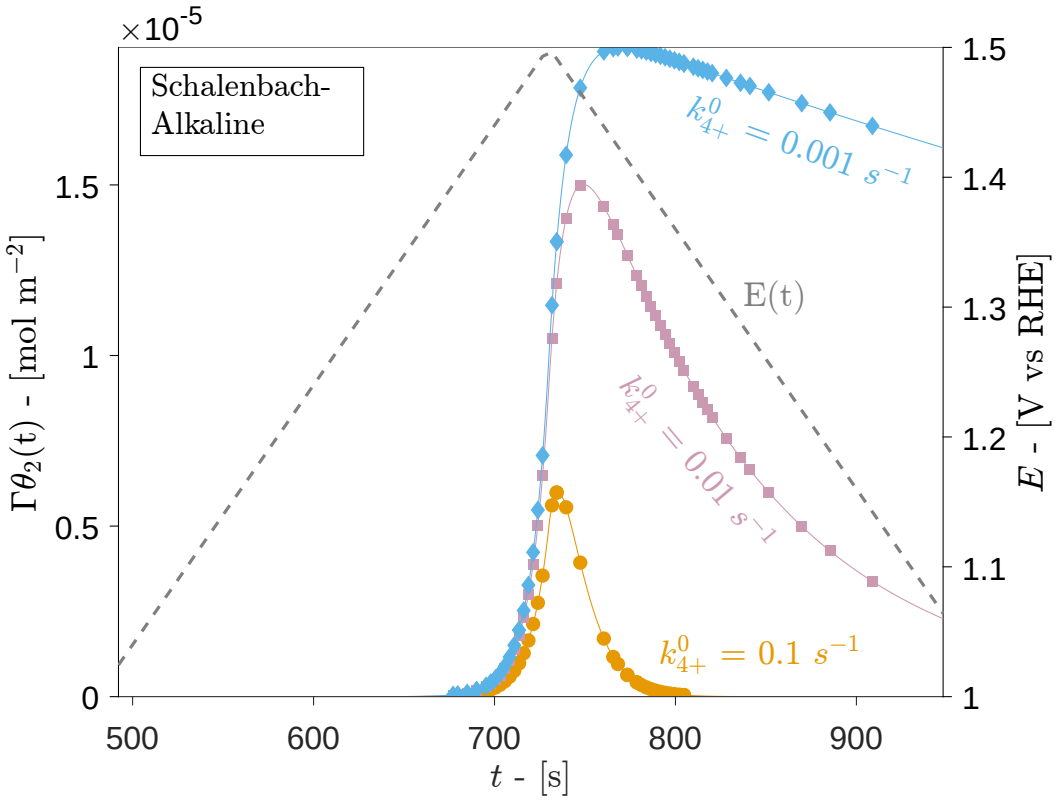

Figure 4.6: The solution of Equation 3.34 describing the site coverage of IrO_3, denoted $\Gamma\theta_2$, as a function of time, t, for three different values of k^0_{4+} based on the data obtained from Schalenbach *et al.* [2]. The potential regime during the degradation study by Schalenbach *et al.* [2] is also provided on the right y-axis. The markers represent the sampled data from the degradation data.

The solution to Equation 3.34 was also plotted as a function of potential in Figure 4.7. Here, the measured dissolution rate by Schalenbach *et al.* [2] as a function of potential is also plotted against the right y-axis, denoted $\frac{d\text{Ir}}{dt}$. The direction of the potential sweep is also given by arrows.

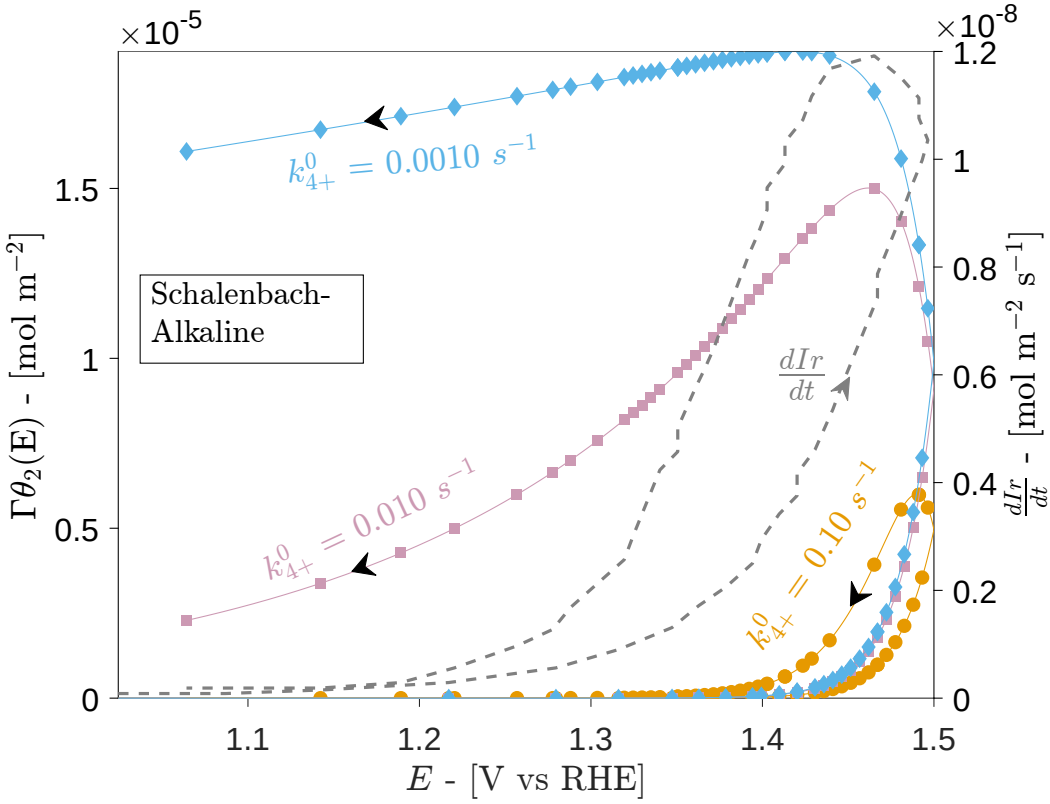

Figure 4.7: The solution of equation 3.34 describing the site coverage of IrO_3, denoted $\Gamma\theta_2$, as a function of potential, E, for three different values of k^0_{4+} based on the data obtained from Schalenbach *et al.* [2]. The degradation data from Schalenbach *et al.* [2] is also provided for reference on the right y-axis. The markers represent sampled data from the degradation data

Lastly, the estimate of the dissolution rate, r_3, for the three different values of k^0_{4+} was found by minimising χ^2 expressed by equation 3.39 with respect to k^0_{3+} for the alkaline model. The result is given in figure 4.8 as a function of time, with the minimised values of k^0_{3+} also given in the figures. The measured degradation data, which the simulated dissolution rates were meant to reproduce, is also given in black dashed lines and denoted $\frac{d\mathrm{Ir}}{dt}$, while the potential regime is given in grey dashed lines.

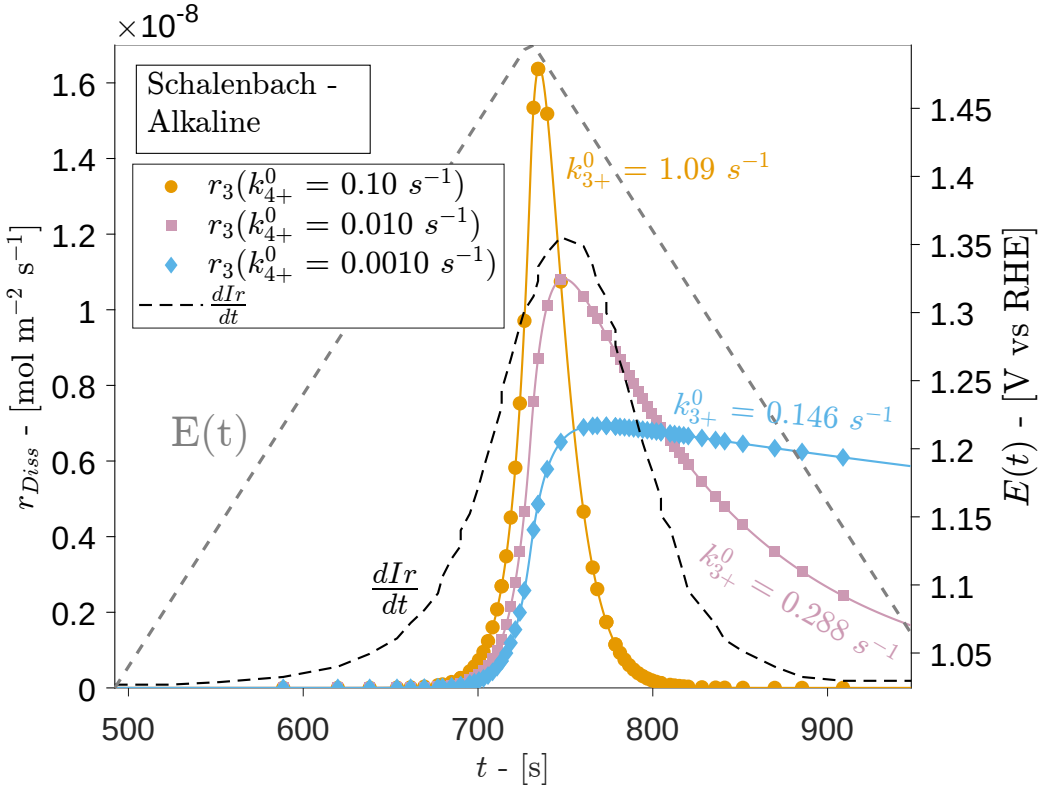

Figure 4.8: The rate of degradation, r_{3+}, as a function of time, t, for three different values of k^0_{4+}, based on the data from Schalenbach *et al.* [2]. The resulting rate constant for the degradation, k^0_{3+}, is also provided with their respective solutions. The measured rate of dissolution from Schalenbach *et al.* [2] in black dashed lines and the potential regime used under the measuring of degradation is also provided as grey dashed lines. Markers represent the sampled data from the degradation data.

The chemical forward rate constants for the dissolution rates in Figure 4.8 can be seen in Table 4.4.

Table 4.4: The chemical rate constants for dissolution, k^0_{3+}, as a result from the minimisation of Equation 3.39 for the alkaline model for $k^0_{4+} = \{0.1\,\mathrm{s}^{-1}, 0.01\,\mathrm{s}^{-1}, 0.001\,\mathrm{s}^{-1}\}$. The values are also shown in Figure 4.8.

Rate constant	Value		
k^0_{4+} [s^{-1}]	0.1	0.01	0.001
k^0_{3+} [s^{-1}]	1.09	0.288	0.148

4.3 Continuum model for AEM-WE

The continuum model was developed by SINTEF and described in more detail by Gerhardt *et al.*[3] and the most important aspects of how the implementation of the microkinetic model affects the output are described in Section 2.5 and 3. This

modelling framework is meant to simulate the operation of an AEM-WE, which operates under alkaline conditions, thus it was most consistent to implement the alkaline model based on the results from Schalenbach *et al.* [2] presented in the previous section into the continuum model. All the simulations were done with polarisation conditions. The time to reach the maximum operational current was always set to be $t = 36\,000\,\mathrm{s}$, meaning that lower maximum operational current densities also correspond to a slower increase in current per time. With an example, this means that when simulating the operation of an AEM-WE with an operational current of $i_{\max} = 30\,000\,\mathrm{A\,m^{-2}}$, compared to that of a $i_{\max} = 300\,\mathrm{A\,m^{-2}}$, they will both reach their operational current after $t = 36\,000\,\mathrm{s}$. This is important to keep in mind for this section.

The degradation expressed by Equation 3.42 is meant to decrease the available surface area of the electrolyte-covered catalyst layer over time, expressed as the specific interfacial area, a_{L}. Moreover, the modelling framework calculates a_{L} as a function of both time and position across the anode catalyst layer (CL) thickness during the polarisation. Since this is a quantitative study, the effect of the ratio between k^0_{4+} and k^0_{3+}, and the magnitude of the operational current on degradation was also studied.

First, the highest rate constants in Table 4.4 from the results of the alkaline model were chosen as model parameters used for the study of the effect of different maximum current densities, $i_{\max}$. Thus, Figure 4.9 was made by choosing $k^0_{4+} = 0.1\,\mathrm{s^{-1}}$ and the corresponding value of $k^0_{3+} = 1.09\,\mathrm{s^{-1}}$ from Table 4.4, and setting the operational current density, $i_{\max}$, to be $i_{\max} = \{30\,000\,\mathrm{A\,m^{-2}}, 3000\,\mathrm{A\,m^{-2}}, 300\,\mathrm{A\,m^{-2}}, 30\,\mathrm{A\,m^{-2}}, 3\,\mathrm{A\,m^{-2}}\}$. Keep in mind that the operational current given in the legend is not achieved before $36\,000\,\mathrm{s}$.

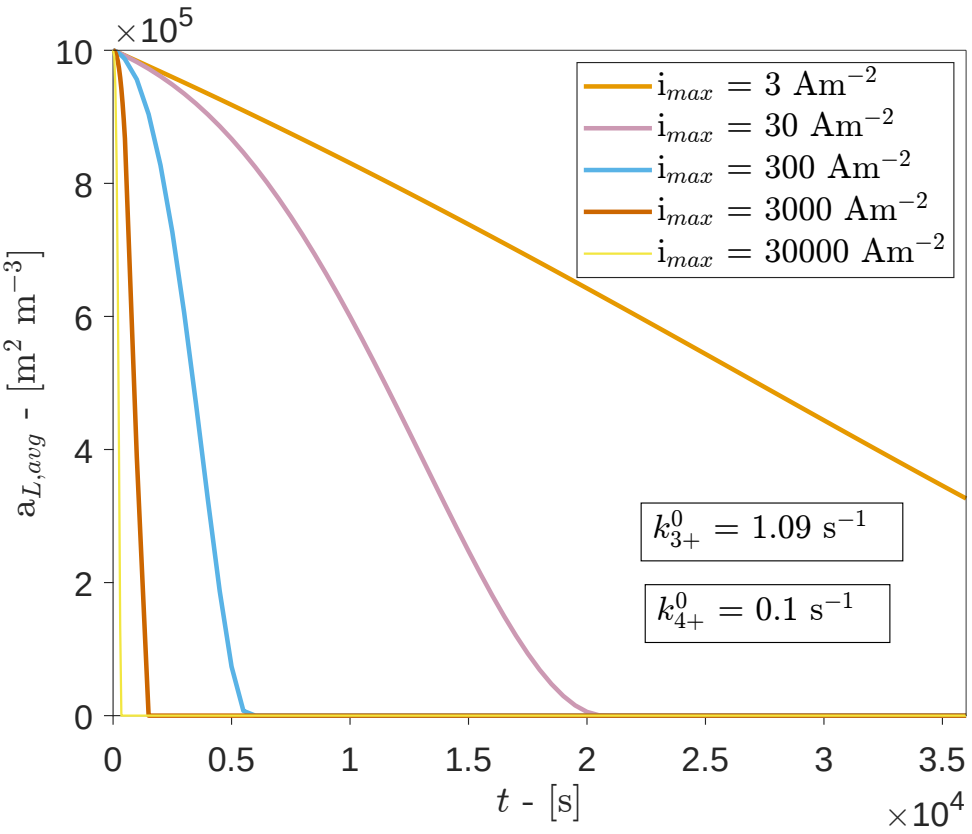

Figure 4.9: Average specific interfacial area, a_{L}, as a function of time, t, with the highest pair of rate constants obtained in the alkaline model from Table 4.4 for five different maximum current densities, i_{max}. The simulation was done under polarisation mode.

Figure 4.9 illustrates the effect of implementing the alkaline model described in section 3.3 on the average specific interfacial area of the electrolyte-covered catalyst layer. With the obtained rate constants from the alkaline model to describe both the reaction rate on the surface of the electrolyte-covered catalyst, through Equation 3.40, and the degradation of the available surface, with Equation 3.42, it seems as a_{L} disintegrates within an instant for normal operational currents, compare i_{max} to operational current densities in Table 1.1. It is not before the operational current density becomes as low as $3\,\mathrm{A\,m^{-2}}$ that the specific interfacial area seems to not dissolve within the ten hours of operation, but a_{L} still declines quite rapidly as a catalyst.

Figure 4.9 describes the average value for a_{L} for different times, and also for different current densities under a polarization of the AEM-WE. It is interesting, however, to see how the local interfacial area changes with time. Figure 4.10 shows

both the relative interfacial area, Figure 4.10a, and the regular interfacial area, Figure 4.10b, as a function of normalised anode catalyst thickness for a polarisation with operational current of $i_{\max} = 3\,\mathrm{A\,m^2}$ from Figure 4.9. In the normalised anode catalyst thickness, a value of 0 represents the interface with the PTL while a value of 1 represents the interface with the AEM. The figure can be interpreted as taking a snapshot of the anode catalyst layer covered in the electrolyte at $t = \{600\,\mathrm{s}, 1600\,\mathrm{s}, 2600\,\mathrm{s}, 3600\,\mathrm{s}\}$. The simulation with an operational current density of $3\,\mathrm{A\,m^{-2}}$ from Figure 4.9 was chosen since it was the only simulation where the electrolyte-covered catalyst layer was not totally spent and lasted for the whole duration.

Figure 4.10b shows that for a constant increase in current of this magnitude, a_{L} decreases quite linearly with time/current density. It also seems like the interfacial area is the same across the entire catalyst layer for every time frame. Figure 4.10a displays the relative local changes across the anode catalyst layer. By the look of Figure 4.10a it seems that there is most catalyst closest to the PTL as time goes by. From the PTL the electrolyte-covered specific interfacial area decreases the closer it comes to the AEM, and moreover, it also decreases more rapidly closer to the AEM as well. However, it can also be seen from Figure 4.10a that the largest local difference across the anode catalyst layer is around 0.006 %, which is not big at all, insinuating that the anode catalyst layer is, in fact, degrading quite uniformly across the anode catalyst layer for this magnitude in operational current and for the rate constants obtained from the alkaline model.

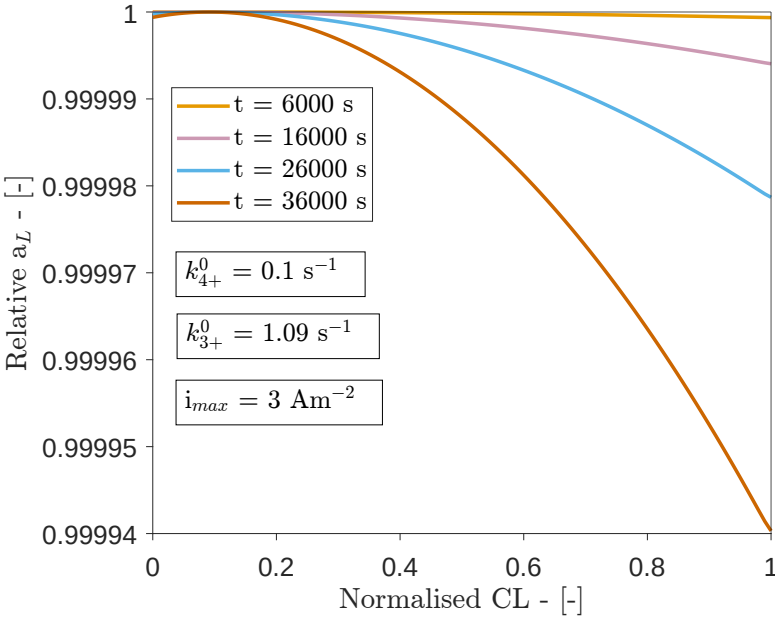

(a) Relative specific interfacial area, a_{L}, as a function of normalised catalyst layer (CL) thickness with the highest pair of rate constants obtained from the alkaline model for four different time frames. The maximum current density of $i = 3\,\mathrm{A\,m^{-2}}$ from Figure 4.9 was chosen.

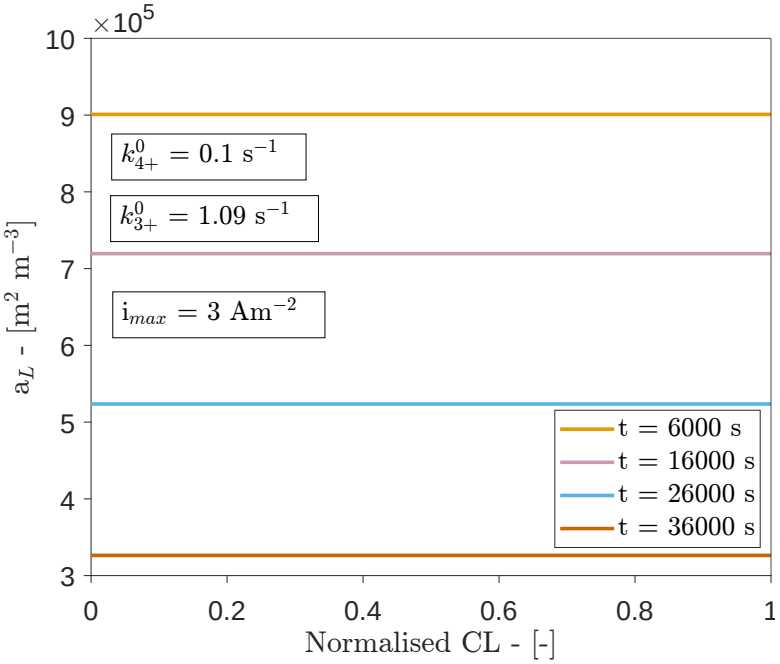

(b) Specific interfacial area, a_{L}, as a function of normalised catalyst layer (CL) thickness with the highest pair of rate constants obtained from the alkaline model for four different time frames. The maximum current density of $i = 3\,\mathrm{A\,m^{-2}}$ from Figure 4.9 was chosen.

Figure 4.10: Regular and relative specific interfacial area, a_{L}, as a function of normalised catalyst layer (CL) thickness where 0 represents the interface with the PTL and 1 means interface with AEM. The figure shows the spatial a_{L} for the average a_{L} from Figure 4.9 and $i_{\mathrm{max}} = 3\,\mathrm{A\,m^{-2}}$ for four different time frames. The simulation with $i_{\mathrm{max}} = 3\,\mathrm{A\,m^{-2}}$ from Figure 4.9 was chosen because a_{L} did not become zero and could give the best visualisation of the trends.

Since the rate constants obtained in the alkaline model given in Table 4.4 were so close in magnitude, they would not show any new properties regarding the operation of an AEM-WE. Hence, the ratio between the forward rate constant for oxygen formation by step 3.17, k^0_{4+}, and the forward rate constant for the dissolution by step 3.16, k^0_{3+}, was changed independently of the results from the alkaline model. Motivated by the rapid dissolving surface from the ratio of around $\frac{k^0_{4+}}{k^0_{3+}} \approx 0.1$ for the operational current of $i = 30\,000\,\mathrm{A\,m^{-2}}$, the ratio was instead set to be $\frac{k^0_{4+}}{k^0_{3+}} = \{10, 100, 1000\}$ and with the operational current of $i = 30\,000\,\mathrm{A\,m^{-2}}$.

Figure 4.11 displays the average interfacial area of the electrolyte exposed catalyst layer, a_L, as a function of time, t, for the same operational current of $i = 30\,000\,\mathrm{A\,m^{-2}}$. It is essentially illustrating the effect of the ratio $\frac{k^0_{4+}}{k^0_{3+}}$ on a_L. The interfacial area is spent quite fast for $\frac{k^0_{4+}}{k^0_{3+}} = 10$ and $\frac{k^0_{4+}}{k^0_{3+}} = 10$, compared to $\frac{k^0_{4+}}{k^0_{3+}} = 1000$. The average interfacial area also seems to flatten out as the current reaches its operational value for $\frac{k^0_{4+}}{k^0_{3+}} = 1000$.

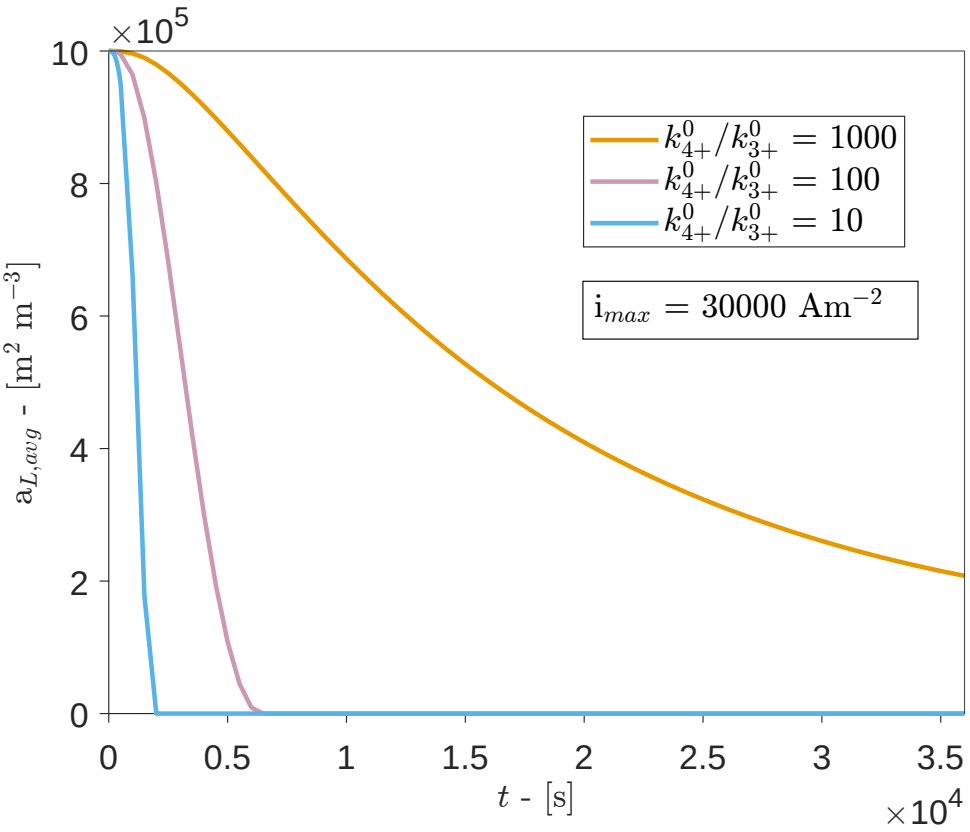

Figure 4.11: The average specific interfacial area, a_L, as a function of time, t, for three different ratios between k^0_{4+} and k^0_{3+}. The simulation was done under polarisation and the highest maximum current density of $i_\mathrm{max} = 30\,000\,\mathrm{A\,m^{-2}}$ was chosen.

It is also interesting to see how the ratio $\frac{k^0_{4+}}{k^0_{3+}}$ also affects the local degradation of the anode catalyst layer with time. While Figure 4.11, shows the effect of $\frac{k^0_{4+}}{k^0_{3+}}$ on the interfacial area as a function of time, Figure 4.12 shows how the specific interfacial area of the catalyst layer exposed to electrolyte changes with position. Figure 4.12 shows the change in a_{L} along a normalised catalyst layer for $\frac{k^0_{4+}}{k^0_{3+}} = 1000$ and $i_{\max} = 30\,000\,\mathrm{A\,m^{-2}}$. The simulation with $\frac{k^0_{4+}}{k^0_{3+}} = 1000$ and $i_{\max} = 30\,000\,\mathrm{A\,m^{-2}}$ from Figure 4.11 was chosen due to the single fact that it did not dissolve completely over the course of 36 000 s. Like previously, Figure 4.12 can be interpreted as snapshots of the catalyst layer at $t = \{600\,\mathrm{s}, 1600\,\mathrm{s}, 2600\,\mathrm{s}, 3600\,\mathrm{s}\}$.

Figure 4.12b illustrates how a_{L} changes across the anode catalytic layer exposed to the electrolyte for four different time frames. It can be seen from Figure 4.12b that the interfacial area is decreasing quite a bit as time goes and the current increases towards $i = i_{\max}$. Furthermore, it is easy to see that the interfacial area is not decaying uniformly as in Figure 4.10b, but dissolving more rapidly closer to the AEM, compared to the catalyst layer closer to the PTL, as time goes by.

The relative changes across the anode catalyst layer in Figure 4.12a is expressing the same trends as Figure 4.12b, only relative to the maximum value. From that, it is clear that there is a much larger consumption rate closer to the AEM than closer to the PTL. The relative change is also much bigger compared to the relative changes of that in 4.10a, which might come from the much larger operational current density.

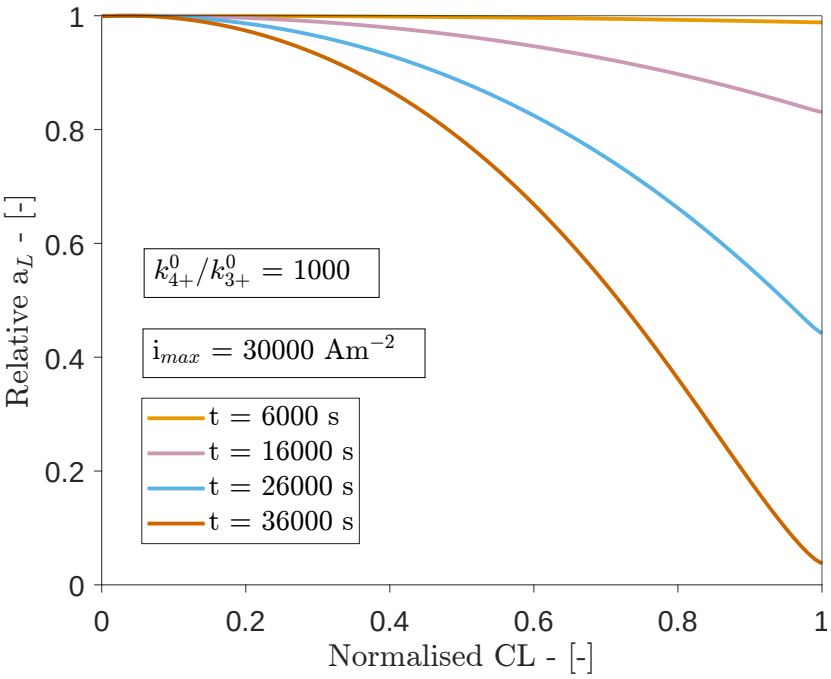

(a) Relative specific interfacial area, a_{L}, as a function of normalised catalyst layer (CL) thickness for four different time frames. The highest ratio between k^0_{4+} and k^0_{3+} from Figure 4.11 was chosen.

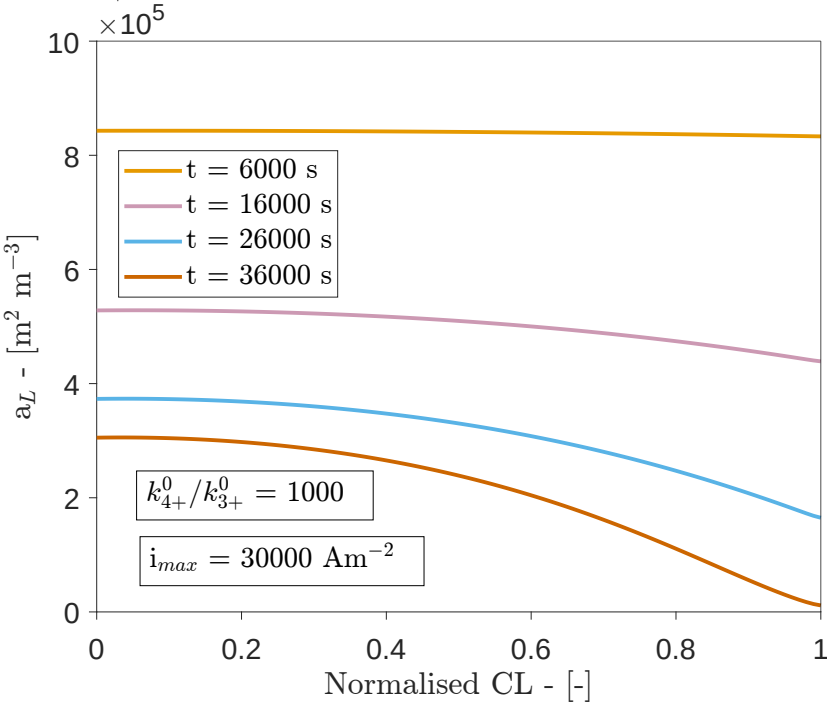

(b) Specific interfacial area, a_{L}, as a function of normalised catalyst layer (CL) thickness for four different times. The highest ratio between k^0_{4+} and k^0_{3+} from Figure 4.11 was chosen.

Figure 4.12: Regular and relative specific interfacial area, a_{L}, as a function of normalised anode catalyst layer (CL) thickness, where 0 means the interface with the PTL and 1 is the interface with the AEM, for four different time frames. The highest ratio between k^0_{4+} and k^0_{3+} from Figure 4.11 was chosen because a_{L} did not become zero.

Degradation of the catalyst layer is expressed in Equation 3.42, which is a linear function of the rate of dissolution, r_{3+}. From Equation 3.38. It is clear that r_{3+} is linearly dependent on the site coverage of IrO_3, $\Gamma\theta_2$, and is hence also related to the degradation of the catalyst layer. The conservation of the site coverage of IrO_3 was also added to the governing equations determining the AEM-WE output.

Figure 4.13 displays the average site coverage of IrO_3, $\Gamma\theta_2$, as a function of normalised catalyst thickness with $k^0_{4+} = 0.1\,\mathrm{s}^{-1}$ and $k^0_{3+} = 1.09\,\mathrm{s}^{-1}$, and with $i_{\max} = \{30\,000\,\mathrm{A\,m}^{-2}, 3000\,\mathrm{A\,m}^{-2}, 300\,\mathrm{A\,m}^{-2}, 30\,\mathrm{A\,m}^{-2}, 3\,\mathrm{A\,m}^{-2}\}$. It can be seen from Figure 4.13, that the average site coverage of IrO_3 is increasing with time/current density. Figure 4.13 is split in two because of the large differences in magnitude.

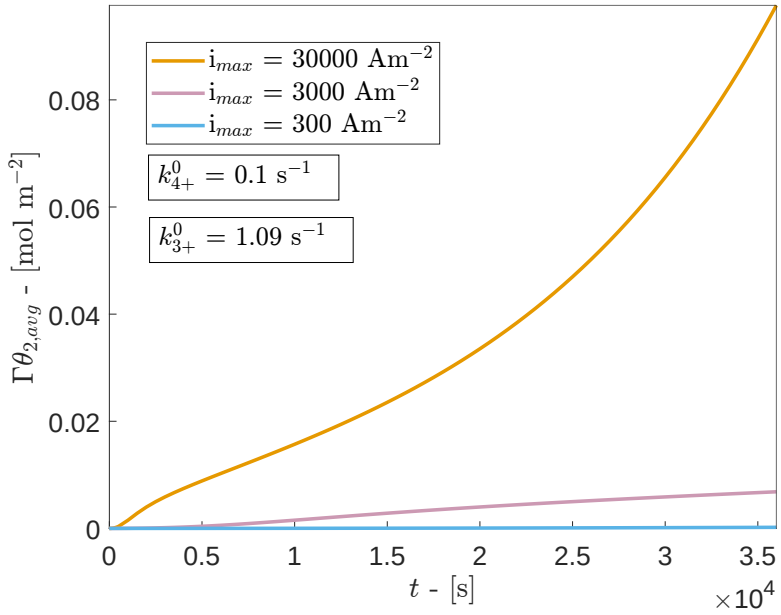

(a) The average site coverage of IrO_3 as a function of operation time for three different operational current densities. The largest rate constants from the alkaline model were used.

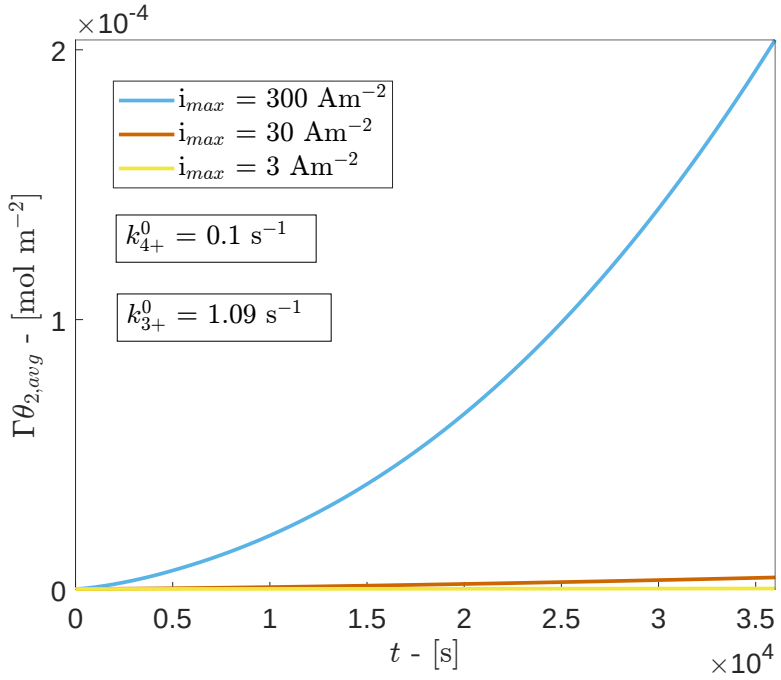

(b) The average site coverage of IrO_3 as a function of operation time for three different operational current densities. The largest rate constants from the alkaline model were used.

Figure 4.13: Average site coverage of IrO_3, $\Gamma\theta_2$, for five different current densities as a function of time, t. The simulation was done under polarisation with the maximum rate constants obtained from the alkaline model. The figure is split in two since the large difference between the currents hid the surfae coverages. Figure 4.13a shows the site coverage for $i_{\max} = \{30\,000\,\mathrm{A\,m^{-2}}, 3000\,\mathrm{A\,m^{-2}}, 300\,\mathrm{A\,m^{-2}}\}$ and Figure 4.13b shows for $i_{\max} = \{300\,\mathrm{A\,m^{-2}}, 30\,\mathrm{A\,m^{-2}}, 3\,\mathrm{A\,m^{-2}}\}$. Simulation with $i_{\max} = 300\,\mathrm{A\,m^{-2}}$ is in both figures and has the same colour.

The change in local surface concentration of IrO_3 through the anode catalyst layer is shown in 4.14. Like earlier, the site coverage of IrO_3, $\Gamma\theta_2$, is plotted against a normalised anode catalyst layer where 0 represents the interface with the PTL and 1 represents the interface with the AEM. The simulation with the maximum operating current of $i_{\max} = 3\,\mathrm{A\,m^{-2}}$ was chosen for consistency with the choice made for Figure 4.10.

Figure 4.14b illustrates the local site coverage of IrO_3 across the anode catalyst CL for $i_{\max} = 3\,\mathrm{A\,m^{-2}}$ in Figure 4.13 at $t = \{600\,\mathrm{s}, 1600\,\mathrm{s}, 2600\,\mathrm{s}, 3600\,\mathrm{s}\}$. $\Gamma\theta_2$. Figure 4.14b shows that the site coverage is steadily increasing across the whole catalyst layer as the current increases. Moreover, much like the trend in Figure 4.10b, it seems like the site coverage is the same across the whole anode catalyst layer. However, the relative changes displayed in Figure 4.10a indicate that there is a very small difference across the catalyst layer as time goes by. The largest difference between the site coverage closest to the PTL and AEM is as expected, after the longest duration of time.

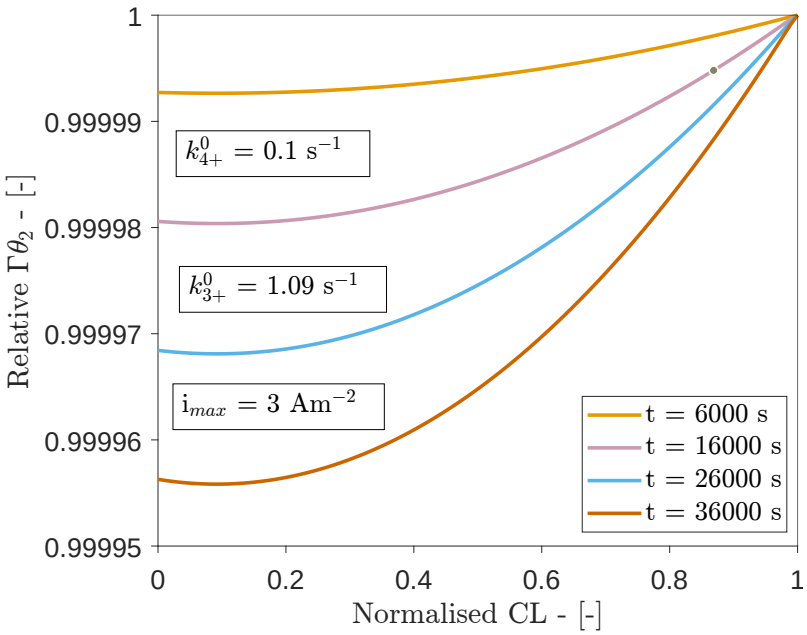

(a) Relative site coverage of IrO_3, $\Gamma\theta 2$, as a function of normalised anode catalyst layer (CL) thickness for four different times with the largest rate constants obtained from the alkaline model during a polarization with $i_{\max} = 3\,\mathrm{A\,m^{-2}}$. This current density from Figure 4.13 was chosen because of consistency.

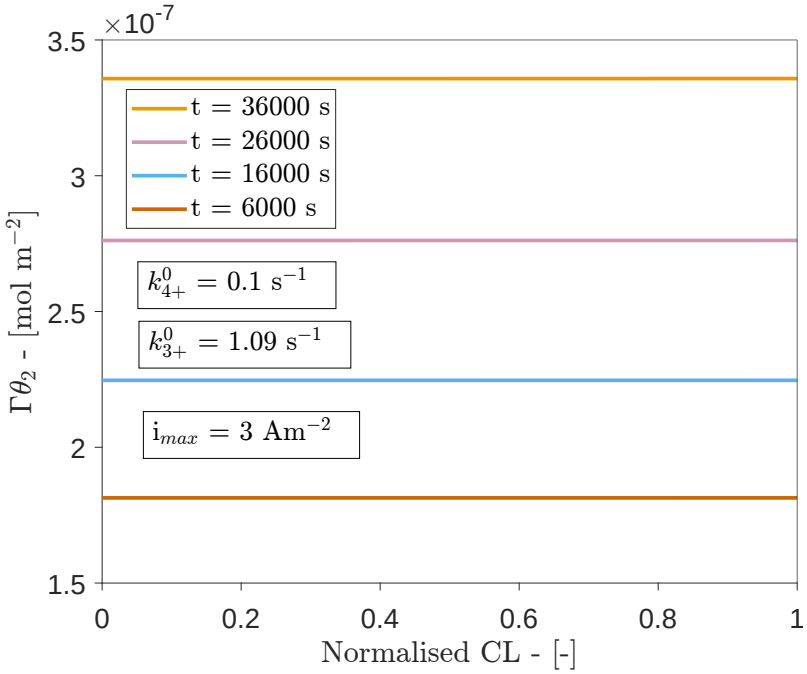

(b) Site coverage of IrO_3, $\Gamma\theta_2$, as a function of normalised catalyst layer (CL) thickness for four different times with the largest rate constants obtained from the alkaline model during a polarisation with $i_{\max} = 3\,\mathrm{A\,m^{-2}}$

Figure 4.14: Site coverage and relative site coverage of IrO_3, $\Gamma\theta_2$, as a function of normalised catalyst layer (CL) thickness, where 0 is the interface with the PTL and 1 is the interface with the AEM for four different times during a polarization with $i_{\max} = 3\,\mathrm{A\,m^{-2}}$. This current density was chosen to be consistent wit the choice of operational current density done for Figure 4.10.

The effect of the ratio $\frac{k^0_{4+}}{k^0_{3+}}$ on the site coverage of IrO_3 was also studied in the same way as for the specific interfacial area. Figure 4.15 was made by setting $i_{\max} = 30\,000\,\mathrm{A\,m^{-2}}$ and having $\frac{k^0_{4+}}{k^0_{3+}} = \{10, 100, 1000\}$. It shows how the average site coverage of IrO_3, $\Gamma\theta_2$, changes with time/current for three different ratios between the forward rate constant for oxygen formation and the forward rate constant for dissolution. The site coverage is generally higher for the lowest ratio, but the magnitude is still much lower compared to the rate constants from the alkaline model in Figure 4.13.

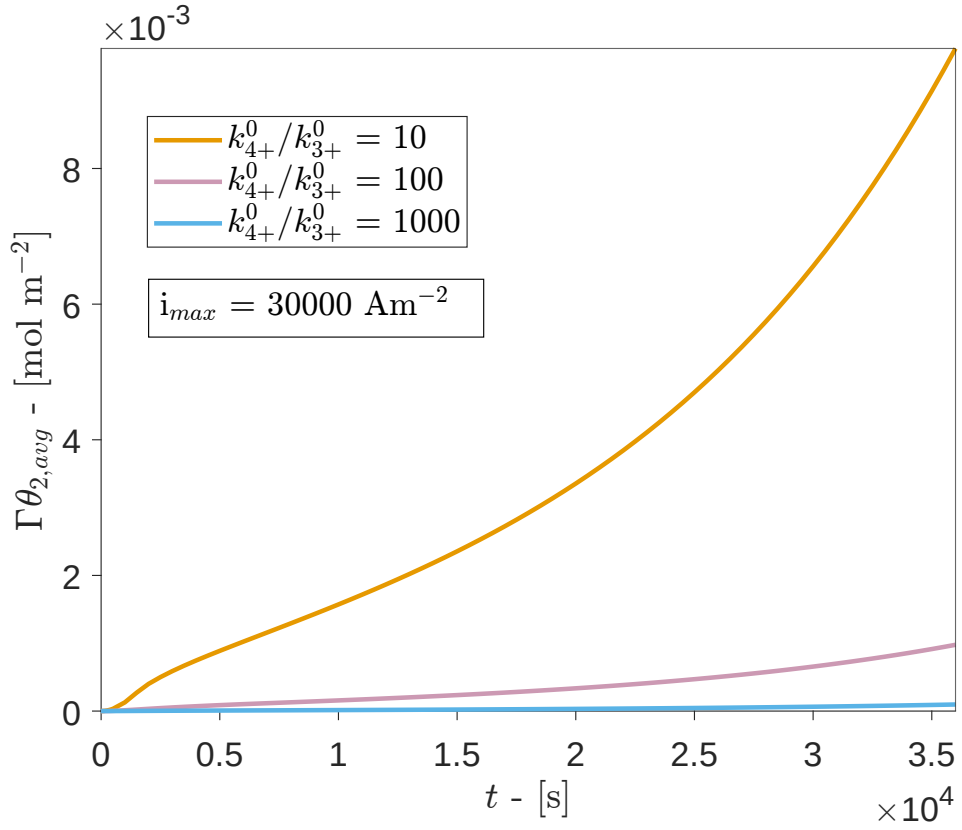

Figure 4.15: Average site coverage of IrO_3, $\Gamma\theta_2$, for three different ratios between k^0_{4+} and k^0_{3+} as a function of time, t. The simulation was done under polarisation with a maximum current of $i_{\max} = 30\,000\,\mathrm{A\,m^{-2}}$

The spatial site coverage of IrO_3 for the simulation with the highest ratio between the rate constants at $t = \{600\,\mathrm{s}, 1600\,\mathrm{s}, 2600\,\mathrm{s}, 3600\,\mathrm{s}\}$ from Figure 4.15 is shown against a normalised catalyst layer thickness in Figure 4.16. Again, 0 represents the interface with the PTL and 1 the interface with AEM. The simulation with the highest ratio was chosen to be consistent with the choice made for Figure 4.12.

The trends shown in Figure 4.16 are more profound compared to those in Figure

4.14b. It is clear that the site coverage is not increasing uniformly, but more rapidly closer to the AEM as the current density reaches maximum operational current density. The relative changes in site coverage from Figure 4.16b shows that the there is a much larger gradient in site coverage across the anode CL, than that illustrated in Figure 4.14a, with the largest difference being close to 60%.

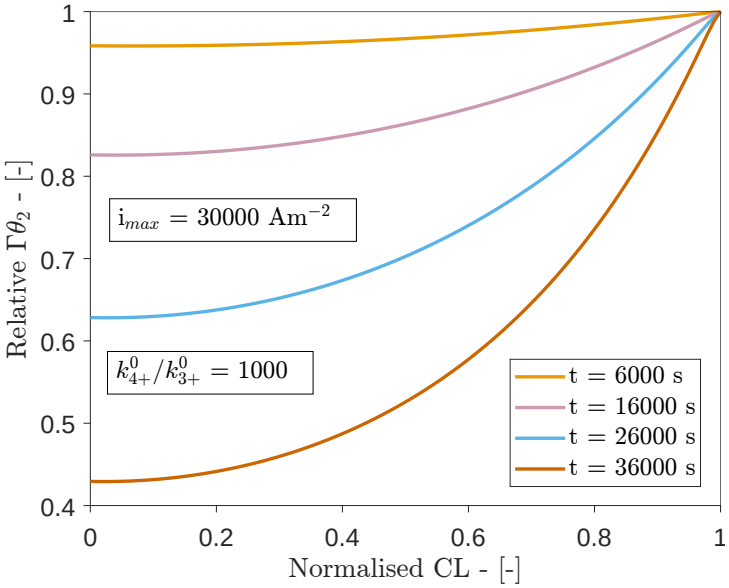

(a) Relative site coverage of IrO_3, $\Gamma\theta_2$, as a function of normalised catalyst layer (CL) thickness for four different times. The highest ratio between k^0_{4+} and k^0_{3+} from Figure 4.15 was chosen.

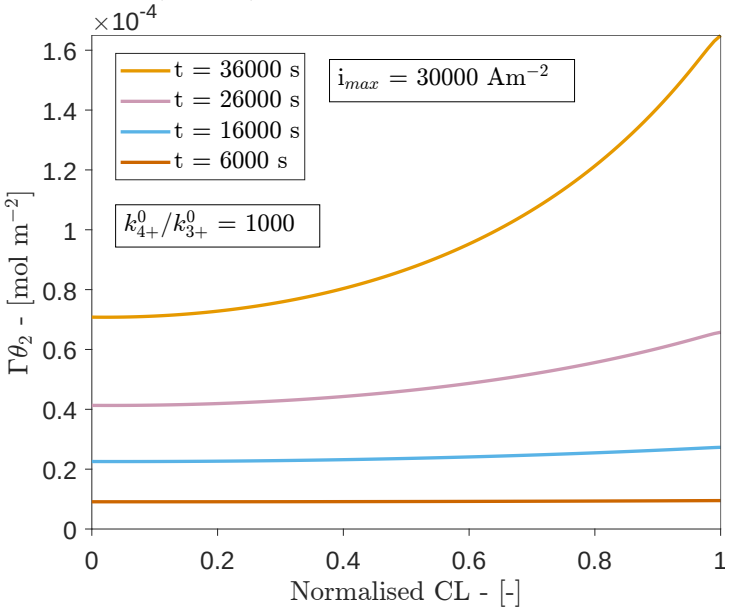

(b) Site coverage of IrO_3 as a function of normalised catalyst layer (CL) thickness for four different times. The highest ratio between k^0_{4+} and k^0_{3+} from Figure 4.15 was chosen.

Figure 4.16: Site coverage and relative site coverage of IrO_3, $\Gamma\theta_2$, as a function of a normalised anode catalyst layer (CL) thickness, where 0 means the interface with the PTL and 1 is the interface with the AEM, during a polarization with $i_{\max} = 30\,000\,\mathrm{A\,m^{-2}}$ and with the highest ratio between k^0_{4+} and k^0_{3+} from Figure 4.15. It shows the spatial site coverages for the average site coverages from Figure 4.15 for four different time frames. The highest ratio was chosen to be consistent with the choice made for Figure 4.12.

A direct measure of performance is given by polarisation curves. The effect of the

degradation of the catalyst layer on the polarisation curves is given in Figure 4.17. There is also added a simulation of an AEM-WE without the implementation of the alkaline microkinetic model for dissolution and oxygen formation. This simulation is then based on the original model described by Gerhardt *et al.*[3] and according to the description in Section 2.5. The simulation with no degradation is black in both subfigures in Figure 4.17. The effect of changing the operating current density while the values of k^0_{4+} and k^0_{3+} are kept constant are shown in Figure 4.17a, and seems like the only effect is that the potential and current is cut shorter, while it follows the same trajectory. Figure 4.17b provides a visual representation of how different ratios between k^0_{4+} and k^03+ affects the performance. The polarisation curves for the simulations with degradation are constantly a bit over the simulation of an AEM-WE with no degradation for both cases, but not by much. Simulations with no degradation were performed with the continuum model before the introduction of the microkinetic model. The fact that the two models are so close to each other in itself without having the microkinetic model explicitly tailored to fit into the cell model is surprising.

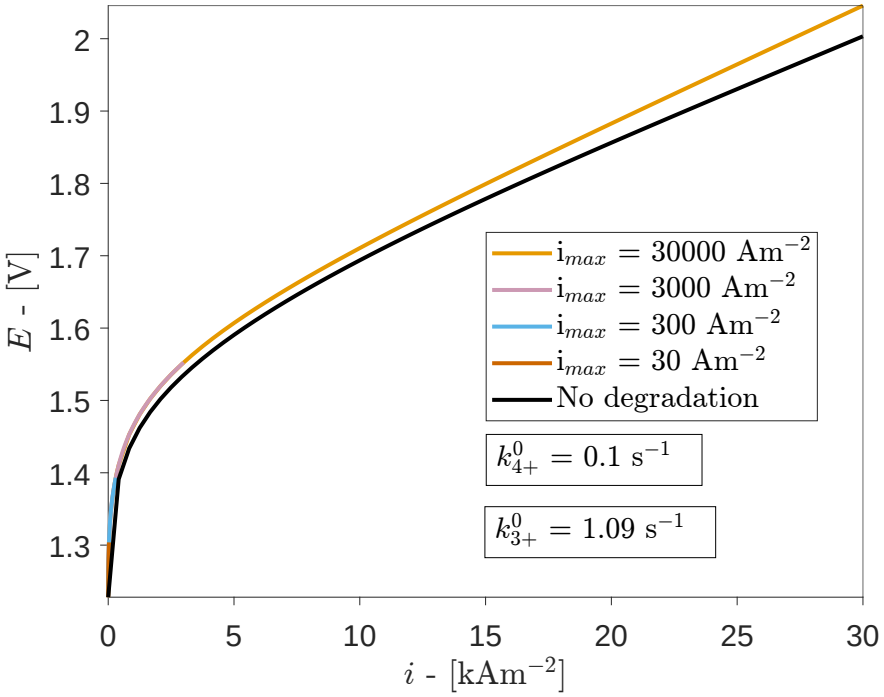

(a) Polarisation curves for four different current densities with the largest rate constants obtained from the alkaline model from Table 4.4. A polarisation curve with no degradation is added in black.

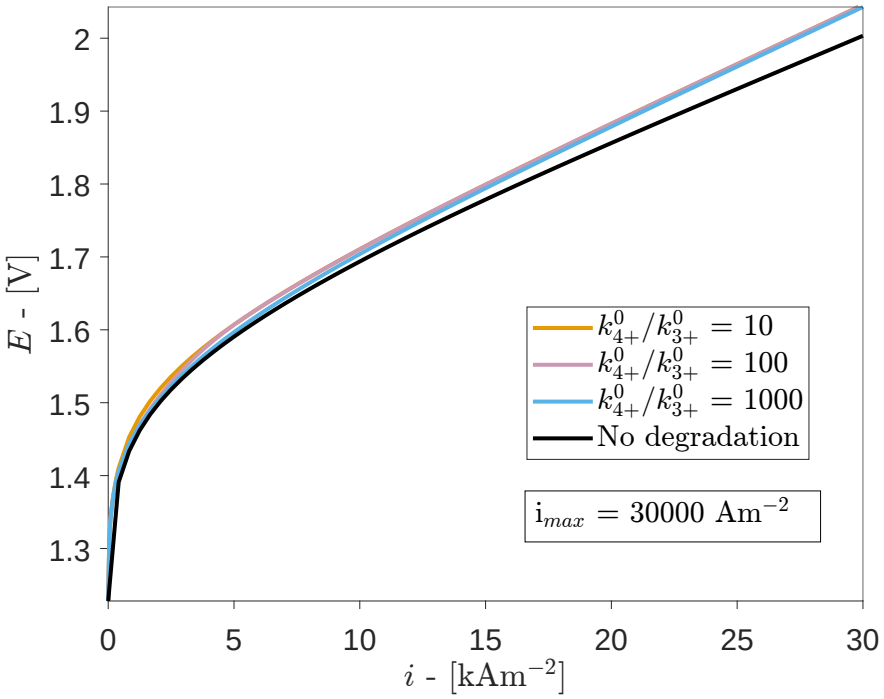

(b) Polarisation curves for three ratios of k^0_{4+} and k^0_{3+} for the same maximum current density of $I_{\max} = 30\,\mathrm{kA\,m^{-2}}$. A polarisation curve with no degradation is also added in black.

Figure 4.17: Polarisation curves showing the effect of different maximum current densities, $i_{\max}$ for $k^0_{4+} = 0.1\,\mathrm{s^{-1}}$ and $k^0_{3+} = 1.09\,\mathrm{s^{-1}}$, and the effect of the ratio between k^0_{4+} and k^0_{3+} for the same maximum current density of $i_{\max} = 30\,\mathrm{kA\,m^{-2}}$. A polarisation curve with no degradation is also added in black for comparison.

5 Discussion

The loss of catalyst covered by electrolyte leads to an offset in polarisation curves. Polarisation curves can be used to assess the performance of electrolysers where a lower cell potential for the same current indicates a better performance. From both of the obtained polarisation curves, it is clear that the performance is best with no degradation of the catalytic layer, which is no surprise. However, the relatively small offset is to some extent surprising. Even more so, when the performance for all the separate simulations with degradation is, for all practical purposes, the same, even though all the electrolyte-covered catalyst has disappeared in some cases. From the obtained interfacial area profiles, it is easy to see that the fastest decline in the catalyst layer is closest to the AEM, indicating a higher rate of degradation. Though, this effect is more profound for larger operational current densities, and is practically absent for very small current densities. The current density generated from the surface reactions on the surface covered in ionomer will contribute to the majority of the current as the electrolyte-covered catalyst diminishes. However, it is unable to completely fill the void left behind by the electrolyte-covered catalyst layer, even though it does not experience degradation. Based on the small offset in the polarisation curves, it is not unlikely that the reaction rate across the catalytic layer will even out as the catalytic layer disappears over time, to accommodate for the loss in catalyst matter.

Catalyst degradation is not uniform during the operation of an AEM-WE. For an AEM-WE under polarization, the catalyst layer will experience different demands coming from different local conditions. It is perhaps easiest to study the interfacial area profiles together with the surface coverage profiles. From the interfacial area profiles, which were just mentioned, it is clear that there is a higher demand closer to the membrane compared to the interface with the PTL. This suggests that the rate of degradation is also higher closest to the membrane. Likewise, the surface coverage of IrO_3 can also give some clues about how the degradation is spread across the catalyst layer. The removal of the interfacial surface area is described by Equation 3.42, which is a function of r_{3+}, the rate of the dissolution step, and is coupled with r_{4+}, the rate of oxygen formation step, by Equation 3.34. The rate of the dissolution step is given by Equation 3.38 and the rate of oxygen formation is given by step 3.23, and these tell us that both the rate of

dissolution and formation of oxygen is linearly dependent on the surface coverage. This means that a higher surface coverage is related to a higher rate of oxygen formation, but also a higher rate of dissolution. The surface coverage profiles imply that both reactions, dissolution and oxygen formation, have a higher occurrence closer to the AEM compared to the interface with the PTL. This coincides with information from the interfacial area profiles. In addition, these observations can also be coupled with the findings from Yu *et al.*[96] regarding catalyst diffusion in PEM-WE. They found iridium particles from the anode catalyst had dissolved and redeposited right at the interface at the membrane, but also across the membrane and all the way to the cathode. A lot of the redeposited iridium had formed an iridium band right at the interface. This is also in line with a higher reaction rate close to the membrane.

Accumulation of IrO_3 on the surface of IrO_2 enhances degradation and inhibits catalysis. The ratio between the forward rate constants for dissolution, k^0_{4+}, and oxygen formation, k^0_{3+}, tells you something about how fast IrO_3 reacts to either oxygen or dissolves into IrO_4^{2-}. A high k^0_{4+}/k^0_{3+}-ratio indicates that there is less degradation since more of the surface species is participating in the OER. A lower ratio, on the other hand, suggests more accumulation on the surface since less is transformed into oxygen, and the OER is still inherently faster than the dissolution. This is especially clear when looking at the average interfacial area as a function time for different ratios of k^0_{4+}/k^0_{3+}. It is also indicated for the average interfacial area for different currents as well. A higher current for the same ratio forces more reaction, but it also leads to more surface species, which are perhaps forming faster than they are removed. The microkinetic model also predicts the accumulation of surface coverage for lower forward rate constants for oxygen formation. The same ratios and current densities that yield a higher accumulation of IrO_3 are the same ratios and current densities that also yield the absolute fastest disintegration of the interfacial area. The electrocatalyst loses its catalytic ability since more surface species occupy active sites, without reacting further to oxygen. This can qualitatively be related to Sabatier's principles, where the surface adsorbates are bound too strongly to the surface, thus, lowering the catalysing ability of the catalyst.

The continuum model captures the main predictions from the alkaline microkinetic

model. As mentioned earlier, site coverage can to some degree be compared to reaction rate. The microkinetic model alone predicts a slow constant increase of the site coverage of IrO_3 with time as the potential steadily increases. However, the microkinetic model is also modelled to recreate degradation during a CV, while the cell model is modelled to operate during LSV. So the change in sweep directions which incites the dissolution and also spikes the surface concentration IrO_3 is not captured. Still, the surface coverage shows the expected trend by steadily increasing as a function of time and potential. The continuum model predicts the highest surface coverage at the end of the operation, which is also where the highest current and potential exist; the same as for the microkinetic model. In addition, as mentioned previously, the accumulation trends for lower values of the ratio k^0_{4+}/k^0_{3+}, are the same for the two models.

Still, there is a large discrepancy between the predictions from the alkaline model alone and the results from the continuum model with the alkaline model implemented. The alkaline model predicts a maximum dissolution rate of $r_{\text{Diss}} \approx 1.6 \cdot 10^{-8}\,\text{mol}\,\text{m}^{-2}$ at a potential $E \approx 1.5\,\text{V}$vs SHE. This would yield a time of around $32\,000\,\text{s}$ before all of a_{L} is spent with a roughness factor of 100. However, when the largest rate constant obtained from the alkaline model, given in Table 4.4, is implemented in the model, it predicts a far more rapid depletion, as can be seen in the average interfacial area as a function of time with the alkaline model parameters implemented. By looking at the polarisation curves, a cell potential of $E_{\text{Cell}} \approx 1.5\,\text{V}$ would correspond to a current density of $2\,\text{kA}\,\text{m}^{-2}$. It is not before the operation current is as low as $3\,\text{A}\,\text{m}^{-2}$, that the catalyst layer survives the whole polarisation. The discrepancy might be explained by the difference in complexity. SINTEFs model is simulating an AEM-WE under polarisation with an initial concentration of KOH of $1\,\text{mol}\,\text{L}^{-1}$, which is far more concentrated than $0.05\,\text{mol}\,\text{L}^{-1}$ which was used in the alkaline model to estimate the rate constant. From Equation 3.38, it can be seen that the reaction order for OH^- for the dissolution current is $\Omega_{OH^-} = 2$, which means that a concentration of $1\,\text{mol}\,\text{L}^{-1}$ KOH as a huge effect on the dissolution rate. Moreover, the Pourbaix diagram, Figure 2.2, predicts that the most stable form of iridium at this pH and operating potential is the dissolution product. So a more rapid dissolution of IrO_2 in alkaline solutions, compared to acidic is expected. In the derivation of the microkinetic model, transport limitations are neglected. This might be a valid assumption for small

current densities, potentials, and diluted solutions, but it oversimplifies the system when implemented in the full-cell model. There are indeed transport limitations within the model, especially at the large current densities, which also come into play. Following this further, the dissolution rate obtained in the alkaline model in Section 4 was based on degradation data from Schalenbach *et al.* [2], which was measured for very small current densities, less than $i = 15\,\mathrm{A\,m^{-2}}$ and within $0.04\,\mathrm{V vs\ RHE} < E < 1.5\,\mathrm{V vs\ RHE}$. There is no guarantee that the derived dissolution is valid for current densities and operating potentials of the magnitude the AEM-WE operates. Looking at the polarisation curves, the potential is around 2 V, which is a lot more than 1.5 V, and the corresponding current density reaches $30\,\mathrm{kA\,m^{-2}}$. This implies a small gap within operational parameters where the microkinetic model is valid. This could perhaps have been avoided if a full dynamic analysis of the system was undertaken and successful, such that different Tafel behaviour could indeed be captured across these large spans in potential. Lastly, the way degradation is modelled as described in Section 3 is based on a totally different surface than that the degradation is actually measured.

The site coverage can describe the validity of the microkinetic model. $\Gamma\theta_2$ as a function of time with the potential regime for both the acidic and alkaline model, reveals two completely different magnitudes where the acidic site coverage is in the order of $10^{-2}\ \mathrm{mol\,m^{-2}}$, while the alkaline is within the order of $10^{-5}\ \mathrm{mol\,m^{-2}}$. The large span in surface coverage may be caused by the difference in activity and stability between the polarisation curves related to the microkinetic model. The intrinsic concentration of available active sites, Γ, is difficult to predict for oxide layers that are not monocrystalline. Though Geppert et al [36] reports that the value of active available sites for the (110) plane for rutile iridium oxide from density functional theory (DFT) is $\Gamma_{\mathrm{IrO_2}} = 8.3 \cdot 10^{-6}\ \mathrm{mol\,m^{-2}}$, but they also mention that the value for hydrous iridium oxide can be two orders of magnitude larger, which might be caused by the roughness of the hydrous layer. Still, this makes the fractional surface coverage of IrO_3 for the acidic model based on the dissolution study of Mayrhofer et al [1] to be $\theta_2 \approx 60$, with a roughness factor of 100. This is a bit high considering the fractional coverage should, by definition, be $0 < \theta_2 \leq 1$. Since the roughness is not measured by Marhofer et al[1], it might be even higher. The alkaline surface coverage in Figure 4.6, is a completely different story. Schalenbach et al [2] is measuring dissolution on metallic iridium, but the

major parts of the degradation is occurring after the onset potential of formation of an oxide layer. This means that the possibility of dissolution occurring from an oxide layer instead of the intended metallic surface can not be ruled out. It also means that the dissolution mechanism is most likely not described by the assumed mechanism of Kasian et al [25], and hence not captured properly by the alkaline model. By using the same intrinsic value for the concentration of active sites as for the (110) plane of IrO_2 the fractional coverage of IrO_3 for the alkaline model becomes $\theta_2 \approx 1.2$, which is not unreasonable at all, and well within the bounds of uncertainty.

The results from microkinetic models are heavily influenced by the chosen mechanism [36, 29]. One of the key steps in devising such a model is to pick or describe a mechanism which is either supported by experimental observations or based on theoretical aspects like DFT calculations[88, 86]. So even though the intermediates IrO_3 and IrO_2OH are found experimentally, it is also found that the LOER mechanism described in Section 2 can be substantial or even dominating under certain conditions. The presence of LOER, however, does not exclude the presence of other surface mechanisms, meaning that the OER occurring on the metallic iridium in Schalenbach et al[2] degradation study, might be a combination of the two, or none of them. This is perhaps the reason why the predicted models have a harder time fitting to the degradation data from the alkaline model as illustrated in Figure 4.8, compared to that of the acidic model in Figure 4.4. Furthermore, as mentioned in the last paragraph, the modelled mechanism is meant to fit a surface which starts out as a metallic surface, and then an oxide layer is formed during polarization. The oxygen in the oxide layer is prone to dissolution since it will always experience a change in oxidation state during polarization, which is one of the reasons oxides are thermodynamically unstable under OER[32]. This will then have the oxygen atoms participate more in surface reactions, which consist of OER and different dissolution reactions among others. However, this is not encapsulated in the assumed mechanism.

6 Conclusions

Microkinetic modelling was applied to describe the degradation of IrO_2 during OER in both alkaline and acidic environments based on degradation measurements from Mayrhofer *et al.*[1] and Schalenbach *et al.*[2]. The alkaline model was then implemented in a continuum model simulating the operation of an anion-exchange membrane water electrolyser to describe the degradation of the catalyst layer. The polarisation curves in Figure 4.17 from the simulations indicate that the dissolution of the catalyst layer described by the model has a relatively small effect on the performance. This indicates that the catalyst covered by ionomer provides most of the current, which was assumed not to degrade. This applies regardless of the ratio between the rate constant for oxygen formation and the rate constant for dissolution, $\frac{k^0_{4+}}{k^0_{3+}}$. However, from the specific interfacial area profiles in Figure 4.12 and 4.10, it is clear that the dissolution rates are not uniform across the catalyst layer, especially at higher current densities. There is indeed a higher rate of dissolution on the catalyst closer to the CL/AEM interface, compared to that of the PTL/CL interface. This is also coherent with the site coverage illustrated in Figure 4.16 and 4.14. From the surface coverage, one can also conclude that the higher surface coverage is also related to a higher rate of oxygen formation, and also followed by a higher rate of dissolution. This is consistent with the catalyst trade-off between stability and activity from Danilovic *et al.*[82]. This distribution of reaction rates is more pronounced at higher current densities. The continuum model is predicting the same trends to some degree regarding the dissolution as a function of current/time, but there is also a lot of discrepancy between the microkinetic model alone and that of the continuum model. This is perhaps originating from the use of quasi-steady-state assumptions in the derivation of the microkinetic model of dissolution. There is also a large potential range where the microkinetic model might be invalid because of the higher potentials from the operation of the continuum model compared to the potential where the dissolution was measured. The alkaline microkinetic model stems from the degradation of Ir/IrO_2 in alkaline solution from Schalenbach *et al.*[2]. They did, however, start with metallic iridium, and an oxide layer was formed during the dissolution. This may have affected their data, such that there indeed were several dissolution mechanisms dominating throughout the CV used to measure dissolution. This leads to the question if the assumed mechanism even was applicable to these data. The

acidic model on the other hand seemed to capture the dissolution trends quite well, compared to the alkaline model.

7 Further work

The microkinetic model introduced in Section 3.3 was based on quasi-steady-state assumptions by assuming the step where the formation of IrO_3 was rate determining, reaction 3.2 and 3.15. Such an assumption was perhaps valid in elucidating the microkinetic model based on the degradation data from Mayrhofer *et al.* [1] and Schalenbach *et al.* [2] since the maximum potential was $E = 1.6\,\mathrm{V}$vs RHE for acidic and $E = 1.5\,\mathrm{V}$vs RHE for the alkaline model, and in estimating the unknown kinetic parameters with LSV data. However, as Geppert *et al.*[28] points out, such assumptions might hide different tafel behaviours across large spans in current density and potential, as was the case of AEM-WE from the continuum model, where the potential for an operating AEM-WE could end up being in the range of $E_{\mathrm{Cell}} \approx 2\,\mathrm{V}$. In addition, which step is rds can change depending on the potential. This means that the initial assumption of a quasi-steady-state might have led to a too simple microkinetic model, for such a dynamic system that is modelled in the continuum model. As a result, the implemented degradation would perhaps not capture an accurate picture of the dissolution of the anode catalytic layer for higher currents and potentials. In order to capture such properties, more resources should be spent on a full-rate analysis, to ensure that the implemented model would be valid over the span of the operational potential. Much inspired by the work of Reksten [94], Marshall *et al.* [28], and Geppert *et al.*[36].

Because of time constraints related to the modelling, the continuum model only simulated an AEM-WE under polarisation conditions. The microkinetic model was based on more dynamic measurements like cyclic voltammetry. It would be interesting to see how the continuum model would respond to exposure of CV measurements and see if the results from the AEM-WE model would predict the same properties as the microkinetic model. Lastly, doing simulations with the constant current would perhaps give a more nuanced picture of the degradation of iridium oxide. Comparing how $\Gamma\theta_2$ and a_{L} would be affected by different forms of operation would indeed be interesting.

A big aspect of microkinetic modelling is assuming that the reaction mechanism is occurring on the surface, and hence, the surface processes play a huge role. The way adsorbates interact with each other and the surface was outside of the scope and implicitly assumed ideal. Geppert *et al.*[36]also introduced adsorption

functions which would account for non-ideality in the adsorption processes. It would be interesting to include this aspect and see if the use of isotherms for adsorption processes would yield even more accurate results.

The OER mechanism in general is highly debated, and a lot is unknown. Only one part of the OER mechanism proposed by Kasian *et al.* [25] was studied. Though, as the results and degradation curves indicate, this mechanism might not alone capture the most correct image, especially in an alkaline environment. It would therefore be worth not only expanding the proposed mechanism by Kasian, but also comparing simulations based on two different mechanisms and see how the output each mechanism changes behaviour if the simulated AEM-WE.

References

[1] S. Cherevko, S. Geiger, O. Kasian, A. Mingers, and K. J. Mayrhofer, "Oxygen evolution activity and stability of iridium in acidic media. Part 2. - Electrochemically grown hydrous iridium oxide," *Journal of Electroanalytical Chemistry*, vol. 774, pp. 102–110, 8 2016.

[2] M. Schalenbach, O. Kasian, M. Ledendecker, F. D. Speck, A. M. Mingers, K. J. Mayrhofer, and S. Cherevko, "The Electrochemical Dissolution of Noble Metals in Alkaline Media," *Electrocatalysis*, vol. 9, pp. 153–161, 3 2018.

[3] M. R. Gerhardt, A. O. Barnett, T. Khoza, P. Fortin, S. Andrenacci, A. Y. Faid, S. Sunde, S. Clark, and P. E. England Karstensen, "An open-source continuum model for hydrogen production from anion-exchange membrane water electrolysis," 2023.

[4] UN authors, "Goal 13: Take urgent action to combat climate change and its impacts," 2023.

[5] P. P. Edwards, V. L. Kuznetsov, W. I. David, and N. P. Brandon, "Hydrogen and fuel cells: Towards a sustainable energy future," *Energy Policy*, vol. 36, pp. 4356–4362, 12 2008.

[6] UNFCCC, "The Paris Agreement," 2023.

[7] UNFCCC, "What is the Kyoto Protocol," 2023.

[8] UNFCCC, "The Glasgow Climate Pact – Key Outcomes from COP26," 2023.

[9] I. Vincent and D. Bessarabov, "Low cost hydrogen production by anion exchange membrane electrolysis: A review," 6 2018.

[10] M. Yu, K. Wang, and H. Vredenburg, "Insights into low-carbon hydrogen production methods: Green, blue and aqua hydrogen," *International Journal of Hydrogen Energy*, vol. 46, no. 41, pp. 21261–21273, 2021.

[11] G. P. Dinga, "HYDROGEN: THE ULTIMATE FUEL AND ENERGY CARRIER*," *Int. J. Hydrogen Energy*, vol. 14, no. 11, pp. 777–784, 1989.

[12] S. A. Lee, J. Kim, K. C. Kwon, S. H. Park, and H. W. Jang, "Anion ex-

change membrane water electrolysis for sustainable large-scale hydrogen production," *Carbon Neutralization*, vol. 1, pp. 26–48, 5 2022.

[13] P. Millet, F. Andolfatto, and R. Durand, "DESIGN AND PERFORMANCE OF A SOLID POLYMER ELECTROLYTE WATER ELECTROLYZER," *INTERNATIONAL JOURNAL OF HYDROGEN ENERGY*, vol. 21, pp. 87–93, 1 1996.

[14] K. Ayers, N. Danilovic, R. Ouimet, M. Carmo, B. Pivovar, and M. Bornstein, "Perspectives on Low-Temperature Electrolysis and Potential for Renewable Hydrogen at Scale.," *Annual review of chemical and biomolecular engineering*, 6 2019.

[15] A. Y. Faid and S. Sunde, "Anion Exchange Membrane Water Electrolysis from Catalyst Design to the Membrane Electrode Assembly," 9 2022.

[16] L. An, T. S. Zhao, Z. H. Chai, P. Tan, and L. Zeng, "Mathematical modeling of an anion-exchange membrane water electrolyzer for hydrogen production," *International Journal of Hydrogen Energy*, vol. 39, pp. 19869–19876, 12 2014.

[17] C. Santoro, A. Lavacchi, P. Mustarelli, V. Di Noto, L. Elbaz, D. R. Dekel, and F. Jaouen, "What is Next in Anion-Exchange Membrane Water Electrolyzers? Bottlenecks, Benefits, and Future," 4 2022.

[18] D. Li, E. J. Park, W. Zhu, Q. Shi, Y. Zhou, H. Tian, Y. Lin, A. Serov, B. Zulevi, E. D. Baca, C. Fujimoto, H. T. Chung, and Y. S. Kim, "Highly quaternized polystyrene ionomers for high performance anion exchange membrane water electrolysers," *Nature Energy*, vol. 5, pp. 378–385, 5 2020.

[19] K. Lee, R. A. Flores, Y. Liu, B. Y. Wang, Y. Hikita, R. Sinclair, M. Bajdich, and H. Y. Hwang, "Epitaxial Stabilization and Oxygen Evolution Reaction Activity of Metastable Columbite Iridium Oxide," *ACS Applied Energy Materials*, vol. 4, pp. 3074–3082, 4 2021.

[20] G. Buvat, M. J. Eslamibidgoli, T. Zhang, S. Prabhudev, A. H. Youssef, A. Ruediger, S. Garbarino, G. A. Botton, P. Zhang, M. Eikerling, and D. Guay, "Understanding the Effect of Ni-Substitution on the Oxygen Evo-

lution Reaction of (100) IrO2 Surfaces," *ACS Catalysis*, vol. 12, pp. 10961–10972, 9 2022.

[21] L. Giordano, B. Han, M. Risch, W. T. Hong, R. R. Rao, K. A. Stoerzinger, and Y. Shao-Horn, "PH dependence of OER activity of oxides: Current and future perspectives," 3 2016.

[22] H. G. Sanchez, M. L. Ng, S. Kaya, D. Friebel, H. Ogasawara, and A. Nilsson, "In-Situ observation of surface species on iridium oxide nanoparticles during the oxygen evolution reaction," *Angewandte Chemie - International Edition*, vol. 53, pp. 7169–7172, 7 2014.

[23] T. Naito, T. Shinagawa, T. Nishimoto, and K. Takanabe, "Recent advances in understanding oxygen evolution reaction mechanisms over iridium oxide," 6 2021.

[24] M. Scohy, C. Montella, F. Claudel, S. Abbou, L. Dubau, F. Maillard, E. Sibert, and S. Sunde, "Investigating the oxygen evolution reaction on Ir(111) electrode in acidic medium using conventional and dynamic electrochemical impedance spectroscopy," *Electrochimica Acta*, vol. 320, 10 2019.

[25] O. Kasian, J.-P. Grote, S. Geiger, S. Cherevko, and K. J. J. Mayrhofer, "Die gemeinsamen Zwischenprodukte von Sauerstoffentwicklung und Auflösung während der Wasserelektrolyse an Iridium," *Angewandte Chemie*, vol. 130, pp. 2514–2517, 2 2018.

[26] I. C. Man, H. Y. Su, F. Calle-Vallejo, H. A. Hansen, J. I. Martínez, N. G. Inoglu, J. Kitchin, T. F. Jaramillo, J. K. Nørskov, and J. Rossmeisl, "Universality in Oxygen Evolution Electrocatalysis on Oxide Surfaces," *ChemCatChem*, vol. 3, pp. 1159–1165, 7 2011.

[27] S. Cherevko, A. R. Zeradjanin, A. A. Topalov, N. Kulyk, I. Katsounaros, and K. J. Mayrhofer, "Dissolution of noble metals during oxygen evolution in acidic media," *ChemCatChem*, vol. 6, no. 8, pp. 2219–2223, 2014.

[28] A. T. Marshall and L. Vaisson-Béthune, "Avoid the quasi-equilibrium assumption when evaluating the electrocatalytic oxygen evolution reaction

mechanism by Tafel slope analysis," *Electrochemistry Communications*, vol. 61, pp. 23–26, 9 2015.

[29] A. P. Dam, G. Papakonstantinou, and K. Sundmacher, "On the role of microkinetic network structure in the interplay between oxygen evolution reaction and catalyst dissolution," *Scientific Reports*, vol. 10, 12 2020.

[30] S. Cherevko, S. Geiger, O. Kasian, A. Mingers, and K. J. Mayrhofer, "Oxygen evolution activity and stability of iridium in acidic media. Part 1. - Metallic iridium," *Journal of Electroanalytical Chemistry*, vol. 773, pp. 69–78, 7 2016.

[31] O. Kasian, S. Geiger, T. Li, J. P. Grote, K. Schweinar, S. Zhang, C. Scheu, D. Raabe, S. Cherevko, B. Gault, and K. J. Mayrhofer, "Degradation of iridium oxides via oxygen evolution from the lattice: Correlating atomic scale structure with reaction mechanisms," *Energy and Environmental Science*, vol. 12, pp. 3548–3555, 12 2019.

[32] T. Binninger, R. Mohamed, K. Waltar, E. Fabbri, P. Levecque, R. Kötz, and T. J. Schmidt, "Thermodynamic explanation of the universal correlation between oxygen evolution activity and corrosion of oxide catalysts," *Scientific Reports*, vol. 5, 7 2015.

[33] J. Liu, Z. Kang, D. Li, M. Pak, S. M. Alia, C. Fujimoto, G. Bender, Y. S. Kim, and A. Z. Weber, "Elucidating the Role of Hydroxide Electrolyte on Anion-Exchange-Membrane Water Electrolyzer Performance," *Journal of The Electrochemical Society*, vol. 168, 5 2021.

[34] D. Saebea, C. Chaiburi, and S. Authayanun, "Model based evaluation of alkaline anion exchange membrane fuel cells with water management," *Chemical Engineering Journal*, vol. 374, pp. 721–729, 10 2019.

[35] J. Geppert, P. Röse, S. Czioska, D. Escalera-López, A. Boubnov, E. Saraçi, S. Cherevko, J.-D. Grunwaldt, and U. Krewer, "Microkinetic Analysis of the Oxygen Evolution Performance at Different Stages of Iridium Oxide Degradation," *Journal of the American Chemical Society*, vol. 144, no. 29, pp. 13205–13217, 2022.

[36] J. Geppert, F. Kubannek, P. Röse, and U. Krewer, "Identifying the oxygen evolution mechanism by microkinetic modelling of cyclic voltammograms," *Electrochimica Acta*, vol. 380, 6 2021.

[37] A. H. Reksten, H. Thuv, F. Seland, and S. Sunde, "The oxygen evolution reaction mechanism at IrxRu1-xO2 powders produced by hydrolysis synthesis," *Journal of Electroanalytical Chemistry*, vol. 819, pp. 547–561, 6 2018.

[38] M. Carmo, D. L. Fritz, J. Mergel, and D. Stolten, "A comprehensive review on PEM water electrolysis," 4 2013.

[39] A. L. Santos, M. J. Cebola, and D. M. Santos, "Towards the hydrogen economy—a review of the parameters that influence the efficiency of alkaline water electrolyzers," *Energies*, vol. 14, 6 2021.

[40] H. Ito, N. Kawaguchi, S. Someya, T. Munakata, N. Miyazaki, M. Ishida, and A. Nakano, "Experimental investigation of electrolytic solution for anion exchange membrane water electrolysis," *International Journal of Hydrogen Energy*, vol. 43, pp. 17030–17039, 9 2018.

[41] A. D. Igalavithana, S. You, L. Zhang, J. Shang, J. Lehmann, X. Wang, Y.-G. Zhu, D. C. W. Tsang, Y.-K. Park, D. Hou, and Y. S. Ok, "Progress, Barriers, and Prospects for Achieving a "Hydrogen Society" and Opportunities for Biochar Technology," *ACS ES&T ENGINEERING*, pp. 1987–2001, 10 2022.

[42] N. Du, C. Roy, R. Peach, M. Turnbull, S. Thiele, and C. Bock, "Anion-Exchange Membrane Water Electrolyzers," 7 2022.

[43] A. Blackman, *Aylward and Findlay's SI Chemical Data*. Milton: John Wiley & Sons, 7th ed. ed., 2014.

[44] C. Hamann, A. Hamnett, and W. Vielstich, *Electrochemistry*. Weinheim: Wiley, 2nd edition ed., 2007.

[45] J. J. Kaczur, H. Yang, Z. Liu, S. D. Sajjad, and R. I. Masel, "Carbon Dioxide and Water Electrolysis Using New Alkaline Stable Anion Membranes," *Frontiers in Chemistry*, vol. 6, 2018.

[46] D. Li, A. R. Motz, C. Bae, C. Fujimoto, G. Yang, F.-Y. Zhang, K. E. Ayers,

and Y. S. Kim, "Durability of anion exchange membrane water electrolyzers," *Energy Environ. Sci.*, vol. 14, no. 6, pp. 3393–3419, 2021.

[47] J. R. Varcoe, P. Atanassov, D. R. Dekel, A. M. Herring, M. A. Hickner, P. A. Kohl, A. R. Kucernak, W. E. Mustain, K. Nijmeijer, K. Scott, T. Xu, and L. Zhuang, "Anion-exchange membranes in electrochemical energy systems," 10 2014.

[48] K. Artyushkova, A. Serov, H. Doan, N. Danilovic, C. B. Capuano, T. Sakamoto, H. Kishi, S. Yamaguchi, S. Mukerjee, and P. Atanassov, "Application of X-ray photoelectron spectroscopy to studies of electrodes in fuel cells and electrolyzers," *Journal of Electron Spectroscopy and Related Phenomena*, vol. 231, pp. 127–139, 2019.

[49] F. D. Speck, A. Zagalskaya, V. Alexandrov, and S. Cherevko, "Periodicity in the Electrochemical Dissolution of Transition Metals," *Angewandte Chemie - International Edition*, vol. 60, pp. 13343–13349, 6 2021.

[50] S. Cherevko, S. Geiger, O. Kasian, N. Kulyk, J. P. Grote, A. Savan, B. R. Shrestha, S. Merzlikin, B. Breitbach, A. Ludwig, and K. J. Mayrhofer, "Oxygen and hydrogen evolution reactions on Ru, RuO2, Ir, and IrO2 thin film electrodes in acidic and alkaline electrolytes: A comparative study on activity and stability," *Catalysis Today*, vol. 262, pp. 170–180, 3 2016.

[51] S. Fierro, T. Nagel, H. Baltruschat, and C. Comninellis, "Investigation of the oxygen evolution reaction on Ti/IrO2 electrodes using isotope labelling and on-line mass spectrometry," *Electrochemistry Communications*, vol. 9, pp. 1969–1974, 8 2007.

[52] J. S. Newman and K. E. Thomas-Aylea, *Electrochemical systems.* Hoboken, N.J: Wiley, 3rd ed. ed., 2004.

[53] K. Oldham, J. Myland, and A. Bond, *Electrochemical science and technology: fundamentals and applications.* Hoboken: Wiley, 2011.

[54] G. Rothenberg, "Catalysis : concepts and green applications," 2008.

[55] K. A. Stoerzinger, L. Qiao, M. D. Biegalski, and Y. Shao-Horn, "Orientation-

Dependent Oxygen Evolution Activities of Rutile IrO2 and RuO2," *The Journal of Physical Chemistry Letters*, vol. 5, no. 10, pp. 1636–1641, 2014.

[56] H. Ooka, J. Huang, and K. S. Exner, "The Sabatier Principle in Electrocatalysis: Basics, Limitations, and Extensions," *Frontiers In Energy Research*, vol. 9, 5 2021.

[57] S. Trasatti, "Electrocatalysis by oxides — Attempt at a unifying approach," *Journal of Electroanalytical Chemistry and Interfacial Electrochemistry*, vol. 111, no. 1, pp. 125–131, 1980.

[58] P. Sabatier, *La catalyse en chimie organique*, vol. 3. C. Béranger, 1920.

[59] J. O. Bockris, "Kinetics of Activation Controlled Consecutive Electrochemical Reactions: Anodic Evolution of Oxygen," *Journal Of Chemical Physics*, vol. 24, no. 4, pp. 817–827, 1956.

[60] X. Wang, H. Zhong, S. Xi, W. S. V. Lee, and J. Xue, "Understanding of Oxygen Redox in the Oxygen Evolution Reaction," *Advanced Materials*, vol. 34, no. 50, pp. 1–27, 2022.

[61] X. Rong, J. Parolin, and A. M. Kolpak, "A Fundamental Relationship between Reaction Mechanism and Stability in Metal Oxide Catalysts for Oxygen Evolution," *ACS Catalysis*, vol. 6, pp. 1153–1158, 2 2016.

[62] M. Wohlfahrt-Mehrens and J. Heitbaum, "OXYGEN EVOLUTION ON Ru AND RuO2, ELECTRODES STUDIED USING ISOTOPE LABELLING AND ON-LINE MASS SPECTROMETRY," tech. rep., Institute of Physical Chemistry, Luasanne, 6 1987.

[63] O. Kasian, J.-P. Grote, S. Geiger, S. Cherevko, and K. J. J. Mayrhofer, "Supporting Information The Common Intermediates of Oxygen Evolution and Dissolution Reactions during Water Electrolysis on Iridium," 2018.

[64] S. Geiger, O. Kasian, M. Ledendecker, E. Pizzutilo, A. M. Mingers, W. T. Fu, Z. Diaz-Morales Oscarand Li, T. Oellers, L. Fruchter, A. Ludwig, K. J. J. Mayrhofer, M. T. M. Koper, and S. Cherevko, "The stability number as a metric for electrocatalyst stability benchmarking," *NATURE CATALYSIS*, vol. 1, pp. 508–515, 7 2018.

[65] A. G. Martínez, P. C. Gómez, S. de la Moya, and H.-U. Siehl, "Revealing the mechanism of the water autoprotolysis on the basis of Marcus theory and TD-DFT methodology," *Journal of Molecular Liquids*, vol. 324, p. 115092, 2021.

[66] M. Pourbaix, *Atlas of electrochemical equilibria in aqueous solutions*. Oxford: Pergamon Press, 1966.

[67] A. Jain, G. Hautier, S. P. Ong, C. J. Moore, C. C. Fischer, K. A. Persson, and G. Ceder, "Formation enthalpies by mixing GGA and GGA + U calculations," *Phys. Rev. B*, vol. 84, p. 45115, 7 2011.

[68] K. A. Persson, B. Waldwick, P. Lazic, and G. Ceder, "Prediction of solid-aqueous equilibria: Scheme to combine first-principles calculations of solids with experimental aqueous states," *Phys. Rev. B*, vol. 85, p. 235438, 6 2012.

[69] I. Petousis, D. Mrdjenovich, E. Ballouz, M. Liu, D. Winston, W. Chen, T. Graf, T. D. Schladt, K. A. Persson, and F. B. Prinz, "High-throughput screening of inorganic compounds for the discovery of novel dielectric and optical materials," *Scientific Data*, vol. 4, no. 1, p. 160134, 2017.

[70] M. K. Horton, J. H. Montoya, M. Liu, and K. A. Persson, "High-throughput prediction of the ground-state collinear magnetic order of inorganic materials using Density Functional Theory," *npj Computational Materials*, vol. 5, no. 1, p. 64, 2019.

[71] M. de Jong, W. Chen, T. Angsten, A. Jain, R. Notestine, A. Gamst, M. Sluiter, C. Krishna Ande, S. van der Zwaag, J. J. Plata, C. Toher, S. Curtarolo, G. Ceder, K. A. Persson, and M. Asta, "Charting the complete elastic properties of inorganic crystalline compounds," *Scientific Data*, vol. 2, no. 1, p. 150009, 2015.

[72] M. de Jong, W. Chen, H. Geerlings, M. Asta, and K. A. Persson, "A database to enable discovery and design of piezoelectric materials," *Scientific Data*, vol. 2, no. 1, p. 150053, 2015.

[73] J. M. Munro, K. Latimer, M. K. Horton, S. Dwaraknath, and K. A. Persson, "An improved symmetry-based approach to reciprocal space path selection

in band structure calculations," *npj Computational Materials*, vol. 6, no. 1, p. 112, 2020.

[74] K. Latimer, S. Dwaraknath, K. Mathew, D. Winston, and K. A. Persson, "Evaluation of thermodynamic equations of state across chemistry and structure in the materials project," *npj Computational Materials*, vol. 4, no. 1, p. 40, 2018.

[75] R. Tran, Z. Xu, B. Radhakrishnan, D. Winston, W. Sun, K. A. Persson, and S. P. Ong, "Surface energies of elemental crystals," *Scientific Data*, vol. 3, no. 1, p. 160080, 2016.

[76] A. K. Singh, L. Zhou, A. Shinde, S. K. Suram, J. H. Montoya, D. Winston, J. M. Gregoire, and K. A. Persson, "Electrochemical Stability of Metastable Materials," *Chemistry of Materials*, vol. 29, no. 23, pp. 10159–10167, 2017.

[77] A. M. Patel, J. K. Nørskov, K. A. Persson, and J. H. Montoya, "Efficient Pourbaix diagrams of many-element compounds," *Phys. Chem. Chem. Phys.*, vol. 21, no. 45, pp. 25323–25327, 2019.

[78] M. Aykol, S. S. Dwaraknath, W. Sun, and K. A. Persson, "Thermodynamic limit for synthesis of metastable inorganic materials," *Science Advances*, vol. 4, no. 4, p. eaaq0148, 2018.

[79] H. Ding, S. S. Dwaraknath, L. Garten, P. Ndione, D. Ginley, and K. A. Persson, "Computational Approach for Epitaxial Polymorph Stabilization through Substrate Selection," *ACS Applied Materials & Interfaces*, vol. 8, no. 20, pp. 13086–13093, 2016.

[80] H. Zheng, X.-G. Li, R. Tran, C. Chen, M. Horton, D. Winston, K. A. Persson, and S. P. Ong, "Grain boundary properties of elemental metals," *Acta Materialia*, vol. 186, pp. 40–49, 2020.

[81] A. Jain, S. P. Ong, G. Hautier, W. Chen, W. D. Richards, S. Dacek, S. Cholia, D. Gunter, D. Skinner, G. Ceder, and K. A. Persson, "Commentary: The Materials Project: A materials genome approach to accelerating materials innovation," *APL Materials*, vol. 1, no. 1, p. 11002, 2013.

[82] N. Danilovic, R. Subbaraman, K.-C. Chang, S. H. Chang, Y. J. Kang,

J. Snyder, A. P. Paulikas, D. Strmcnik, Y.-T. Kim, D. Myers, V. R. Stamenkovic, and N. M. Markovic, "Activity-Stability Trends for the Oxygen Evolution Reaction on Monometallic Oxides in Acidic Environments," *Journal Of Physical Chemistry Letters*, vol. 5, pp. 2474–2478, 7 2014.

[83] A. Lončar, D. Escalera-López, S. Cherevko, and N. Hodnik, "Interrelationships between Oxygen Evolution and Iridium Dissolution Mechanisms," 3 2022.

[84] S. Whitaker, "Flow in porous media I: A theoretical derivation of Darcy's law," *Transport in Porous Media*, vol. 1, no. 1, pp. 3–25, 1986.

[85] M. T. Q. S. da Silva, M. do Rocio Cardoso, C. M. P. Veronese, and W. Mazer, "Tortuosity: A brief review," *Materials Today: Proceedings*, vol. 58, pp. 1344–1349, 2022.

[86] A. H. Motagamwala and J. A. Dumesic, "Microkinetic Modeling: A Tool for Rational Catalyst Design," 1 2021.

[87] A. G. Oshchepkov, A. Bonnefont, V. A. Saveleva, V. Papaefthimiou, S. Zafeiratos, S. N. Pronkin, V. N. Parmon, and E. R. Savinova, "Exploring the Influence of the Nickel Oxide Species on the Kinetics of Hydrogen Electrode Reactions in Alkaline Media," *Topics in Catalysis*, vol. 59, pp. 1319–1331, 9 2016.

[88] J. A. Dumisic, D. F. Rudd, L. M. Aparicio, J. E. Rekoske, and A. A. Treviño, *The Microkinetics of heterogeneous catalysis*. ACS professional reference book, Washington: American Chemical Society, 1993.

[89] H. Scott Fogler, *Elements of chemical reaction engineering*, vol. 1. Pearson Education Limitied, 4 ed., 7 2013.

[90] G. Milazzo and S. Caroli, *Tables of standard electrode potentials*. Chichester: Wiley, 1978.

[91] E. S. Davydova, M. Manikandan, D. R. Dekel, and S. Sunde, "Supporting Information for "Effect of the synthetic method on the properties of Ni-based hydrogen oxidation catalysts" †," 2021.

[92] D. C. Grahame, "Mathematical Theory of the Faradaic Admittance - (Pseudocapacity and Polarization Resistance)," *Journal Of The Electrochemical Society*, vol. 99, no. 12, pp. C370–C385, 1952.

[93] E. S. Davydova, M. Manikandan, D. R. Dekel, and S. Sunde, "Effect of the Synthetic Method on the Properties of Ni-Based Hydrogen Oxidation Catalysts," *ACS Applied Energy Materials*, vol. 4, pp. 3404–3423, 4 2021.

[94] A. Reksten, "Iridium-based electrocatalysts for the oxygen evolution reaction," 2016.

[95] N. W. F Phillips, R. H. Singleton, E. A. Hollingshead, A. Damjanovic, A. Dey, and M. Bockris, "Metallurgie des Aluminiums," *Translated from Russian by H. Frahn. 6. M. Rolin and R. Muhlethaler, Bull. Soc. Chim. France*, vol. 113, pp. 739–746, 7 1966.

[96] H. Yu, L. Bonville, J. Jankovic, and R. Maric, "Microscopic insights on the degradation of a PEM water electrolyzer with ultra-low catalyst loading," *Applied Catalysis B: Environmental*, vol. 260, 1 2020.

[97] E. Hairer and G. Wanner, "Stiff differential equations solved by Radau methods," *Journal of Computational and Applied Mathematics*, vol. 111, pp. 93–111, 11 1999.

[98] MathWorks®, "Solve Stiff ODEs," 2023.

[99] S. M. Park, S. Ho, S. Aruliah, M. F. Weber, C. A. Ward, R. Venter, and S. Srinivasan, "Electrochemical Reduction of Oxygen at Platinum Electrodes in KOH Solutions - Temperature and Concentration Effects," *Journal Of The Electrochemical Society*, vol. 133, pp. 1641–1649, 8 1986.

[100] MathWorks®, "ode15s," 2023.

[101] P. E. England Karstensen, "Microkinetic model for degradation of IrO2," 6 2023.

Appendices

A Pourbaix diagram of Ir

A Pourbaix diagram, also called potential-pH (E - pH) diagrams [66, 44, 53] or dominance diagram [53] is a diagram representing the thermodynamic stability as a function of potential and pH [44]. The diagram shows which species is the most dominant/stable species for a given potential-pH condition [53]. Such diagrams are often used in the field of corrosion, but they tell nothing about the kinetics of the reactions[53]. The lines in a Pourbaix diagram represent different equilibria existing in the system, often a metal in contact with water [53]. It is important to note that since the Pourbaix diagram is only a two-dimensional diagram, other variables such as temperature and pressure must be fixed. Both chemical and electrochemical reactions are present in a system described in a Pourbaix diagram. Horizontal lines represent equilibria where there is no transfer of protons or hydroxides, but there is a transfer of electrons, and thus the reaction is purely electrochemical. Vertical lines depict the opposite implying that no electrons are being transferred, but an equilibria with protons or hydroxides. Lastly, diagonal lines are subsequently a combination of the two other lines, meaning an equilibrium which has both protons or hydroxide ions and electrons transfer.[66, 53]. The activity of dissolved ions in the system also affects the dominance areas. Since the system is usually in contact with water, the equilibrium for the OER and HER are also included.

Figure 2.2 is a simplified Pourbaix diagram of Ir in contact with water. The stability regions of Ir(s), IrO_2(s), IrO_3(s), and IrO_4^{2-}(aq) are represented in the diagram with their corresponding equilibrium lines in black. Indeed, there are more species in this system, but this simplified version is sufficient for the scope of the study. In addition, the equilibrium lines for OER and HER are also present as orange dashed lines. The equilibria represented in this diagram include

$$\text{I}: \quad \mathrm{IrO_2(s) + 4\,H^+(aq) + 4\,e^- \rightleftharpoons Ir(s) + 2\,H_2O(l)} \qquad E^\circ_{\text{I}} \quad \text{(A.1)}$$

$$\text{II}: \quad \mathrm{IrO_3(s) + 2\,H^+(aq) + 2\,e^- \rightleftharpoons IrO_2(s) + H_2O(l)} \qquad E^\circ_{\text{II}} \quad \text{(A.2)}$$

$$\text{III}: \quad \mathrm{IrO_4^{2-}(aq) + 2\,H^+ \rightleftharpoons IrO_3(s) + H_2O(l)} \qquad \Delta_r G^\circ_{\text{III}} \quad \text{(A.3)}$$

$$\text{IV}: \quad \mathrm{IrO_4^{2-}(aq) + 4\,H^+ + 2\,e^- \rightleftharpoons IrO_2(s) + 2\,H_2O(l)} \qquad E^\circ_{\text{IV}} \quad \text{(A.4)}$$

$$\text{OER}: \quad \mathrm{O_2(g) + 4\,H^+ + 4\,e^- \rightleftharpoons 2\,H_2O(l)} \qquad E^\circ_{\text{OER}} \quad \text{(A.5)}$$

$$\text{HER}: \quad \mathrm{2\,H^+ + 2\,e^- \rightleftharpoons H_2(g)} \qquad E^\circ_{\text{HER}} \quad \text{(A.6)}$$

By using the Nernst equation, equation 3.13, on the electrochemical reactions A.1, A.2, A.4, A.6, and A.5, solving the potential $E_{n,i}$ for $i = \{\text{I}, \text{II}, \text{IV}, \text{HER}, \text{OER}\}$ as a function of pH, and evaluating the Gibbs free energy at equilibrium[viii] for reaction A.3, the lines to the Pourbaix diagram can be elucidated. By assuming that the activity for all components is equal to unity except for $\mathrm{H^+(aq)}$ and $\mathrm{IrO_4^{2-}(aq)}$ the equilibrium lines describing the Pourbaix diagram becomes

$$E_{n,\text{I}} = E^\circ_{\text{I}} - \frac{4RT}{n_{\text{I}}F}\ln\{10\}p\text{H} \quad \text{(A.7)}$$

$$E_{n,\text{II}} = E^\circ_{\text{II}} - \frac{2RT}{n_{\text{II}}F}\ln\{10\}p\text{H} \quad \text{(A.8)}$$

$$p\text{H}_{\text{III}} = -\frac{p\text{Ir}}{2} - \frac{\Delta_r G^\circ_{\text{III}}}{2\ln\{10\}RT} \quad \text{(A.9)}$$

$$E_{n,\text{IV}} = E^\circ_{\text{IV}} - \frac{RT}{n_{\text{IV}}F}\ln\{10\}p\text{Ir} - \frac{4RT}{n_{\text{IV}}F}\ln\{10\}p\text{H} \quad \text{(A.10)}$$

$$E_{n,\text{HER}} = E^\circ_{\text{HER}} - \frac{2RT}{n_{\text{HER}}F}\ln\{10\}p\text{H} \quad \text{(A.11)}$$

$$E_{n,\text{OER}} = E^\circ_{\text{OER}} - \frac{4RT}{n_{\text{OER}}F}\ln\{10\}p\text{H} \quad \text{(A.12)}$$

where the activity for the proton and the dissolved iridium is substituted with pH and pIr respectively.

[viii] The Gibbs free energy for a reaction $\Delta_r G$ is given by

$$\Delta_{\text{r}}G = \Delta_{\text{r}r}G^\circ + \text{R}T\ln\left\{\prod_{\text{j}} a_{\text{j}}^{\nu_{\text{j}}}\right\}$$

where $\Delta_{\text{r}}G^\circ$ is the standard Gibbs free energy for the reaction at standard conditions. At equilibrium, the Gibbs free energy for the reaction is equal to zero, $\Delta_{\text{r}}G = 0$. [53]

By using data from the free and open resource *The Materials Project*'s[81] app *Material Explorer* [67, 68, 69, 70, 71, 72, 73, 74, 75, 76, 77, 78, 79, 80], along with data from Pourbaix [66], the Pourbaix diagram in Figure 2.2 could be made. It is based on data measured by Pourbaix, and DFT calculations from the *Material explorer* app.

B Oxygen evolution mechanisms on iridium oxides

Kasian *et al.* [25] did a study on the degradation of iridium oxides during oxygen evolution reaction (OER), and found different pathways were favourable depending on the preparation and the electrode potential. They arrived at a two-way mechanism depending on the preparation history. The mechanism studied in this report and the one presented in section 2.6 is the one for thermally prepared oxide, the other mechanism is the one for reactively sputtered oxides, and for metallic iridium, and is recited here.

The initial stages of their two-way mechanism are the same for both ways and start with metallic iridium and proceed through the formation of IrO2

$$\mathrm{Ir(s)} \rightleftharpoons \mathrm{Ir^{3+}} + 3\,\mathrm{e^-} \tag{B.1}$$

$$\mathrm{Ir(s)} + 2\,\mathrm{H_2O(l)} \rightleftharpoons \mathrm{IrO_2(s)} + 4\,\mathrm{H^+} + 4\,\mathrm{e^-} \tag{B.2}$$

$$\mathrm{Ir^{3+}(aq)} + 2\,\mathrm{H_2O(l)} \rightleftharpoons \mathrm{IrO_2(s)} + 4\,\mathrm{H^+} + \mathrm{e^-} \tag{B.3}$$

The dissolution occurring in step B.1, is insignificant if the iridium is already covered by an oxide layer [25]. The steps prior to the formation of iridium oxide are not so relevant for the degradation study on iridium oxide, as this study is, and hence, they are not included in this study. However, they are included here since Kasian *et al.*[25] studied dissolution under OER conditions for both metallic iridium and iridium oxide.

After the iridium oxide is formed, either through step B.2 or B.3, it reacts further with water creating $\mathrm{IrO_2OH}$ through

$$\mathrm{IrO_2(s)} + \mathrm{H_2O(l)} \rightleftharpoons \mathrm{IrO_2OH_{ads}} + \mathrm{H^+(aq)} \tag{B.4}$$

$$\mathrm{IrO_2OH_{ads}} \rightleftharpoons \mathrm{IrO_2OH} + \mathrm{e^-} \tag{B.5}$$

where $\mathrm{IrO_2OH_{ads}}$ is $\mathrm{IrO_2}$ with an adsorbed OH-group and is a short lived intermediate. From here, the reaction mechanism can take two ways, making $\mathrm{IrO_2OH}$ a common intermediate for the two pathways. Now the OER mechanism can either

follow the path most favourable to thermally prepared oxides or the way most favourable to reactively sputtered oxides and metallic iridium. The former is the one studied in this study and elaborated in section 3.1, and the one presented in section 3.2 is modified to alkaline conditions. The proposed mechanism by Kasian *et al.*[25] in acidic conditions after step B.4 is the following for the thermally prepared oxide

$$\mathrm{IrO_2OH} \rightleftharpoons \mathrm{IrO_3} + \mathrm{H^+(aq)} + \mathrm{e^-} \tag{B.6}$$

$$\mathrm{IrO_3} + \mathrm{H_2O(l)} \rightleftharpoons \mathrm{IrO_4^{2-}(aq)} + 2\,\mathrm{H^+(aq)} \tag{B.7}$$

$$\mathrm{IrO_3} \rightleftharpoons \mathrm{IrO_2(s)} + \frac{1}{2}\mathrm{O_2(aq)} \tag{B.8}$$

where the dissolution in step B.7 by the dissolution of $\mathrm{IrO_4^{2-}}$. As illustrated in Figure 3.1, this mechanism is a two-way mechanism which can either lead to dissolution by step B.7 or to the formation of oxygen by step B.8.

Now the latter path, the one for reactively sputtered iridium oxide and metallic iridium is described to undergo the following steps after step B.5,

$$2\,\mathrm{IrO_2OH} \rightleftharpoons \mathrm{HIrO_2(s)} + \mathrm{O_2(g)} \tag{B.9}$$

$$\mathrm{HIrO_2(s)} + 3\,\mathrm{H^+} \rightleftharpoons \mathrm{Ir^{3+}} + 2\,\mathrm{H_2O(l)} \tag{B.10}$$

$$\mathrm{HIrO_2(s)} \rightleftharpoons \mathrm{IrO_2} + \mathrm{H^+} + \mathrm{e^-} \tag{B.11}$$

where the oxygen is produced in step B.9. This part is also a two-way mechanism, where the reaction can either go to dissolution by step B.10 via $\mathrm{Ir^{3+}}$, after oxygen is produced or recreate the catalyst layer, $\mathrm{IrO_2}$, by step B.11, and thus work as an electrocatalyst.

Even though Kasian *et al.*[25] studied the dissolution of iridium oxide under acidic conditions, their mechanism for OER on thermally prepared oxide is still assumed to describe the dissolution in alkaline conditions by introducing $\mathrm{OH^-}$ to the pH-dependent steps as elaborated in section 3.2.

Mayrhofer *et al.*[30] mention that the electrochemistry for iridium is quite different

in acidic compared to alkaline environments, making the transfer of knowledge from one to the other difficult. On the other hand, Dam *et al.* [29] hypothesise that the mechanistic path for iridium dissolution might change towards utilising hydroxide ions in alkaline conditions, but that the degradation will still proceed through the adsorbed oxygen, O_{ad}, on IrO_2, by the formation of IrO_3 as it is displayed here. This encourages, the assumption that the mechanism is still valid in alkaline conditions by indeed introducing hydroxide ions in the mechanistic path.

C Additional results

Additional results based on polarisation curves from other experiments than Mayrhofer *et al.* [1] and Schalenbach *et al.* [2] which do not bring new insights than those presented in Section 4. The results presented in Section 4 are based on polarisation curves from the same experiments that the degradation studies were conducted.

C.1 Acidic model

Additional results from the study based on polarisation curves on iridium/iridium oxide in acidic media from Scohy *et al.* [24], Damjanovic *et al.* [95], and Cherevko *et al.* [50]. These results convey the same trends as the one presented in Section 4, and since they don't bring any new results, they are added here.

The numerical fitting of Equation 3.30 to the polarisation data from Scohy *et al.* [24], Damjanovic *et al.* [95], and Cherevko *et al.* [50]. are shown in Figure C1. The coefficient of determination, R^2, is also added.

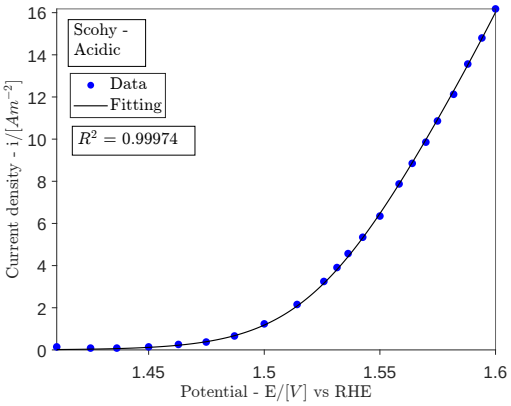

(a) The sampled data from the polarisation curve on activated Ir(III) in $0.05\,\mathrm{mol\,L^{-1}}$ H_2SO_4 from Scohy *et al.* [24] in blue circles and the corresponding curve fitting in black line. The coefficient of determination is $R^2 = 0.99974$

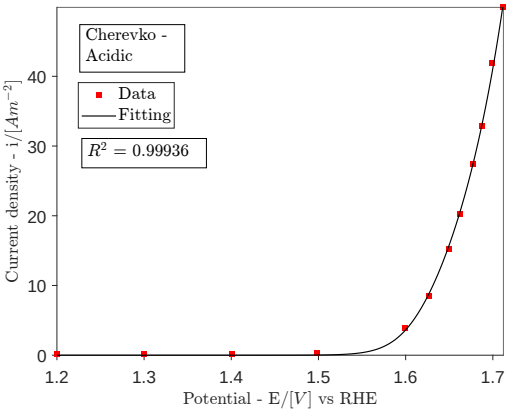

(b) The sampled data from the polarisation curve on IrO_2 in $0.1\,\mathrm{mol\,L^{-1}}$ H_2SO_4 from Cherevko *et al.* [50] in red squares and the corresponding curve fitting in black line. The coefficient of determination is $R^2 = 0.99936$

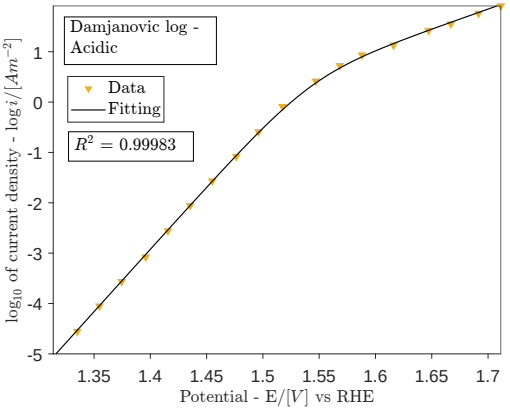

(c) The sampled data from the polarisation curve on Ir in 1 N $HClO_4$ from Damjanovic *et al.* [95] in orange downward triangles and the corresponding curve fitting based on the logarithm of the current density in black line. The coefficient of determination is $R^2 = 0.99983$

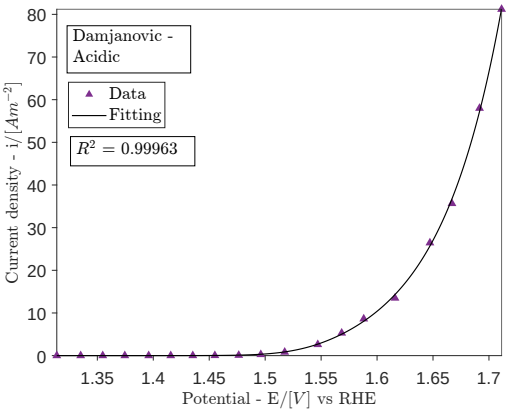

(d) The sampled data from the polarisation curve on Ir in 1 N $HClO_4$ from Damjanovic *et al.* [95] in purple upwards triangles and the corresponding curve fitting in black line. The coefficient of determination is $R^2 = 0.99963$

Figure C1: The sampled data from the polarisation curves from Scohy *et al.* [24], blue circles in figure C1a, Cherevko *et al.* [50], red squares in figure C1b, and Damjanovic *et al.* [95], orange downward triangles in figure C1c, and purple upward triangles in figure C1d, along with their corresponding fits in black line. The coefficient of determination is also displayed in their respective figures. All these data are for acidic data and acidic data fitting

The resulting fitting parameters for each of the CV curves shown in Figure C1 are given in Table C.1. Table C.1 shows the model parameters used to solve Equation 3.33.

Table C.1: Model parameters used for the computation of the dissolution rates for the acidic model

Parameter	Scohy[24]	Damjanovic/log[95]	Cherevko[50]	Unit
$\Gamma k_{2+}^{0} \cdot 10^{7}$	18.26	0.6528/0.5969	0.4518	$[\mathrm{mol\,m^{-2}\,s^{-1}}]$
$K_{1}^{0} \cdot 10^{-5}$	2.435	2.179/2.952	897.3	[−]
α	0.7371	0.5423/0.5346	0.5829	[−]
T		298[a]		[K]
$c_{\mathrm{H^+}}$		0.2[b]		$[\mathrm{mol\,L^{-1}}]$

[a] Temperature for electrochemical measurements from Mayrhofer *et al*[1].

[b] The concentration of H^+ given by Mayrhofer *et al*[1] to be $0.01\,\mathrm{mol\,L^{-1}}$ H_2SO_4, and full dissociation is assumed.

The solution to Equation 3.33, $\Gamma\theta_2$, as a function of time, t, based on the numerical approach in the acidic model elaborated in Section 3 are shown in Figure C2. The parameters from Table C.1 were used to find a solution. In addition, the potential regime, $E(t)$, from Mayrhofer *et al.* [1] is also added in grey dashed lines.

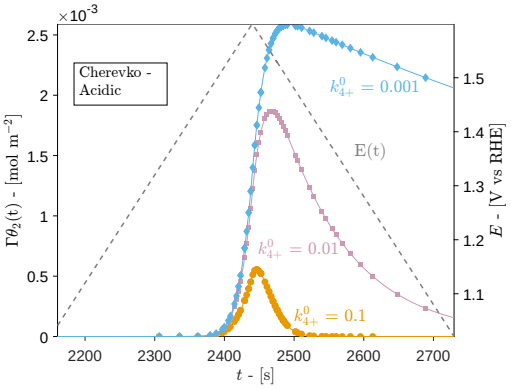

(a) The solution of equation 3.33 as a function of time for three different values of k^0_{4+} based on the data obtained from Cherevko *et al.* [50]. The potential regime used in the solution is also provided on the right y-axis.

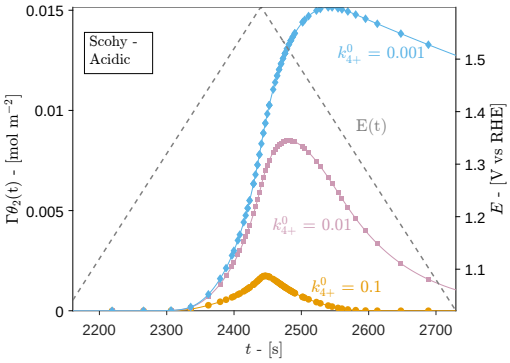

(b) The solution of equation 3.33 as a function of time for three different values of k^0_{4+} based on the data obtained from Scohy *et al.* [24]. The potential regime used in the solution is also provided on the right y-axis.

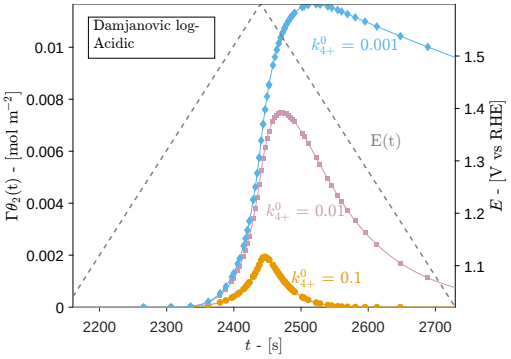

(c) The solution of equation 3.33 as a function of time for three different values of k^0_{4+} based on the data obtained from Damjanovic *et al.* [95], but based on the logarithmic fitting of equation 3.30. The potential regime used in the solution is also provided on the right y-axis.

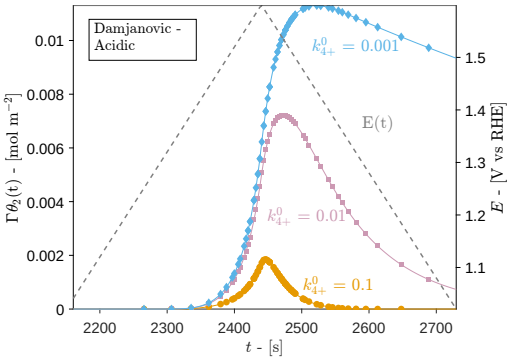

(d) The solution of equation 3.33 as a function of time for three different values of k^0_{4+} based on the data obtained from Damjanovic *et al.* [95]. The potential regime used in the solution is also provided on the right y-axis.

Figure C2: All subfigures display the solution of 3.33 as a function of time, t, for three different values of k^0_{4+}, which is the forward chemical rate constant for step 3.4. The product $\Gamma\theta_2$ is a measure of the surface concentration of IrO_3 on the surface of IrO_2, where Γ is the total surface concentration of active sites, and is unknown, while θ_2 is the fractional site coverage with respect to Γ. The data used in this figure is gathered from Scohy *et al.*[24], figure C2b, Cherevko *et al.*[50], figure C2a, and Damjanovic *et al.* [95], figure C2d and C2c. The potential regime is also provided and plotted against the second y-axis to the left. Markers represent the sampled data from the degradation data

The solution to Equation 3.33, $\Gamma\theta_2$, as a function of potential, E, is shown in Figure C3. For reference, the dissolution data from Mayrhofer *et al.* [1] is also displayed in grey dashed lines for comparison.

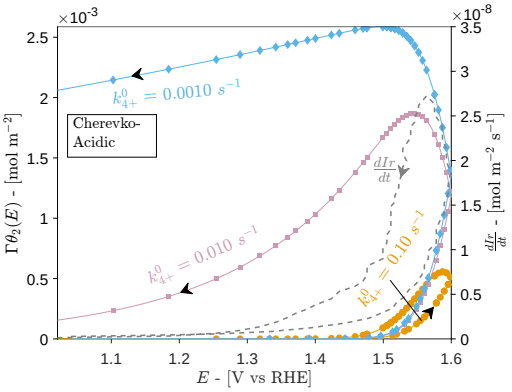

(a) The solution of equation 3.33 is plotted as a function of potential for three different values of k^0_{4+} based on the data obtained from Scohy *et al.* [24]. The degradation data from Mayrhofer *et al.* [1] is provided for reference on the right y-axis.

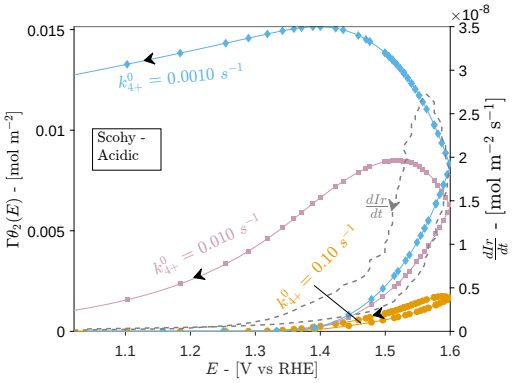

(b) The solution of equation 3.33 is plotted as a function of potential for three different values of k^0_{4+} based on the data obtained from Cherevko *et al.* [50]. The degradation data from Mayrhofer *et al.* [1] is provided for reference on the right y-axis.

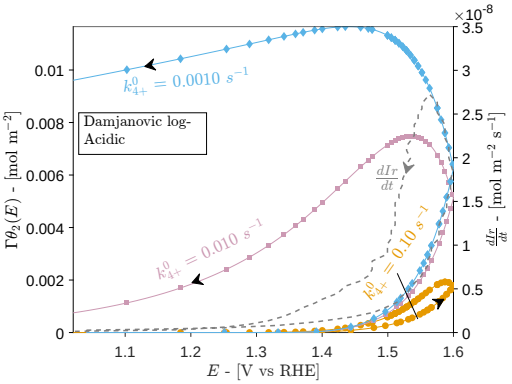

(c) The solution of equation 3.33 is plotted as a function of potential for three different values of k^0_{4+} based on the data obtained from Damjanovic *et al.* [95], but based on the logarithmic fitting of equation 3.30. The degradation data from Mayrhofer *et al* [1] is provided for reference on the right y-axis.

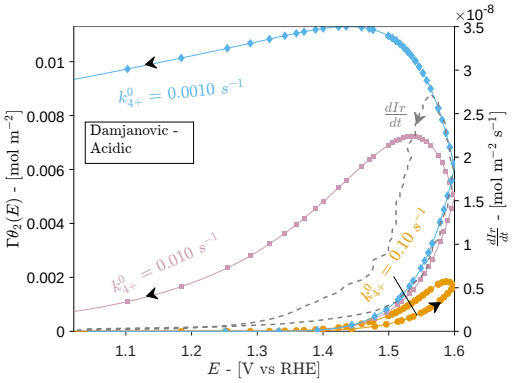

(d) The solution of equation 3.33 is plotted as a function of potential for three different values of k^0_{4+} based on the data obtained from Damjanovic *et al* [95]. The degradation data from Mayrhofer *et al* [1] is provided for reference on the right y-axis.

Figure C3: All subfigures display the solution of 3.33 as a function of potential, E, for three different values of k^0_{4+}, which is the forward rate constant for step 3.4. The product $\Gamma\theta_2$ is a measure of the surface concentration of IrO_3 on the surface of IrO_2, where Γ is the total surface concentration of active sites, and is unknown, while θ_2 is the fractional site coverage with respect to Γ. The data used in this figure is gathered from Scohy *et al*[24], figure C2b, Cherevko *et al*[50], figure C2a, and Damjanovic *et al* [95], figure C2d and C2c. The degradation data from Mayrhofer *et al* [1] is also provided on the right y-axis as a reference. Markers represent the sampled data from the degradation data

The model parameters used to obtain the solution to Equation 3.33 are given in Table C.1

The rate of dissolution,r_{Diss}, also called r_{3+} in section 3, is plotted against time, t, along with the degradation data from Mayrhofer *et al*[1]. The simulated dissolution rate is aiming to recreate the degradation data from Mayrhofer *et al* [1].

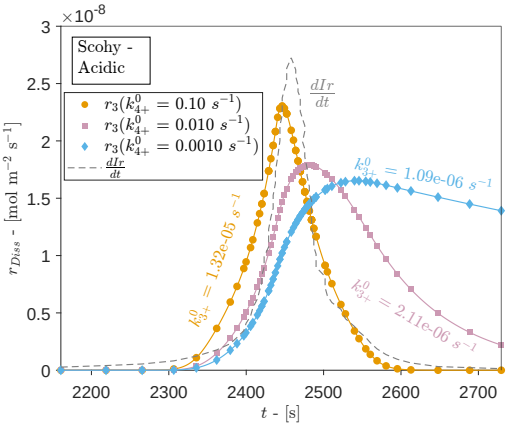

(a) The rate of degradation, r_{3+}, as a function of time, t, for three different values of k^0_{4+}, based on the data from Scohy *et al* [24] for the acidic model. The resulting rate constant for the degradation, k^0_{3+}, is also provided with their respective solutions. The degradation data from Mayrhofer *et al* [1] is also provided.

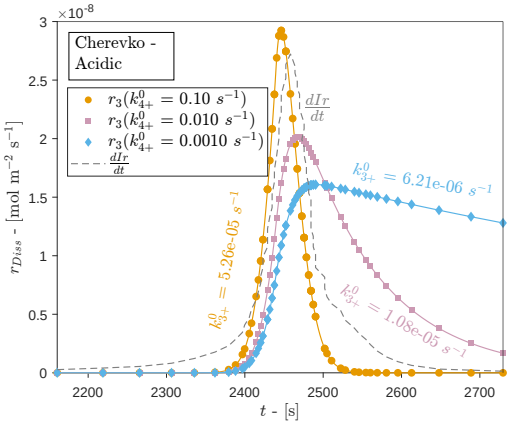

(b) The rate of degradation, r_{3+}, as a function of time, t, for three different values of k^0_{4+}, based on the data from Cherevko *et al* [50] for the acidic model. The resulting rate constant for the degradation, k^0_{3+}, is also provided with their respective solutions. The degradation data from Mayrhofer *et al* [1] is also provided.

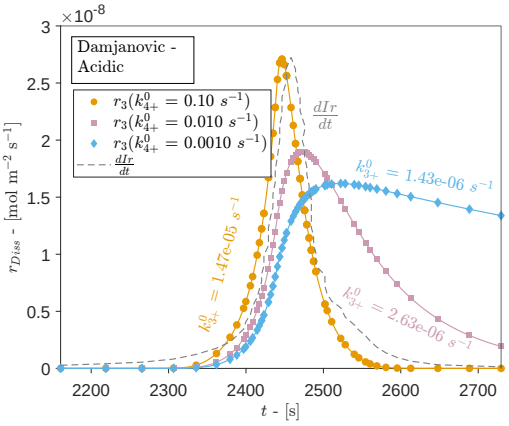

(c) The rate of degradation, r_{3+}, as a function of time, t, for three different values of k^0_{4+}, based on the data from Damjanovic *et al* [95] for the acidic model. The resulting rate constant for the degradation, k^0_{3+}, is also provided with their respective solutions. The degradation data from Mayrhofer *et al* [1] is also provided.

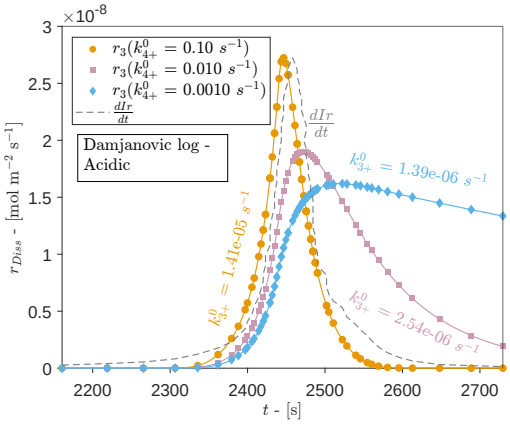

(d) The rate of degradation, r_{3+}, as a function of time, t, for three different values of k^0_{4+}, based on the data from Damjanovic *et al* [95] for the acidic model, but the logarithmic fitting. The resulting rate constant for the degradation, k^0_{3+}, is also provided with their respective solutions. The degradation data from Mayrhofer *et al* [1] is also provided.

Figure C4: All figures display the rate of dissolution as a function of time, t, for three different values of k^0_{4+}, which is the forward rate constant for step 3.4 for the acidic model. The rate of dissolution is given by r_{3+} from step 3.3 and the chemical rate constant k^0_{3+} is a measure of how fast the rate of dissolution is. The degradation data from Mayrhofer *et al* [1] is also provided in grey dashed lines. Markers represent the sampled data from the degradation data

C.2 Alkaline model

Additional results from the study based on CV data on iridium/iridium oxide in alkaline media from Cherevko *et al* [50] and Damjanovic *et al* [95]. These results

convey the same trends as the one presented in Section 4, and since they don't bring any new results, they are added here.

The numerical fitting of Equation 3.31 to the polarisation data from Cherevko *et al* [50] and Damjanovic *et al* [95]. are shown in Figure C5. The coefficient of determination, R^2, is also added.

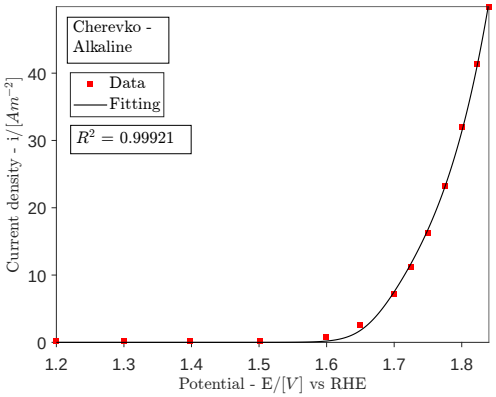

(a) The sampled data from the polarisation curve on IrO_2 in 0.05 mol L^{-1} NaOH from Cherevko *et al* [50] in red squares and the corresponding curve fitting in black line. The coefficient of determination is $R^2 = 0.99921$

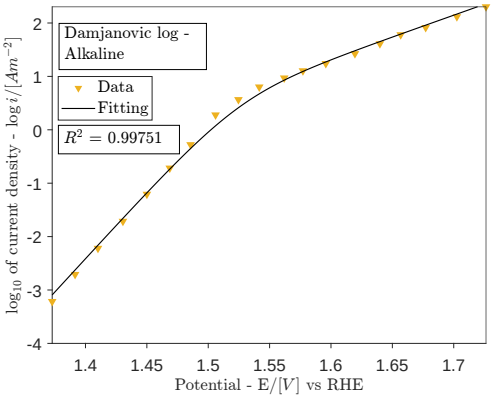

(b) The sampled data from the polarisation curve on Ir in 1 N KOH from Damjanovic *et al* [95] in orange downward triangles and the corresponding curve fitting based on the logarithm of the current density in black line. The coefficient of determination is $R^2 = 0.99583$

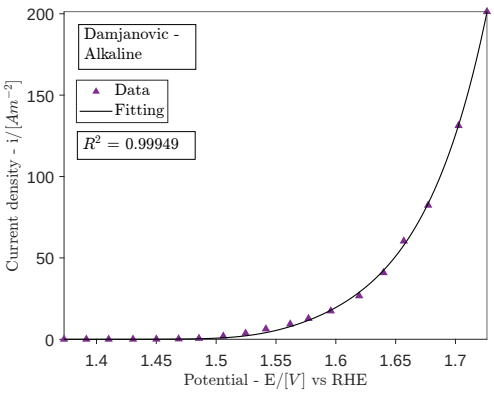

(c) The sampled data from the polarisation curve on Ir in 1 N KOH from Damjanovic *et al* [95] in purple upward triangles and the corresponding curve fitting in black line. The coefficient of determination is $R^2 = 0.99993$

Figure C5: The sampled data from the polarisation curves from Cherevko *et al* [50] in red squares in figure C5a and Damjanovic *et al* [95], orange downward triangles in figure C5b and purple upward triangles in figure C5c, along with their corresponding fits in black line. The coefficient of determination is also displayed in their respective figures. All these data are for alkaline data and alkaline data fitting

The fitting parameters obtained from fitting Equation 3.31 to the CV data showed in Figure C5 were used as model parameters together with the hydroxide activity

and temperature from Schakenbach *et al.*[2]. The model parameters were used to solve Equation 3.34

Table C.2: Model parameters used for the computation of the dissolution rates for the alkaline model.

Parameter	Cherevko[50]	Damjanovic/log[95]	Unit
$\Gamma k_{2+}^{0} \cdot 10^{6}$	3.732	0.1049/0.08199	$[\mathrm{mol\,m^{-2}\,s^{-1}}]$
$K_{1}^{0} \cdot 10^{-5}$	4.46	0.5203 /1.469	$[-]$
α	0.7007	0.5349/0.5128	$[-]$
T		298[a]	[K]
$c_{\mathrm{OH^-}}$		0.05[b]	$[\mathrm{mol\,L^{-1}}]$

[a] Temperature for electrochemical measurements from Schalenbach *et al.*[2].

[b] The concentration of $\mathrm{OH^-}$ given by Schalenbach *et al.*[2] to be $0.05\,\mathrm{mol\,L^{-1}}$ KOH, and full dissociation is assumed.

The solution to Equation 3.34, $\Gamma\theta_2$, as a function of time, t, based on the numerical approach in the alkaline model elaborated in Section 3 are shown in Figure C6. The solution was obtained by the use of the numerical parameters in Table C.2. In addition, the potential regime, $E(t)$ from Schalenbach *et al* [2] is also added in grey dashed lines.

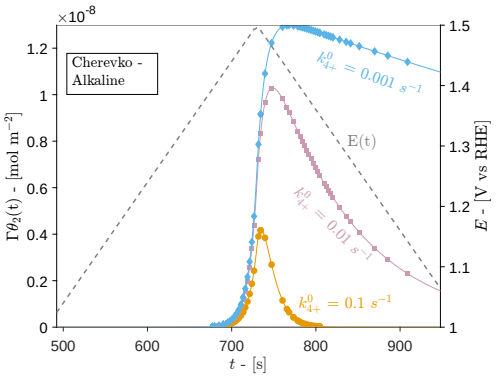

(a) The solution of equation 3.34 as a function of time for three different values of k^0_{4+} based on the data obtained from Cherevko *et al* [50]. The potential regime used in the solution is also provided on the right y-axis.

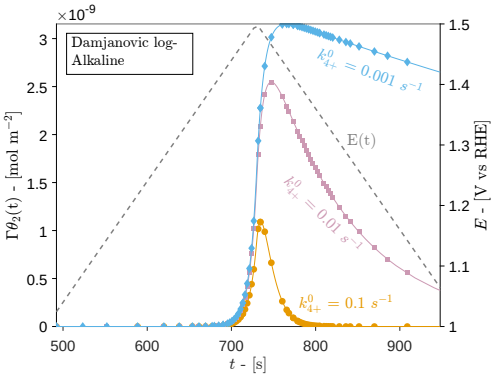

(b) The solution of equation 3.34 as a function of time for three different values of k^0_{4+} based on the data obtained from Damjanovic *et al* [95], but based on the logarithmic fitting of... . The potential regime used in the solution is also provided on the right y-axis.

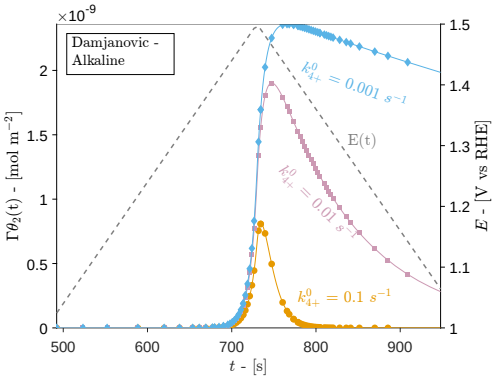

(c) The solution of equation 3.34 as a function of time for three different values of k^0_{4+} based on the data obtained from Damjanovic *et al* [95]. The potential regime used in the solution is also provided on the right y-axis.

Figure C6: All subfigures display the solution of 3.34 as a function of time, t, for three different values of k^0_{4+}, which is the forward rate constant for step 3.17. The product $\Gamma\theta_2$ is a measure of the surface concentration of IrO_3 on the surface of IrO_2, where Γ is the total surface concentration of active sites, and is unknown, while θ_2 is the fractional site coverage with respect to Γ. The data used in this figure is gathered from Cherevko *et al*[50], figure C2a, and Damjanovic *et al* [95], figure C2d and C2c. The potential regime is also provided and plotted against the second y-axis to the left. Markers represent the sampled data from the degradation data

The solution to Equation 3.34, $\Gamma\theta_2$, as a function of potential, E, is shown in Figure C7. For reference, the dissolution data from Schalenbach *et al* [2] is also displayed in grey dashed lines for comparison.

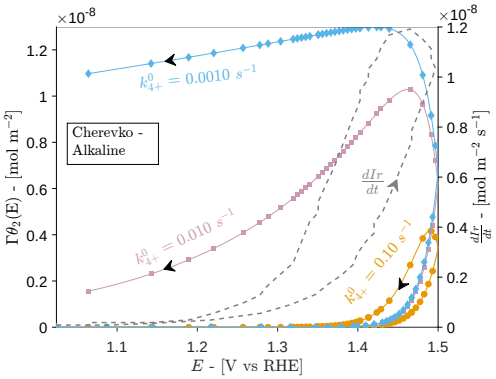

(a) The solution of equation 3.34 as a function of potential for three different values of k^0_{4+} based on the data obtained from Cherevko *et al* [50]. The degradation data from Mayrhofer *et al* [1] is provided for reference on the right y-axis.

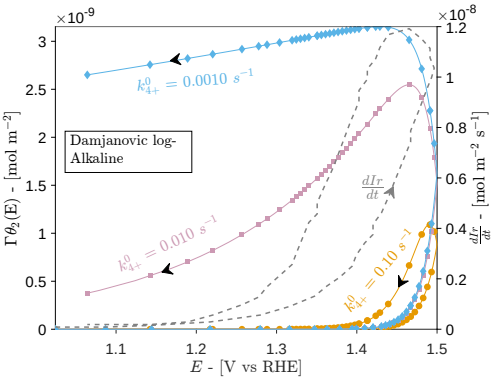

(b) The solution of equation 3.34 as a function of potential for three different values of k^0_{4+} based on the data obtained from Damjanovic *et al* [95], but based on the logarithmic fit. The degradation data from Mayrhofer *et al* [1] is provided for reference on the right y-axis.

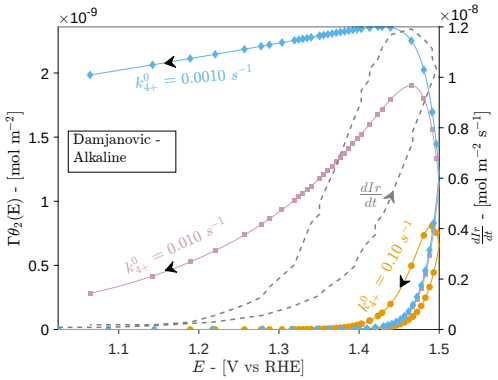

(c) The solution of equation 3.34 as a function of potential for three different values of k^0_{4+} based on the data obtained from Damjanovic *et al.* [95]. The degradation data from Mayrhofer *et al.* [1] is provided for reference on the right y-axis.

Figure C7: All subfigures display the solution of 3.34 as a function of potential, E, for three different values of k^0_{4+}, which is the forward rate constant for step 3.17. The product $\Gamma\theta_2$ is a measure of the surface concentration of IrO_3 on the surface of IrO_2, where Γ is the total surface concentration of active sites, and is unknown, while θ_2 is the fractional site coverage with respect to Γ. The data used in this figure is gathered from Cherevko *et al.*[50], figure C2a and Damjanovic *et al.* [95], figure C6c and C6b. The degradation data from Schalenbach *et al.* [2] is also provided on the right y-axis as a reference. Markers represent the sampled data from the degradation data

The rate of dissolution,r_{Diss}, also called r_{3+} in section 3, is plotted against time, t, along with the degradation data from Schalenbach *et al.* [2]. The simulated dissolution rate is aiming to recreate the degradation data from Schalenbach *et al.* [2].

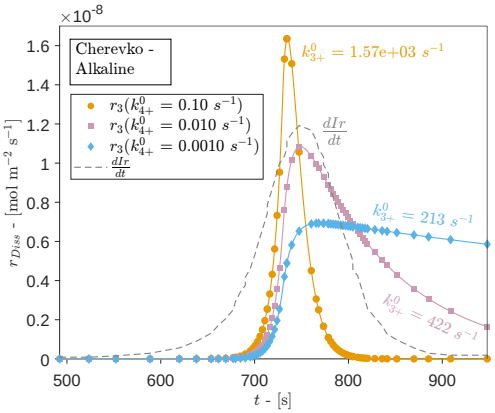

(a) The rate of degradation, r_{3+}, as a function of time, t, for three different values of k^0_{4+}, based on the data from Cherevko *et al.* [50] for the alkaline model. The resulting rate constant for the degradation, k^0_{3+}, is also provided with their respective solutions. The degradation data from Mayrhofer *et al.* [1] is also provided in grey dashed lines.

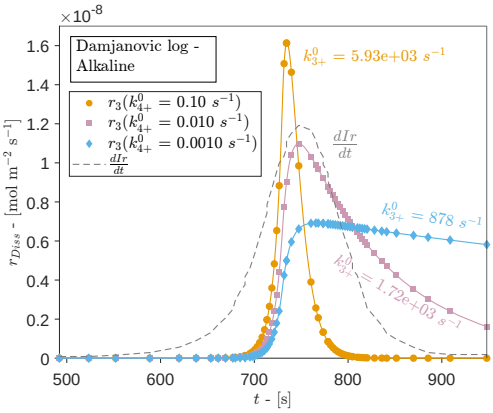

(b) The rate of degradation, r_{3+}, as a function of time, t, for three different values of k^0_{4+}, based on the data from Damjanovic *et al.* [95] for the alkaline model based on the logarithmic fitting. The resulting rate constant for the degradation, k^0_{3+}, is also provided with their respective solutions. The degradation data from Mayrhofer *et al.* [1] is also provided in grey dashed lines.

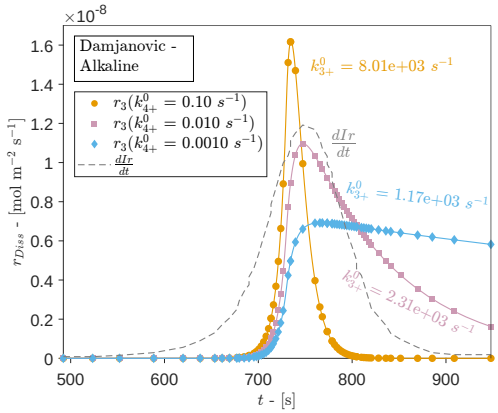

(c) The rate of degradation, r_{3+}, as a function of time, t, for three different values of k^0_{4+}, based on the data from Damjanovic *et al.* [95] for the alkaline model. The resulting rate constant for the degradation, k^0_{3+}, is also provided with their respective solutions. The degradation data from Mayrhofer *et al.* [1] is also provided in grey dashed lines.

Figure C8: All figures display the rate of dissolution as a function of time, t, for three different values of k^0_{4+}, which is the forward rate constant for step 3.17, for the alkaline model. The rate of dissolution is given by r_{3+} from step 3.16 and the chemical rate constant k^0_{3+} is a measure of how fast the rate of dissolution is. The degradation data from Mayrhofer *et al.* [1] is also provided in grey dashed lines. Markers represent the sampled data from the degradation data

D Full rate analysis

The study of the oxygen evolution reaction (OER) mechanism has been researched extensively and is still poorly understood. In this study, a microkinetic approach with the assumption of a rate-determining step (rds) was performed. Though, as mentioned in section 3.3, it is often advisable to conduct a more complex and full dynamic analysis [36, 28]. The motivation to conduct such a complex analysis by avoiding steady-state assumptions and quasi-steady-state assumptions is that these approximations can undermine the complexity of the system, and can hide the presence of important kinetic parameters such as several Tafel slopes for different regions of the potential. However, a mechanistic study without assuming the presence of an rds and avoiding quasi-steady-state assumptions was performed based on the works of Reksten [94] in "Appendix B: Electrochemical Oxide Path without Assumption of Quasi-Equilibrium", though her derivation is in an acidic environment.

As mentioned in section 3, the dissolution step was neglected since the OER pathway would most likely dominate the total current and the reaction mechanism is the same as the one presented in the same section. The reaction mechanism of the OER on IrO_2 in an alkaline environment without the dissolution step is also given here as

$$IrO_2(s) + OH^-(aq) \underset{k_{1-}}{\overset{k_{1+}}{\rightleftharpoons}} IrO_2OH + e^- \tag{D.1}$$

$$IrO_2OH + OH^-(aq) \underset{k_{2-}}{\overset{k_{2+}}{\rightleftharpoons}} IrO_3 + H_2O(l) + e^- \tag{D.2}$$

$$IrO_3 \underset{k^0_{4-}}{\overset{k^0_{4+}}{\rightleftharpoons}} IrO_2(s) + \frac{1}{2}O_2(aq) \tag{D.3}$$

where the same notation as used in the study in section 3 is applied. This is the same as Bockris [59] electrochemical oxide path on a catalyst surface in alkaline conditions. The derivation from Reksten [94] is based on the assumptions that everything is occurring under steady state and no presence of catalyst dissolution. Hence, non of the reaction rates are equal to zero, but this allows the different rate equations to be set equal to each other. Still, this is an approximate solution since the rate of dissolution is still neglected, and the presence of dissolution would

contradict the steady-state assumption.

With the following rate equations based on the power law model

$$r_1 = r_{1+} - r_{1-} = k_{1+}\Gamma(1-\theta_1-\theta_2)a_{\mathrm{OH^-}} - k_{1-}\Gamma\theta_1 \tag{D.4}$$

$$r_2 = r_{2+} - r_{2-} = k_{2+}\Gamma\theta_1 a_{\mathrm{OH^-}} - k_{2-}\Gamma\theta_2 a_{\mathrm{H_2O}} \tag{D.5}$$

$$r_4 = r_{4+} - r_{4-} = k^0_{4+}\Gamma\theta_2 - k^0_{4-}\Gamma(1-\theta_1-\theta_2)\sqrt{a_{\mathrm{O_2}}} \tag{D.6}$$

is the same as previously. The rate constants for the electrochemical steps, step D.1 and D.2, follow the same definition as introduced earlier in section 3, see equation 3.11 and 3.12, and is a function of the chemical rate constants, $k^0_{i\pm}$, and potential, E, where $+$ denotes forward an $-$ denotes backward reaction respectively. θ_1 and θ_2 is denoting the fractional surface concentration of species IrO_2OH and IrO_3 with respect to the total surface concentration of active sites, Γ. Assuming steady state ($r_1 = r_2 = r_4 = r$), the total rate of reaction becomes

$$\begin{aligned} r = {} & \Gamma a_{\mathrm{OH^-}}\left[1 - B\left(1 + K_2(E)\frac{a_{\mathrm{H_2O}}}{a_{\mathrm{OH^-}}} + K_1(E)K_2(E)\frac{a_{\mathrm{H_2O}}}{a^2_{\mathrm{OH^-}}}\right)\right] \\ & \cdot\left\{\frac{1}{k_{1+}(E)} + \frac{1}{k_{2+}(E)} + \frac{K_1(E)}{k_{2+}(E)a_{\mathrm{OH^-}}}\right. \\ & \left. +\Gamma A a_{\mathrm{OH^-}}\left[1 + K_2(E)\frac{a_{\mathrm{H_2O}}}{a_{\mathrm{OH^-}}} + K_1(E)K_2(E)\frac{a_{\mathrm{H_2O}}}{a^2_{\mathrm{OH^-}}}\right]\right\}^{-1} \end{aligned} \tag{D.7}$$

where A and B are

$$A = \frac{\frac{1}{k^0_{4+}} - \frac{K^0_4\sqrt{a_{\mathrm{O_2}}}}{k_{2+}(E)a_{\mathrm{OH^-}}}}{\Gamma\left[1 + k^0_4\left(K_2(E)\frac{a_{\mathrm{H_2O}}}{a_{\mathrm{OH^-}}} + 1\right)\sqrt{a_{\mathrm{O2}}}\right]}$$

$$B = \frac{K^0_4\sqrt{a_{\mathrm{O_2}}}}{1 + K^0_4\left[K_2(E)\frac{a_{\mathrm{H_2O}}}{a_{\mathrm{OH^-}}} + 1\right]\sqrt{a_{\mathrm{O2}}}}$$

and

$$K_i = \frac{k_{i-}}{k_{i+}} = K_i^0 \exp\left\{-\frac{F}{RT}(E - E_n)\right\}, \quad i = \{1, 2\}$$
$$K_i^0 = \frac{k_{i-}^0}{k_{i+}^0}, \quad i = \{1, 2, 3\}$$

In addition, there is indeed a thermodynamic constraint that the system must obey which is

$$K = \frac{a_{\mathrm{H_2O}}\sqrt{a_{\mathrm{O_2}}}}{a_{\mathrm{OH^-}}^2} = \frac{1}{K_1^0 K_2^0 K_4^0} \tag{D.8}$$

and is derived by evaluating the system at equilibrium when $E = E_n$.

Without any further assumptions being made, there are eight kinetic parameters that are somewhat unknown, being K_1^0, k_{1+}^0, α_1, K_2^0, k_{2+}^0, α_2, K_4^0, k_{4+}^0. In addition, the total surface concentration of active sites, Γ, is usually unknown unless the reaction is occurring on a well-defined monocrystalline crystallographic plane. By using the thermodynamic constraint on the system given in equation D.8, it removes one fitting parameter since it can be described by two others, still there are seven kinetic parameters and one intrinsic property that is till unknown. If the same procedure as described in section 3 were to be undertaken without assuming an rds, the transfer coefficient for step 3.14 and 3.15 to be the same, and lastly, letting Γ be a fitting parameter as well, the numerical fitting procedure would lead to unphysical descriptions of the fitting parameters because of the many unknowns. The result of the numeical fitting procedure of equation D.7 to the sampled data of Schalenbach *et al.* [2] and [50] is given figure D1

with the resulting fitting parameters shown in Table D.2

It is easy to see that the result of too many unknown parameters, also increases the amount of uncertainty related to these coefficients. The confidence interval for all parameters is several orders of magnitude larger than the actual value, and the lower bounds are even negative which are nonphysical for empirically positive parameters, even though the coefficient of determination says the fitted curve describes the data well, as shown in figure D1. Because the actual fitting itself is also very prone to the starting values, because the large span in the confidence

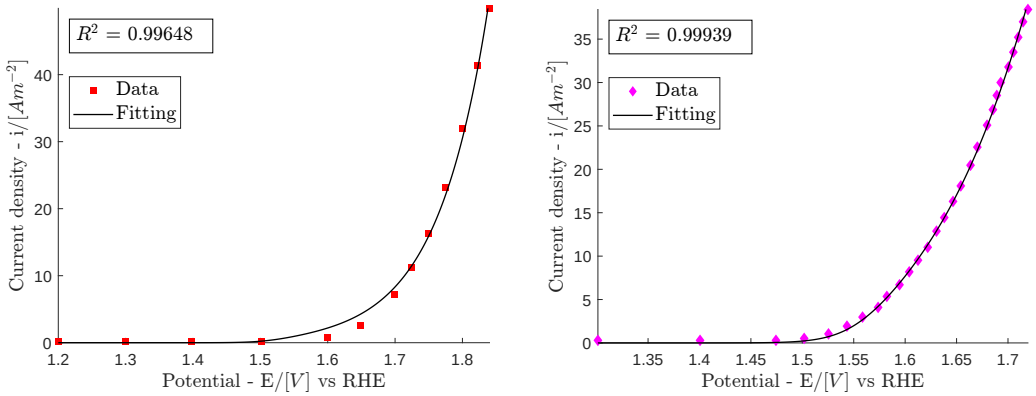

(a) The sampled data from the polarisation curve on IrO_2 in 0.05 mol L^{-1} NaOH from Cherevko *et al.* [50] in red squares and the corresponding curve fitting in black line based on equation D.7. The coefficient of determination is $R^2 = 0.99648$

(b) The sampled data from the polarisation curve on Ir in 0.05 mol L^{-1} NaOH from Schalenbach *et al.* [2] in magenta diamonds and the corresponding curve fitting black line based on equation D.7. The coefficient of determination is $R^2 = 0.99939$

Figure D1: The sampled data from the polarisation curves from Cherevko *et al.* [50] in red squares in figure C5a, Schalenbach *et al.* [2] in magenta diamonds in figure D1b along with their corresponding fits in black line based on equation D.7 with K_1^0, k_{1+}^0, α_1, K_2^0, k_{2+}^0, α_2, k_{4+}^0, and Γ as fitting parameters. The coefficient of determination is also displayed in their respective figures.

interval, and the nonphysical values of the confidence interval ultimately led to abandoning this approach entirely.

Though to simplify this expression, one can assume that the last step, step D.3, in the mechanism is irreversible towards the right, meaning that $k_{4+}^0 \gg 1$, which leads to $K_4^0 \ll 1$. This also implies that $A \to 0$ and $B \ll 1$, which simplifies the full rate of reaction expressed by equation D.7, to

$$r = \frac{\Gamma k_{2+}^0 \exp\left\{\frac{(1-\alpha_2)F}{RT}(E - E_n)\right\} a_{\mathrm{OH^-}}}{1 + \frac{k_{2+}^0}{k_{1+}^0} + \frac{K_1(E)}{a_{\mathrm{OH^-}}}} = \frac{i_{OER}}{2F} \approx \frac{i}{2F} \tag{D.9}$$

where there is also assumed that $\alpha_1 = \alpha_2 = \alpha$. Even though, three parameters disappear, it is still four kinetic parameters left, being k_{2+}^0, $\alpha_2 = \alpha$, k_{1+}^0, and K_1^0, and the surface concentration, Γ. If the surface concentration is assumed to be the same as for the (110) plan of rutile on IrO_2, see section 4, the numerical fitting procedure improves to some extent as can be seen in figure D2

Still, the uncertainties in the fitting parameters become unreasonably high

Like the approach with the full rate and without any assumptions, this approach

Table D.1: Results from the numerical fitting of equation D.7 where K_1^0, k_{1+}^0, α_1, K_2^0, k_{2+}^0, α_2, k_{4+}^0, and Γ were fitting parameters and K_4^0 were omitted by the use of equation D.8. The data used for the fitting was extracted from polarisation curves from Cherevko *et al.* [50] and Schalenbach *et al.* [2] for alkaline solutions.

Fitting parameters	Cherevko	Schalenbach
K_1^0 [−]	$1030\ (-1.175 \cdot 10^6, 1.177 \cdot 10^6)$	$1320\ (-1140, 3781)$
k_{1+}^0 [s^{-1}]	$1182\ (-2.286 \cdot 10^{10}, 2.286 \cdot 10^{10})$	$1045\ (-6.403 \cdot 10^8, 6.403 \cdot 10^8)$
K_2^0 [−]	$11.81\ (-2.056 \cdot 10^8, 2.056 \cdot 10^8)$	$15.91\ (-2.059 \cdot 10^7, 2.059 \cdot 10^7)$
k_{2+}^0 [s^{-1}]	$1.387\ (-2.699 \cdot 10^7, 2.699 \cdot 10^7)$	$4.591\ (-2.813 \cdot^1 06, 2.813 \cdot 10^6)$
k_{4+}^0 [s^{-1}]	$297.1\ (-8.992 \cdot 10^8, 8.992 \cdot 10^8)$	$585\ (-1.388 \cdot 10^9, 1.388 \cdot 109)$
α_1 [−]	$0.5459\ (-2.694 \cdot 10^5, 2.694 \cdot 10^5)$	$0.9088\ (-3.751, 5.569)$
α_2 [−]	$0.6668\ (-46.11, 47.44)$	$0.6014(-0.7552, 1.958)$
Γ [$mol\,m^{-2}$]	$1.306 \cdot 10^{-6}\ (-25.41, 25.41)$	$2.103 \cdot 10^{-6}\ (-1.289, 1.289)$

Table D.2: Results from the numerical fitting of equation D.9 where K_1^0, k_{1+}^0, α, k_{2+}^0 were fitting parameters and Γ was assumed to be equal to $\Gamma = 8.16 \cdot 10^{-6}$ $mol\,m^{-2}$ and the transfer coefficient were assumed equal, $\alpha_1 = \alpha_2 = \alpha$. The data used for the fitting was extracted from polarisation curves from Cherevko *et al.* [50] and Schalenbach *et al.* [2] for alkaline solutions.

Fitting parameters	Cherevko	Schalenbach
K_1^0 [−]	$4.1 \cdot 10^5(-4.407 \cdot 10^8, 4.415 \cdot 10^8)$	$9554(-8.344 \cdot 10^9, 8.344 \cdot 10^9)$
k_{1+}^0 [s^{-1}]	$2066(-1.043 \cdot 10^{10}, 1.043 \cdot 10^{10})$	$6.06(-1.811 \cdot 10^6, 1.811 \cdot 10^6)$
k_{2+}^0 [s^{-1}]	$0.4404(-473.4, 474.3)$	$17.71(-1.547 \cdot 10^7, 1.547 \cdot 10^7)$
α [−]	$0.6989(0.6769, 0.7208)$	$0.7146(0.7004, 0.7287)$

was also abandoned because of the same reasons. Too broad confidence intervals, and also lower bounds, making the insecurities too high. This might come as a surprise since Equation D.9 is very similar to when a quasi-steady-state is assumed, and step D.2 is assumed to be the rds, which is described as an assumption for this study. Comparing to equation D.10,

$$r_2 = \frac{\Gamma k_{2+}^0 \exp\left\{\frac{(1-\alpha)F}{RT}(E - E_n\right\} a_{\mathrm{OH^-}}}{1 + \frac{K_1(E)}{a_{\mathrm{OH^-}}}} = \frac{i_{OER}}{nF} \approx \frac{i}{nF} \tag{D.10}$$

it is easy to see that the only difference is the extra $\frac{k_{2+}^0}{k_{1+}^0}$ term in the denominator in equation D.9. This a consequence of assuming step D.2 to be rds, because that implies that step D.1 is equilibrated and that step D.2 is much slower than step D.1. Subsequently, this means that $k_{1+}^0 \gg k_{2+}^0$, which makes the extra term diminish in comparison to the other terms in the denominator and we are left

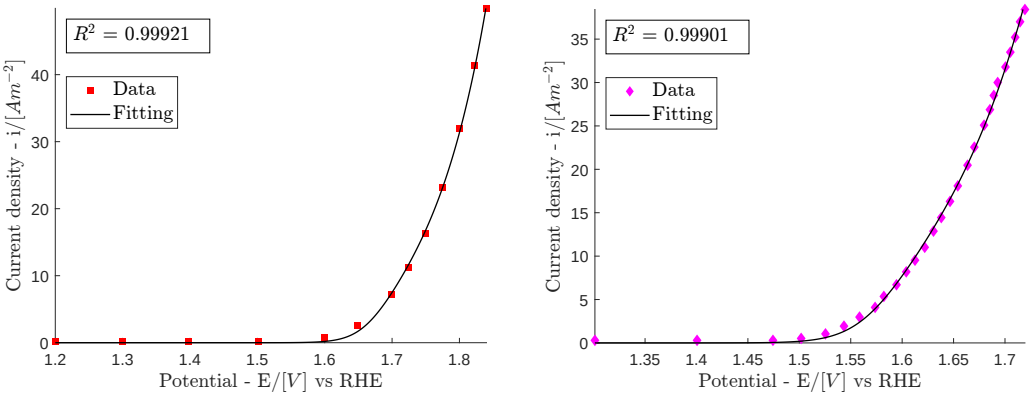

(a) The sampled data from the polarisation curve on IrO_2 in 0.05 mol L^{-1} NaOH from Cherevko *et al.* [50] in red squares and the corresponding curve fitting in black line based on equation D.7. The coefficient of determination is $R^2 = 0.99921$

(b) The sampled data from the polarisation curve on Ir in 0.05 mol L^{-1} NaOH from Schalenbach *et al.* [2] in magenta diamonds and the corresponding curve fitting black line based on equation D.7. The coefficient of determination is $R^2 = 0.99901$

Figure D2: The sampled data from the polarisation curves from Cherevko *et al.* [50] in red squares in figure D2a, Schalenbach *et al.* [2] in magenta diamonds in figure D2b along with their corresponding fits in black line based on the fitting of Equation D.9. The coefficient of determination is also displayed in their respective figures.

with the same result as used in this study. The evaluation of the full analysis approach, was what ultimately led to the assumption of an rds, and the result of the numerical fitting procedure is shown in section 4.[99]

E Ode15s

In order to solve the differential equation that describes the site coverage of IrO_3, which acts as the common intermediate for the chosen mechanism for OER on iridium oxide, given Equation 3.25, we need a stiff equation solver. This is because equation 3.25 is a stiff differential equation, and the "stiff" property is a bit difficult to define. One of the properties of stiff equations is that they make the use of explicit solvers slow in obtaining a solution, and also make the solver unstable [98]. Most notable is this because the step size is being forced to become unreasonably low compared to the integration level, even in regions where the curve is smooth [98]. These small steps will then make an explicit solver use a lot of evaluations in order to traverse a small time step. This makes it necessary to use stiff solvers, which do more work per step, but have a higher numerical stability and they can take larger steps than the explicit solvers can. Dumesic *et al.*[86] also state that by applying microkinetic modelling to such systems as this, with coupled differential equations, the use of stiff solvers is necessary because of the, and they too mentions the use of the built-in solver *ode15s* in MATLAB®.

MathWorks® proposes to use the *ode15s* solver since it performs best in most cases, though *ode23s* is also a good alternative and can at times be even more efficient [100]. *ode15s* is a stiff ordinary differential equation (ODE) solver which utilizes variable step, variable order (VSVO) and is based on the numerical differentiation formulas (NDF) for orders 1 to 5[100]. Since it performs best in most cases, it was chosen as the solver for the numerical approach described in 3.3.

F Code

Some essential parts of the code used for the microkinetic model in the alkaline and acidic models are given here. It consists of three functions that calculate important quatities like k^0_{3+} and $\Gamma\theta_2$. There is no plotting descriptions here, since that is not so relevent for the calculations themselves. For the whole code used in the microkinetic model, see my public github repository[101] and is also availabe from the url:`https://github.com/pekarste/Degradation/tree/main`.

F.1 Acidic model

The following function is called

```
time_theta_potential_ode15s_acidic
```

and takes in input arguments

```
(E_Data, i_data, a_H, T, data_type, k_4_0_plus)
```

and the output from this function is

```
[t_ode_15s_acidic, gamma_theta_ode15s_acidic,
potential_ode15s_1, gamma_theta_interpol]
```

. The input variables to the function are potential, `E_data`, current density, `i_data`, the activity of the proton, `a_H`, temperature, `T`, the data type, `data_type` being a string element either `"array"` or `"number"`, and lastly the chemical forward rate constant of oxygen formation, `k_4_0_plus`. It uses these input parameters and does the numerical fitting procedure to produce the necessary constants, solving Equation 3.33 with a known value of k^0_{4+}, and lastly interpolates the solution obtained by the use of *ode15s* with the measured degradation data from Mayrhofer *et al.*[1]. It returns the time, `t_ode15s_acidic`, and solution, `gamma_theta_ode15s_acidic`, *ode15s* returns on solving Equation 3.33, the potential based related to the time, `potential_ode15s_1`, and lastly the interpolated values of the solution, `gamma_theta_interpol`, to be used for the plotting.

```
function [t_ode15s_acidic, gamma_theta_ode15s_acidic,
    potential_ode15s_1 ,gamma_theta_interpol] =
    time_theta_potential_ode15s_acidic(E_data, i_data, a_H, T,
    data_type,k_4_0_plus)
```

```
%time_theta_potential_ode15s_acidic will take in some a bunch of things
%and giove back arrays of t, theta, and interpolated values
%   Detailed explanation goes here

%% %%%%%%%%%%%%%%%%%%%%% Acidic model %%%%%%%%%%%%%%%%%%%%%%%%%%%%%%%%
% This script will couple all the different functions together and work
% like a masterscript.

%% Define Physical Constants

R = 8.31446261815324;           % J mol^-1 K^-1
F = 96485.3329;                 % A s mol^-1
E_OER_SHE = 1.229;              % Standard reduction potential for OER vs SHE - acidic
E_REF_RHE = 0.0;                % Standard redcution potential for HER vs SHE - acidic
E_n = E_OER_SHE - E_REF_RHE;    % Standard reduction potential for OER vs RHE
a_H2O = 1;                      % [-]
Mm_Ir = 192.2;                  % g/mol [SI]
%gamma = 8.16*10^(-6);          % mol/m^2 [concentration of active sites]
Marhofer_a_H_acidic = 0.05*1;   % [-] - Activity of OH-
theta_2_0 = eps;
%% %%%%%%%%%%%%%%%%%%%%% Fitting %%%%%%%%%%%%%%%%%%%%%%%%%%%%
% Fitting the expression of the current based on r_2 to the data
% The r_2_fit returns the curve (fitting results) and the gof.
% The coefficients are contained in the curve

% Cherevko
[curve_acidic, gof_acidic] = ...
        % This is the expression with rds
    r_2_fit_acidic(E_data, i_data, a_H, T, data_type);
%% %%%%%%%%%%%%%%%%%% Data for degradation
```

```
    %%%%%%%%%%%%%%%%%%%%%%%%%%%%%
Mayrhofer_dissolution_data = readmatrix("Mayrhofer_dissolution_2.
    xlsx");    % Mayrhofer dissolution vs time data - [ng/cm^2s]

%Mayrhofer_dissolution = Mayrhofer_dissolution_data(5:end,2);
             % Mayrhofer dissolution data - [ng/cm^2*s] -- Starting
    from 5 to remove the tail
Mayrhofer_time = Mayrhofer_dissolution_data(5:end,1);
            % Mayrhofer time data [s] -- Starting from 5 to remove
    the tail to be consistent

%Mayrhofer_dissolution_mole = Mayrhofer_dissolution*10^(-9)*10^(4)/
    Mm_Ir;    % Changes the units from ng/cm^2*s --> mole/m^2*s

%% %%%%%%%%%%%%%%%%%%%%Solving differental equation
    %%%%%%%%%%%%%%%%%%%%%%%%

%
    ------------------------------------------------------------------------

[t_ode15s_acidic, gamma_theta_ode15s_acidic] =
    diff_equation_solver_acidic(Mayrhofer_time, "value",
    curve_acidic, Marhofer_a_H_acidic, T, k_4_0_plus, theta_2_0);

%% %%%%%%%%%%Transforming time to potential for the ode15s solution
potential_ode15s_1 = CV_potential_acidic(t_ode15s_acidic, "array");

%% Interpolating the solution from ode15s to find values
    corresponding to
% the measured values since ode15s gives more points
gamma_theta_interpol = interp1(t_ode15s_acidic,
    gamma_theta_ode15s_acidic,Mayrhofer_time);

end
```

The next function is called

```
chi_square_acidic
```

and takes in

```
(time_solver, gamma_theta_solver, k_4_0_plus,
time_data, degradation_data)
```

and returns

```
[curve]
```

Just as the name of the function implies, this function is minimising χ^2 from Equation 3.39 with respect to k^0_{3+}. The input parameters represent the time, t, and solution, $\Gamma\theta_2$, from the solution of Equation 3.33 by the use of *ode15s* as `time_solver` and `gamma_theta_solver`. In addition, it takes in the k^0_{4+}, `k_4_0_plus`, and the sampled time and degradation data from Mayrhofer *et al.*[1], `time_data` and `degradation_data`. It is a numerical fitting procedure that returns a `cfit` structure which contains the minimised value of k^0_{3+} in `curve` as `k_3_0_plus`.

```
function [curve] = chi_square_acidic(time_solver, gamma_theta_solver
    , k_4_0_plus, time_data, degradation_data)
%UNTITLED Summary of this function goes here
%   Detailed explanation goes here

%gamma = 8.16*10^(-6);
             % [mol/m^^2]
a_H2O = 1;

fun = @(k_3_0_plus, x) k_3_0_plus.*a_H2O.*interp1(time_solver,
    gamma_theta_solver, x);
FT = fittype(fun, 'independent',{'x'}, 'coefficients',{'k_3_0_plus'
    });

FO = fitoptions('Method','NonLinearLeastSquares',...
            'Lower', eps,...
            % k_3_0_plus
            'Upper', 10^4, ...
            'StartPoint', k_4_0_plus,...
            'TolFun', 1e-20);
            % k_3_0_plus

[curve, gof, output,warnstr,errstr,convmsg]...
    = fit(time_data,degradation_data,FT,FO);

end
```

F.2 Alkaline model

The following functions are the same as the ones introduced in the acidic model, just an alkaline version.

The first function is the alkaline version of `time_theta_potential_ode15s_acidic`, and is

```
time_theta_potential_ode15s_alkaline
```

which takes in

```
(E_data, i_data, a_OH, T, data_type, k_4_0_plus)
```

and returns

```
[t_ode_15s_alkaline, gamma_theta_ode15s_alkaline,
potential_ode15s_1, gamma_theta_interpol]
```

The input parameters are all the same as the ones introduced in the first acidic model, except that the activity of the proton, `a_H`, has naturally been replaced by the activity of the hydroxide, `a_OH`. This also means that the return values are the same as in the acidic model, only alkaline. This is also why many of the output names have `_alkaline` at the end.

```
function [t_ode15s_alkaline, gamma_theta_ode15s_alkaline,
    potential_ode15s_1 ,gamma_theta_interpol] =
    time_theta_potential_ode15s_alkaline(E_data, i_data, a_OH, T,
    data_type,k_4_0_plus)
%time_theta_potential_ode15s_alkaline will take in some a bunch of
    things
%and giove back arrays of t, theta, and interpolated values
%   Detailed explanation goes here

%% %%%%%%%%%%%%%%%%%%%% ALKALINE model
    %%%%%%%%%%%%%%%%%%%%%%%%%%%%%%%%
% This script will couple all the different functions together and
    work
% like a masterscript.


% Will try to use acidic equations but alkaline environemnt
%% Define Physical Constants
```

```
13
14 R = 8.31446261815324;
                % J mol^-1 K^-1
15 F = 96485.3329;
                % A s mol^-1
16 E_OER_SHE = 0.40;
                % Standard reduction potential for OER vs SHE - alkaline
17 E_REF_SHE = -0.829;
                % Standard redcution potential for HER vs SHE - alkaline
18 E_n = E_OER_SHE - E_REF_SHE;
                % Standard reduction potential for OER vs RHE - alkaline
19 a_H2O = 1;
                % [-]
20 Mm_Ir = 192.2;
                % g/mol [SI]
21 gamma = 8.16*10^(-6);
                % mol/m^2 [concentration of active sites]
22 theta_2_0 = eps;
23 Schalenbach_OH_alkaline = 0.05*1;
                   % [-] - Activity of OH-
24
25 %% %%%%%%%%%%%%%%%%%%%%% Fitting %%%%%%%%%%%%%%%%%%%%%%%%%%%
26 % Fitting the expression of the current based on r_2 to the data
27 % The r_2_fit returns the curve (fitting results) and the gof.
28 % The coefficients are contained in the curve
29
30 % Cherevko
31 [curve_alkaline, gof_alkaline] = ...
                % This is the expression with rds
32     r_2_fit_alkaline(E_data, i_data, a_OH, T, data_type);
33 %% %%%%%%%%%%%%%%%%% Data for degradation
    %%%%%%%%%%%%%%%%%%%%%%%%%%%%%%%
34 Schalenbach_dissolution_CV_linear_data = readmatrix("Data\Alkaline\
    Schalenbach\Schalenbach_dissolution_alkaline_peak_1.xlsx");
35 % Schalenbach dissolution vs time - [ng/cm^2*s]
36
37 %Schalenbach_dissolution_CV_linear =
    Schalenbach_dissolution_CV_linear_data(1:end,2);    %
    Schalenbach dissolution data - [ng/cm^2*s]
38 Schalenbach_time_CV_linear = Schalenbach_dissolution_CV_linear_data
    (1:end,1);           % Schalenbach time data - [s]
39
```

```
%Schalenbach_dissolution_mole = Schalenbach_dissolution_CV_linear
    *10^(-9)*10^(4)/Mm_Ir;  % Changes the units from ng/cm^2*s -->
    mole/m^2*s

%% %%%%%%%%%%%%%%%%%%%%Solving differental equation
    %%%%%%%%%%%%%%%%%%%%%%%%

%
    ------------------------------------------------------------------------

[t_ode15s_alkaline, gamma_theta_ode15s_alkaline] =
    diff_equation_solver_alkaline(Schalenbach_time_CV_linear, "value
    ", curve_alkaline, Schalenbach_OH_alkaline, T, k_4_0_plus,
    theta_2_0);

%% %%%%%%%%%%Transforming time to potential for the ode15s solution
potential_ode15s_1 = CV_potential_alkaline(t_ode15s_alkaline, "array
    ");

%% Interpolating the solution from ode15s to find values
    corresponding to
% the measured values since ode15s gives more points
gamma_theta_interpol = interp1(t_ode15s_alkaline,
    gamma_theta_ode15s_alkaline,Schalenbach_time_CV_linear);

end
```

This function is too the alkaline version of minimising χ^2 by Equation 3.39. The function is called

```
chi_square_alkaline
```

also recognized by the `_alkaline` at the end of the name. It takes in the same arguments as the acidic `chi_square_acidic`

```
(time_solver, gamma_theta_solver, a_OH, k_4_0_plus,
time_data, degradation_data
```

except that the activity of the hydroxide has replaced the activity of the proton by `a_OH`. Lastly, it returns

```
[curve]
```

which is a `cfit`, which contains the minimised value of k_{3+}^0, `k_3_0_plus`, inside `curve`.

```
function [curve] = chi_square_alkaline(time_solver,
    gamma_theta_solver, a_OH, k_4_0_plus, time_data,
    degradation_data)
%UNTITLED Summary of this function goes here
%   Detailed explanation goes here

%gamma = 8.16*10^(-6);
             % [mol/m^^2]

fun = @(k_3_0_plus, x) k_3_0_plus.*a_OH.^(2).*interp1(time_solver,
    gamma_theta_solver, x);
FT = fittype(fun, 'independent',{'x'}, 'coefficients',{'k_3_0_plus'
    });

FO = fitoptions('Method','NonLinearLeastSquares',...
            'Lower', eps,...
            % k_3_0_plus
            'Upper', 10^4, ...
            'StartPoint', k_4_0_plus,...
            'TolFun', 1e-20);
            % k_3_0_plus

[curve, gof, output,warnstr,errstr,convmsg]...
    = fit(time_data,degradation_data,FT,FO);

end
```

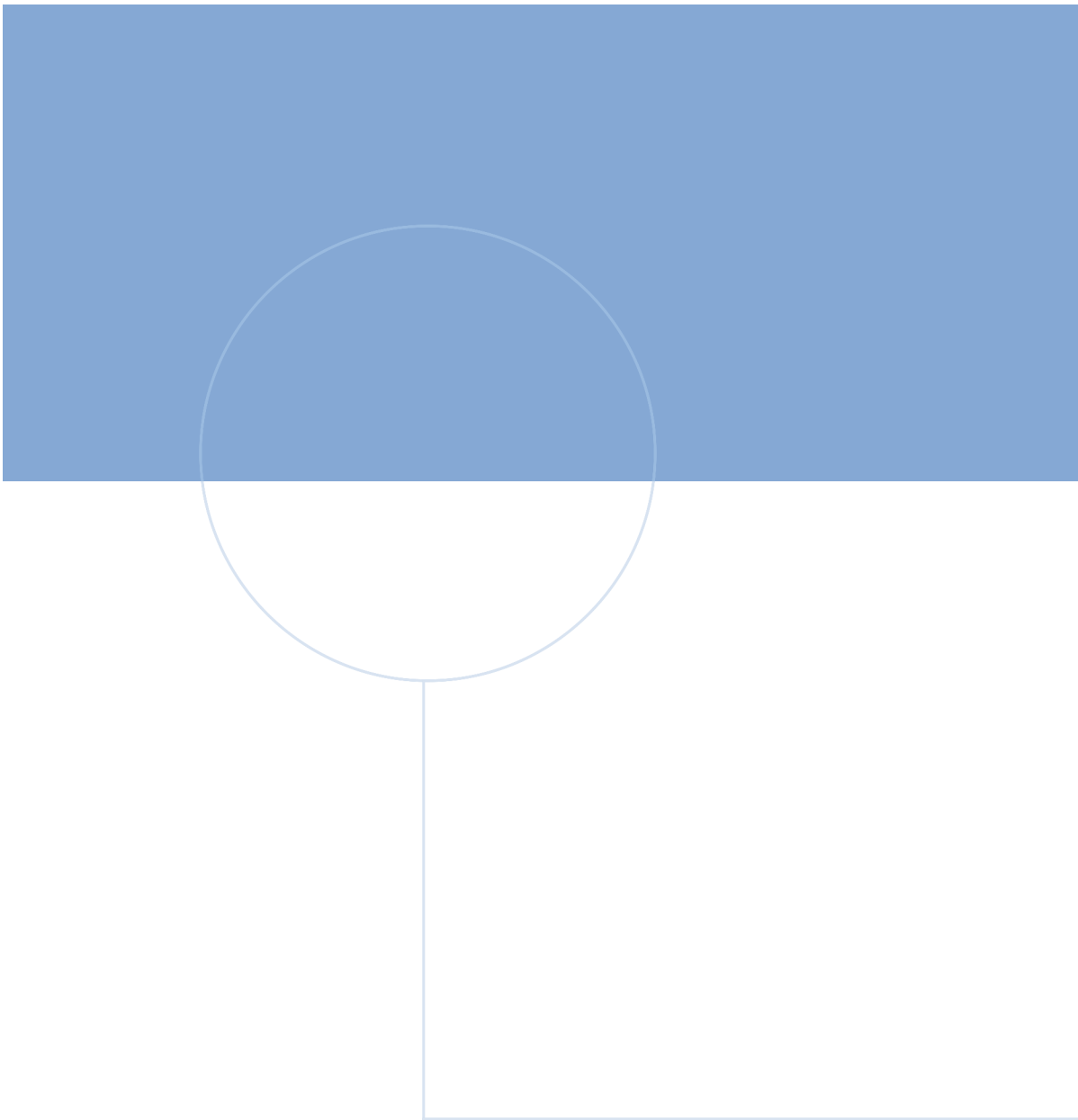

NTNU

Norwegian University of
Science and Technology